

# Punching shear of slabs on top of ribbed foundation piles

September 2013

J.F.N. Schut

Master of Science Thesis



DELFT UNIVERSITY OF TECHNOLOGY

MASTER THESIS

# Punching shear behaviour of structural slabs on top of ribbed foundation piles

Assessment by nonlinear finite element analyses

*A thesis submitted to Delft University of Technology  
for the degree of Master of Science in Civil Engineering*

***Author:***

J.F.N. Schut

***Thesis committee:***

prof.dr.ir. D.A. Hordijk  
dr.ir. C.B.M. Blom  
dr.ir. P.C.J. Hoogenboom  
ir. L.J.M. Houben

Delft University of Technology  
Faculty of Civil Engineering and Geosciences  
Department of Structural Engineering  
Section of Concrete Structures

September 29, 2013

*A good scientist is a person with original ideas. A good engineer is a person who makes a design that works with as few original ideas as possible.*

Dyson, Freeman

# Acknowledgements

I would like to extend a very big thank you to my graduation committee for their support, input and feedback during the realisation of the thesis. Their knowledge and questions about the subject often led me to new insights and solutions for problems I encountered. Similarly, I would like to acknowledge Rene Braam for the guidance during my numerical simulations. My special thanks goes to Kees Blom, who fulfilled the role of daily supervisor. He gave me support and feedback on my progress, practically every week. Thanks also for reminding me to enjoy the last part of my life as a student.

I would like to thank my parents and elder sisters for their ongoing encouragement and support. Sometimes it is the small things that mean the most when you are so far into this process, you can't see out.

Thanks to my amazing friends for their ongoing support through this process and for being able to figure out whether it was safe to ask, "How is the thesis going?" A special mention to Daniël Schönfeld, you have been a good fellow student and have become a true friend, thanks for the support during the last four years.

At the end, thanks to you, reader. If you are reading this line after the others, you at least read one page of my thesis. Thank you.

Jesse Schut  
Delft, September 2013



# Abstract

The excavated building pit is a frequently used building technique during the construction of structures below ground level. A temporary structure of sheet piles and underwater concrete is designed to retain soil and water. Ribbed tension piles are driven before concreting the water retaining slab. These tension piles compensate the hydrostatic pressure after de-watering of the construction pit. The water retaining slab is often not used as a structural member during exploitation due to the relative inaccurate process of concreting below groundwater table and the associated risks. A structural concrete slab is poured in top of the water retaining slab. Generally, the top of the foundation piles are crushed before concreting the structural slab. The uncovered pile reinforcement is combined with the slab reinforcement which results in a monolithic floor with an optimal connection between slab and pile. During some construction projects it is desirable to avoid pile head crushing for economic reasons or to prevent the stray current phenomena. Stray current is a flow of electricity through the ground due to imbalances in electrical rail systems. The presence of stray current can cause accelerated metal corrosion, because the electrical flow causes the metal to break down into its ions and enter the ground. The concrete cover around the pile reinforcement avoids this phenomena.

The question that arises is to what extent does the partly penetrated foundation pile influence the punching shear behaviour of the structural slab when the pile is loaded in compression during the exploitation phase. Punching shear is a phenomenon in concrete slabs caused by concentrated support reactions, inducing a cone shaped perforation starting from the surface of the slab. Punching shear is a brittle and undesirable failure mode because of the absence of structural warning before failure. The Dutch CUR 77 design code approach with respect to punching shear verification for underwater concrete slabs assumes tensile forces during the construction stage. This is the stage corresponding to an empty building pit when the foundation piles compensate the hydrostatic pressure. This design code doesn't include an approach in case the piles are loaded in compression after the complete construction is built. The same holds for the Eurocode 2 design approach for structural slabs, which assumes that the support reaction applies at the surface of the slab. This is not the case when the foundation pile partly penetrates the structural slab. The lack of a clear design approach causes a structural debate about this complex problem.

At the heart of this debate lies the problem of the effectiveness of the present ribs and the associated punching cone perimeter. In other words, what becomes the effective depth of the slab in case of a partly penetrated ribbed foundation pile. Is it the total depth from slab surface to slab bottom or only the depth between the slab surface and pile head? The size of the punching cone perimeter is highly important because it determines the slab resistance against this failure mode.

In order to investigate the punching shear behaviour, simulations by nonlinear finite element analyses have been performed using the software ATENA developed by Červenka Consulting. Initially, conducted experiments were simulated in order to validate the modelling technique. This chapter focuses on the numerical simulation of the contact area between the slab and the ribbed pile. The contact area is modelled with interface material, based on the Mohr-Coulomb failure criterion for shear planes. The FEM analyses showed good agreement with the conducted experiments regarding to crack propagation which induces punching shear.

A fictitious case study of a unreinforced concrete slab element with a partly penetrated ribbed pile was analysed in the present work. The case study is made up of a number of subsequent modelling steps to investigate each influence separately. The case study starts with a parameter study to investigate the influence of the shear transfer capacity from slab to pile on the punching behaviour. The maximum allowable shear stress depends of a cohesion parameter and a coefficient of friction parameter. Various combinations of both parameters are investigated with respect to the punching shear behaviour. A clear distinction in failure behaviour is observed between a friction coefficient of 1.0 and 1.4. Up to a friction coefficient of 1.0, the critical shear crack propagates from pile head towards the slab surface which indicates that only the top part of the slab is responsible for punching shear resistance. From a friction coefficient of 1.4 the critical shear crack propagates from slab bottom towards slab surface, which indicates that the full slab height is active in punching resistance. This change in punching cone size results in a failure load which is more than twice as high. No significant increase of failure load is observed during analyses with different cohesion values.

The second step consists of adding reinforcement to the initial model. The influence of both bending and shear reinforcement is analysed with respect to the punching shear resistance. The influence of bending reinforcement was neglectable due to the limited slab deflections. The limited deflections are the result of the low slab slenderness which implies high bending stiffness. However, the influence of shear reinforcement was significant. For friction coefficients from 0.0 to 1.0, the failure load increased with a magnitude of roughly four compared to the failure load without shear reinforcement. An increase of roughly two is observed for friction coefficients of 1.4 or greater. Also a change in failure behaviour is observed during the analyses with shear reinforcement. For friction coefficients of 1.0 or greater, the brittle punching behaviour changes into ductile flexural behaviour. This is highly desirable because large structural deflections insinuates an upcoming failure.

The last step consists of adding non symmetry to the initial model. A non symmetric load condition is introduced by removing one of the two supporting plates. The results show a slight increase of the slab capacity of about 4%. The slight increase is the result of increased compression stresses at the bottom side of the foundation pile. This has a positive influence on the shear stress resistance of the contact area with respect to the Mohr-Coulomb friction law.

Although full scale laboratory tests are needed to verify the numerical results, the recommendation for practical use is that for structural slabs provided with shear reinforcement and a foundation pile with at least two ribbed sides, a fully punching cone develops.



# Contents

<b>Acknowledgements</b>	<b>i</b>
<b>Abstract</b>	<b>iii</b>
<b>List of Figures</b>	<b>xi</b>
<b>List of Tables</b>	<b>xiii</b>
<b>List of Symbols</b>	<b>xv</b>
<b>1 Introduction</b>	<b>1</b>
1.1 Background . . . . .	1
1.2 Punching shear phenomenon . . . . .	3
1.3 Objective . . . . .	6
1.4 Thesis outline . . . . .	6
<b>2 Literature review</b>	<b>7</b>
2.1 Experimental studies . . . . .	7
2.1.1 Experiment of Elstner and Hognestad . . . . .	7
2.1.2 Experiment of Bollinger . . . . .	8
2.1.3 Experiment of Kinnunen and Nylander . . . . .	9
2.1.4 Experiment of Ka Lun Li . . . . .	10
2.1.5 Experiment of Braam, Bosman and Van Rhijn . . . . .	11
2.1.6 Discussion . . . . .	13
2.2 Analytical studies . . . . .	14
2.2.1 The model of Talbot . . . . .	14
2.2.2 The model of Kinnunen and Nylander . . . . .	15
2.2.3 The model of Nielsen . . . . .	16
2.2.4 The model of Muttoni . . . . .	17
2.2.5 Discussion . . . . .	20
2.3 Punching shear verification . . . . .	20
2.3.1 ACI 318-08 . . . . .	21
2.3.2 EC 2 . . . . .	21
2.3.3 BS 8110 . . . . .	22
2.3.4 CUR 77 . . . . .	22
2.3.5 Discussion . . . . .	22
2.4 Interface between concrete cast at different times . . . . .	24
2.4.1 EC 2 . . . . .	25
2.4.2 FIP . . . . .	26

2.4.3	Daschner . . . . .	26
2.4.4	Nissen . . . . .	27
<b>3</b>	<b>Finite element modelling</b>	<b>29</b>
3.1	Non-linearity . . . . .	29
3.2	Numerical solution methods . . . . .	30
3.2.1	The Newton-Raphson iteration . . . . .	30
3.2.2	Arc length iteration . . . . .	32
3.2.3	The line search method . . . . .	33
<b>4</b>	<b>Modelling of reinforced concrete in ATENA</b>	<b>35</b>
4.1	Material modelling . . . . .	35
4.1.1	Concrete model . . . . .	36
4.1.2	Reinforcement model . . . . .	41
4.2	Structural definition . . . . .	41
4.2.1	GAP-elements . . . . .	42
4.3	Solution control setting . . . . .	43
<b>5</b>	<b>Validation of modelling technique</b>	<b>45</b>
5.1	Laboratory tests for comparison . . . . .	46
5.1.1	Geometrical data and loading . . . . .	46
5.1.2	Material data . . . . .	47
5.1.3	Results and observations from experiments . . . . .	48
5.2	Finite element modelling of laboratory tests . . . . .	49
5.2.1	Boundary conditions and loading . . . . .	49
5.2.2	Material properties . . . . .	50
5.2.3	Interface material . . . . .	51
5.2.4	Finite elements . . . . .	52
5.3	Results from numerical analyses . . . . .	53
5.3.1	Crack pattern development . . . . .	55
5.3.2	Fracture strain development . . . . .	57
5.3.3	Load-displacement behaviour . . . . .	58
5.4	Discussion . . . . .	60
<b>6</b>	<b>Finite element modelling of thesis objective</b>	<b>61</b>
6.1	General modelling considerations . . . . .	62
6.1.1	Geometrical specifications . . . . .	62
6.1.2	Boundary conditions and loading . . . . .	63
6.1.3	Material properties . . . . .	64
6.1.4	Finite elements . . . . .	64
6.1.5	Modelling scheme . . . . .	65
6.2	Boundary limits . . . . .	65
6.2.1	No interface connection . . . . .	66
6.2.2	Perfect interface connection . . . . .	68
6.3	Parameter study . . . . .	70
6.3.1	Failure mechanism 1 . . . . .	73
6.3.2	Transition zone . . . . .	73
6.3.3	Failure mechanism 2 . . . . .	75
6.3.4	Numerical analyses vs. experimental studies . . . . .	76
6.4	Influence of reinforcement . . . . .	76
6.4.1	Bending reinforcement . . . . .	76

6.4.2	Shear reinforcement . . . . .	78
6.5	Influence of a smooth pile surface . . . . .	83
6.6	Non symmetric load conditions . . . . .	85
<b>7</b>	<b>Conclusion and recommendations</b>	<b>89</b>
7.1	Introduction . . . . .	89
7.2	Conclusions . . . . .	89
7.3	Recommendations . . . . .	90
	<b>Bibliography</b>	<b>92</b>
	<b>Appendices</b>	<b>I</b>
<b>A</b>	<b>ATENA Input - Validation Chapter</b>	<b>III</b>
<b>B</b>	<b>ATENA Input - Case Study</b>	<b>XIX</b>
<b>C</b>	<b>Encountered modelling problems</b>	<b>XLV</b>



# List of Figures

1.1	Crushing heads of prefabricated piles . . . . .	2
1.2	Piper’s Row Car Park, Wolverhampton, UK, 1997 [55] . . . . .	3
1.3	Schematic presentation of different crack patterns for a column loaded in compression [50] . . . . .	3
1.4	Punching shear crack development, viewed from tensile face [25] . . . . .	4
1.5	Photos of a punching shear cone observed during experiments conducted by M. Hallgren et al. [36] . . . . .	5
1.6	Representation of punching shear cones, loaded in compression . . . . .	5
2.1	Setup of punching experiment Elstner and Hognestad [46] . . . . .	7
2.2	Results experiment of Elstner and Hognestad [46] . . . . .	8
2.3	Results experiment of Bollinger [7] . . . . .	9
2.4	Results experiment of Kinnunen and Nylander [48] . . . . .	10
2.5	Results experiment of Ka Lun Li [35] . . . . .	11
2.6	Punching shear cone element after failure [16] . . . . .	11
2.7	The analytical model of Talbot [5] . . . . .	14
2.8	The analytical model of Kinnunen and Nylander [48] . . . . .	15
2.9	The analytical model of Nielsen [42] . . . . .	16
2.10	The analytical model Muttoni [40] . . . . .	18
2.11	Design procedure to check punching shear strength . . . . .	19
2.12	Comparison between design codes according to Sagaseta [33] . . . . .	23
2.13	Comparison between design codes according to Muttoni [41] . . . . .	23
2.14	The Mohr-Coulomb shear failure criterion . . . . .	24
2.15	Indented construction joint [10] . . . . .	25
3.1	Regular Newton-Raphson iteration . . . . .	31
3.2	Modified Newton-Raphson iteration . . . . .	32
3.3	Phenomena in which arc-length control is recommendable . . . . .	32
3.4	Arc-length control . . . . .	33
4.1	Uniaxial stress-strain law for concrete . . . . .	36
4.2	Fixed and rotated crack model . . . . .	37
4.3	Stress-crack opening law according to Hordijk [27] . . . . .	38
4.4	Reduction of compressive strength due to the development of lateral tensile strains . . . . .	39
4.5	Compressive hardening/softening based on experimental observations by van Mier [38] . . . . .	40
4.6	Transmitting shear stresses across the crack by aggregate interlock . . . . .	41
4.7	The bilinear stress-strain law for reinforcement . . . . .	41
4.8	Failure surface for interface elements . . . . .	43

5.1	Experimental setup pull-out tests Braam et al. [16]	46
5.2	The different rib geometries of all series	47
5.3	Presentation of pull-out cone for directions $R_1$ and $R_2$	48
5.4	Boundary conditions and prestressing layout	50
5.5	Linear and quadratic tetrahedral element	52
5.6	Mesh configuration of modelled specimen and monitoring points	53
5.7	Top view of specimen surface during the experiment	55
5.8	Crack pattern development before failure of specimen 3-1 Interface 1 (crack filter 0.1 mm)	56
5.9	Development of principle fracture strain [-] of specimen 1-1 with interface 1	57
5.10	Force-displacement graph of specimen 1-1 corresponding to monitoring point 8	58
5.11	Force-displacement graph of specimen 3-1 corresponding to monitoring point 4	59
6.1	Considered field element from a fictitious infinite flat slab	61
6.2	Geometrical specifications of the investigated field element	62
6.3	Boundary conditions and loading	63
6.4	Mesh configuration of modelled specimen and monitoring points	65
6.5	Load-displacement graph of monitoring point 2 corresponding to sliding connection	66
6.6	Vertical slab displacement (z-axis) of field element after failure [m] (scale factor = 50)	67
6.7	Crack width (no crack filter) of field element corresponding to no interface connection [m]	67
6.8	Load-displacement graph of monitoring point 2 corresponding to perfect interface connection	68
6.9	Vertical slab displacement (z-axis) of field element after failure [m] (scale factor = 50)	69
6.10	Crack width (no crack filter) of field element corresponding to perfect interface connection [m]	70
6.11	Surface chart with failure loads corresponding to various combinations of friction coefficients and cohesion	71
6.12	Failure load - Friction coefficient graph (Cohesion = 1.0 N/mm <sup>2</sup> )	72
6.13	Development of principal fracture strain [-] ( $c = 1.0$ N/mm <sup>2</sup> , $\mu = 1.0$ )	73
6.14	Load-displacement graph of monitoring point 2 corresponding different friction coefficients (Cohesion = 1.0 N/mm <sup>2</sup> )	74
6.15	Principal fracture strain at failure [-] ( $c = 1.0$ N/mm <sup>2</sup> , $\mu = 1.2$ )	74
6.16	Development of principal fracture strain [-] ( $c = 1.0$ N/mm <sup>2</sup> , $\mu = 1.4$ )	75
6.17	Reinforced vs. unreinforced load-displacement graph ( $c = 1.0$ and $\mu = 1.5$ )	77
6.18	Principal stress of bending reinforcement at failure [N/mm <sup>2</sup> ]	77
6.19	Top view of specimen with cracked elements after failure (no crack filter)	78
6.20	Shear reinforcement layout located around the foundation pile	79
6.21	Failure load - Friction coefficient graphs ( $c = 0.5$ N/mm <sup>2</sup> )	80
6.22	Load - Displacement graph for different friction coefficients	80
6.23	Principal fracture strain at failure [-] ( $c = 0.5$ N/mm <sup>2</sup> , $\mu = 0.5$ )	81
6.24	Principal stress and strain at failure ( $c = 0.5$ N/mm <sup>2</sup> , $\mu = 0.5$ )	82
6.25	Principal fracture strain at failure [-] ( $c = 0.5$ N/mm <sup>2</sup> , $\mu = 1.6$ )	82
6.26	Principal stress and strain at failure ( $c = 0.5$ N/mm <sup>2</sup> , $\mu = 1.6$ )	83
6.27	Load - Displacement graph for different pile conditions	84
6.28	Principle fracture strain at failure for different pile conditions [-]	85
6.29	Considered field element with non symmetric load condition	86

6.30	Results experiment of Sagaseta et al. [33]	86
6.31	Development of principal fracture strain with non symmetric load condition	
	[-] ( $c = 0.7 \text{ N/mm}^2$ , $\mu = 1.4$ )	87
6.32	Normal interface stress [ $\text{N/mm}^2$ ] ( $c = 0.7 \text{ N/mm}^2$ , $\mu = 0.2$ )	88





# List of Tables

2.1	Diameters and the average internal crack slopes . . . . .	12
2.2	Failure load comparison based on experimental data and the theory . . . . .	12
2.3	Cohesion and friction coefficient according to EC 2 section 6.2.5 [10] . . . . .	25
2.4	Cohesion and friction coefficient according to FIP [43] . . . . .	26
2.5	Cohesion and friction coefficient according to Daschner [20] . . . . .	26
2.6	Cohesion and friction coefficient according to Nissen et al. [29] . . . . .	27
4.1	Default values of error tolerances . . . . .	43
5.1	Concrete maturity data and centric tensile strengths . . . . .	48
5.2	Dywidag prestressing cable properties . . . . .	48
5.3	Experimental results conducted by Braam et al [16] . . . . .	49
5.4	Concrete slab material parameters . . . . .	51
5.5	Concrete pile material parameters . . . . .	51
5.6	Dywidag prestressing cable properties . . . . .	51
5.7	Implemented friction coefficients . . . . .	52
5.8	Finite element mesh generation . . . . .	52
5.9	Experimental results versus numerical results . . . . .	53
6.1	Basic material properties for concrete slab . . . . .	64
6.2	Finite element mesh generation . . . . .	65
6.3	Failure loads corresponding to various combinations of friction coefficients and cohesion [kN] . . . . .	71
6.4	Comparison of failure load for slab with and without shear reinforcement . . . . .	79
6.5	Surface conditions with associated cohesion and friction coefficient values . . . . .	84



# List of Symbols

## Roman upper case letters

$A$	cross sectional area
$E$	modulus of elasticity
$EI$	bending stiffness
$F$	force
$G$	modulus of rigidity
$G_f$	fracture energy
$\underline{K}$	stiffness matrix
$H$	hardening modulus for steel model
$L$	length
$M$	bending moment
$P$	load
$S_F$	crack shear stiffness factor
$V$	shear force

## Roman lower case letters

$a_r$	distance between pile ribs
$b_0$	perimeter of critical section
$c$	cohesion
$c'$	catenary shell diameter
$c''$	conical shell diameter
$d$	effective depth concrete section
$d_{g0}$	reference aggregate size
$d_g$	maximum aggregate size
$\underline{f}$	force vector
$f$	material strength
$h$	slab height
$k_i$	material constants, $i = 1, 2, 3...$
$l$	slab length

$n$	number of ribbed pile sides
$m$	bending moment per unit width
$\underline{p}$	displacement vector
$r$	radius
$r_{c,lim}$	reduction limit as lateral tensile strains develops
$s_{max}$	maximum crack spacing
$u$	control perimeter punching cone
$v$	shear strength
$w_d$	critical compressive displacement
$w$	crack opening, vertical displacement of slab

### Greek lower case letters

$\alpha$	inclination of conical shell
$\beta$	coefficient for plastic flow direction
$\gamma$	partial safety factor
$\Delta$	increment
$\delta$	slab deflection
$\varepsilon$	strain
$\eta$	size factor
$\kappa$	correction factor for dowel action
$\lambda$	load multiplier
$\mu$	coefficient of friction
$\nu$	Poisson's ratio
$\rho$	density
$\rho_l$	reinforcement ratio
$\sigma$	stress
$\tau$	shear stress
$\phi$	reinforcement bar diameter
$\psi$	slab rotation

### Superscripts

$-e$	elastic component
$-p$	plastic component
$-f$	fracture component
$-n$	iteration

## Subscripts

$^{-}0$	initial value
$^{-}1,2,3$	principal values
$^{-}c, ^{-}s$	concrete, steel contribution
$^{-}ext, ^{-}int$	external, internal contribution
$^{-}R, ^{-}E$	response, action contribution
$^{-}ck, ^{-}m, ^{-}d$	characteristic, mean and design value
$^{-}cr$	cracking value
$^{-}i,j,k,l$	tensorial indices
$^{-}n$	nominal value
$^{-}u$	ultimate value
$^{-}x,y,z$	Cartesian coordinates
$^{-}y$	yield value



# Chapter 1

## Introduction

### 1.1 Background

The excavated building pit is a frequently used building technique during the construction of structures below ground level. A temporary structure of sheet piles and underwater concrete is designed to retain water and soil. The construction pit is ready for excavation after all sheet piles are driven to the required depth. In case of deep excavations, temporary struts or anchor tie rods are applied to reduce the horizontal deformation of the sheet pile wall. In areas with a high groundwater table, the construction pit will be flooded by groundwater during the excavation. In order to work in a dry environment and to prevent continuously pumping of water, the bottom of the pit is provided with a concrete layer to resist the hydrostatic pressure. This water retaining slab is poured with the presence of a flooded building pit and is for that reason often called *underwater concrete*. In case of an empty excavation pit, the dead weight of the concrete slab is often not enough to be in vertical equilibrium with the hydrostatic pressure resulting from the groundwater. Hence tension piles are driven before concreting the slab. The downward orientated pile force and the dead load of the concrete layer compensates the hydrostatic pressure.

Tension piles are characterised by an internal or external ribbed top section. These ribs have the function to withstand tensile stresses and to stimulate the load transfer from the concrete slab to the pile. The number of ribbed sides depends on the manufacturer and wishes of the client. From practical point of view commonly three sides are ribbed. Usually, the manufacturer fabricates foundation piles in horizontally orientated steel moulds. After concreting the pile, it is more convenient to smooth the top surface.

After concreting the water retaining slab, the construction pit is ready for de-watering. The hydrostatic pressure acting on the bottom of the concrete layer is equal to the height of the reduced water column. During de-watering, tension piles compensate the weight of the pumped groundwater. The piles transfer the tensile forces by friction to the surrounded soil. Due to the relative inaccurate concreting process below water table and the associated risks like water-bearing cracks, the unreinforced slab is usually not used as a structural member in the exploitation phase. In this case it is necessary to concrete a structural slab with reinforcement on top of the underwater concrete. Generally before concreting, the top of the ribbed pile is crushed. The uncovered pile reinforcement is bent and included into the slab reinforcement. The result is a monolithic floor with an optimal connection between the slab and foundation pile.

Figure 1.1(a) shows an example of uncovered reinforcements after pile head crushing. Figure 1.1(b) shows a close-up of pile reinforcement combined with slab reinforcement. In this case the pile and slab are fully connected to ensure structural integrity.



(a) Uncovered pile reinforcement [49]

(b) Pile reinforcement combined with slab reinforcement [54]

**Figure 1.1: Crushing heads of prefabricated piles**

During certain construction projects it is desirable from economical, environment and/or social point of view to avoid pile crushing. The benefits for using not crushed piles are:

1. Economically:

- shorter piles necessary (saving in material costs);
- reduction in transportation costs;
- time saving due to the absence of pile cutting;
- cost saving due to the absence waste material;
- prevention of stray current phenomena.

2. Environmentally:

- reduction of needed raw materials;
- no disturbance due to vibrations;
- no disturbance due to noise;
- no disturbance due to dust;
- no waste material.

3. Socially:

- no labour at difficult accessible locations;
- no labour intensive work (vibrations, noise, dust).

Stray current is a flow of electricity through the ground due to imbalances in electrical rail systems. The presence of stray current can cause accelerated metal corrosion, because the electrical flow causes the metal to break down into its ions and enter the ground. The concrete cover around the pile reinforcement avoids this phenomena.

The question that arises is to what extend does not crushing the pile head influence the overall structural integrity. This thesis focuses on one special failure mechanism which is called *punching shear failure*. Special attention is paid to the role of the ribs in this failure mechanism.



## 1.2 Punching shear phenomenon

A critical point in slabs is the bearing capacity around concentrated forces like foundation piles and columns. The combination of relative high shear forces and bending moments may cause failure. Although this is a highly localised mechanism, it could cause failure of the total structure due to the increase of shear forces in other structural members. Figure 1.2 shows an example of a partial collapsed car park due to punching shear failure.

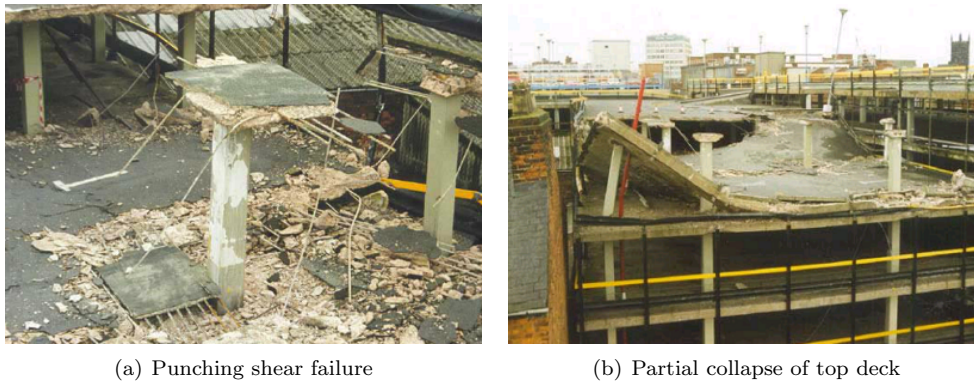


**Figure 1.2: Piper’s Row Car Park, Wolverhampton, UK, 1997 [55]**

Punching shear failure is characterised by a truncated-cone-shaped element that appears after failure. The shape of this element is the result of the interaction between shear stresses and bending stresses around a concentrated load. Punching shear failure is a local mechanism and is associated to a brittle failure. Brittle failure implies a failure mechanism without any structural warning in the form of large displacement or visible crack formation. This makes punching shear a dangerous phenomenon. Punching shear failure occurs only in elements carrying bending moments and shear forces in two directions. For this reason, punching shear is called *two-way shear*.

Two different crack propagations can be distinguished during the crack development until punching failure. Figure 1.3(a) presents the crack pattern caused by pure shear stresses, and Figure 1.3(b) presents the crack pattern corresponding to flexural stresses.

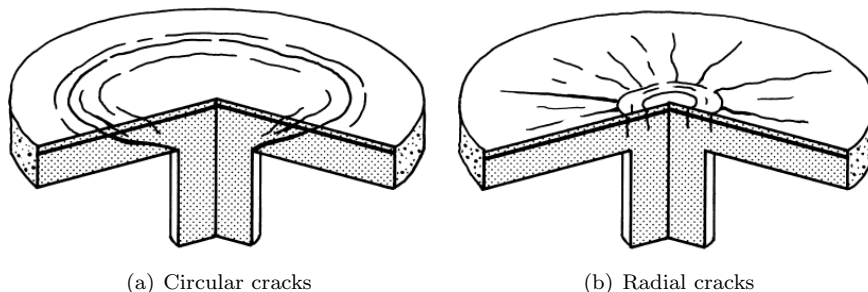


**Figure 1.3: Schematic presentation of different crack patterns for a column loaded in compression [50]**

Tangential cracks occur at a distance from the load application point and propagate in the tangential direction. These tangential cracks are induced by high radial moments,  $m_r$ . Tangential cracks are equivalent to flexural cracks in one-way shear slabs. Radial cracks start close to the column face and propagate in direction of the edge of the slab. These cracks are induced by tangential moments,  $m_\varphi$ . Radial cracks and tangential moments are not found in one way shear structures. Both radial and tangential cracks start on the tensile side of the slab. The response of a concrete slab is strongly related to the crack development. S. Guandalini [25] described the crack development as a process which can be separated into four phases:

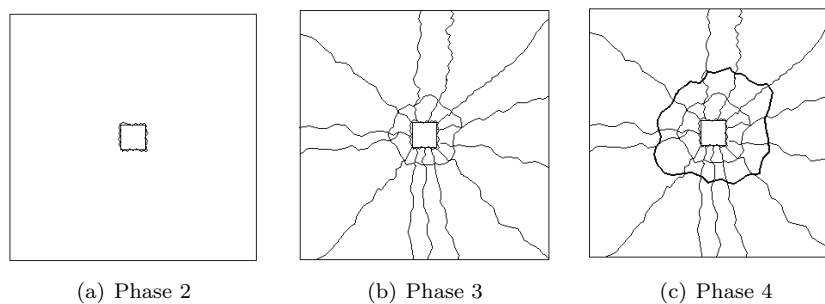
1. the linear elastic phase;
2. the phase of flexural response;
3. the phase of shear resistance;
4. the post-punching failure phase.

During the first phase no cracks are developed yet. The slab behaves linear elastic, so the tensile strength nor the compressive strength of the concrete are reached. After removing the applied load, the slab returns to its initial state. The slab response during this phase can be analysed with the elastic bending theory. This phase ends when the first crack arises which corresponds to the cracking load  $F_{cr}$ .

The second phase is initiated when the first flexural crack appears. This crack is a tangential crack located at top surface along the circumference of the column, see Figure 1.4(a). Under increasing load, radial cracks begin to form at the perimeter of the column and spread out toward the edge of the slab. This phase is completed once the first tangential crack is a stress-free crack.

After phase 2, the behaviour of the slab changes and shear resistance is mobilised. This shear behaviour is characterised by inclined cracks across the slab thickness. The shear resistance is not only influenced by the concrete strength but also by the shear reinforcement and the dowel action. During this phase, few new flexural cracks form, see Figure 1.4(c). However, existing cracks open and sudden unite into a single crack which is the punching crack. This is the end of the shear resistance phase.

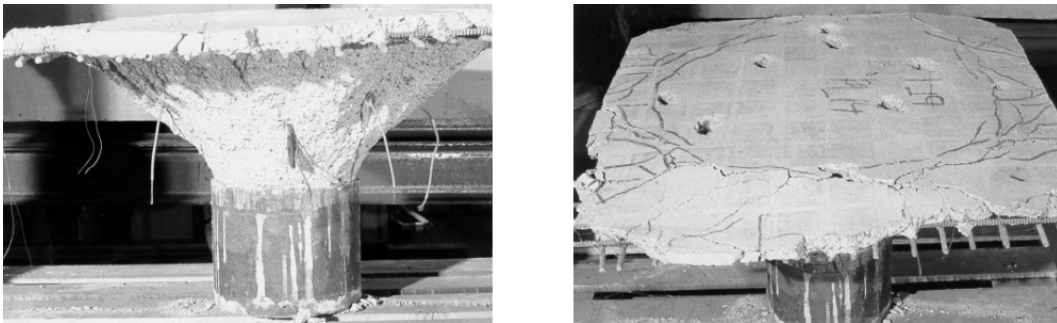
Suddenly, a truncated-cone-shaped element punches through the slab, see Figure 1.4(c). This failure crack appears at the same time as failure occurs. At failure, a cone is separated from the rest of the slab along the punching cracks and penetrates through the slab.



**Figure 1.4: Punching shear crack development, viewed from tensile face [25]**

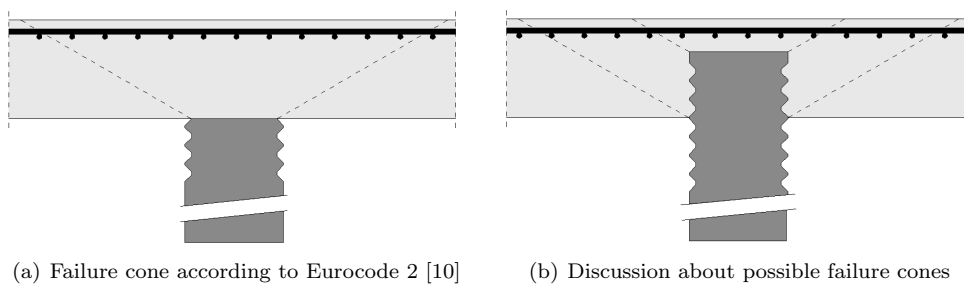
The punching shear strength of a slab depends on aspects like the slab height, span distances, loaded area, concrete strength and the amount of reinforcement. Openings and asymmetric spans influence the punching shear strength negatively. Punching shear failures are undesirable modes of failure since they give almost no warning and have disastrous consequences.

Figure 1.5 presents a clear visualisation of a punching cone element. The element appeared after punching shear tests on concrete footings conducted by M. Hallgren, S. Kinnunen and B. Nylander [36].



**Figure 1.5: Photos of a punching shear cone observed during experiments conducted by M. Hallgren et al. [36]**

The Eurocode 2 [10] design code for punching shear verification is based on concentrated forces acting on top side of a concrete slab. This code accounts for the full slab height in its verification expression, see Figure 1.6(a). The dotted line represents the fictitious shear plane angle which differs per country. The difference in shear angle between countries emphasise the variety of opinions about the occurring punching cone perimeter. Design codes for structural slabs are not clear about the effective slab height in case the concentrated force penetrates partly into the slab, like the situation of a penetrated foundation pile, see Figure 1.6(b). The question is which punching will occur.



(a) Failure cone according to Eurocode 2 [10]

(b) Discussion about possible failure cones

**Figure 1.6: Representation of punching shear cones, loaded in compression**

The same uncertainty counts for the Dutch design code CUR 77 [14] for underwater concrete verification. This code includes a punching shear verification for ribbed piles. This punching shear verification is based on foundation piles loaded in tension which is the case during the construction phase. The code doesn't include a verification method in case of compression forces during the exploitation phase.

### 1.3 Objective

The lack of a clear design approach causes a structural debate about this complex problem. That is something this thesis must change. So the objective reads:

*A study into the punching shear behaviour of structural slabs on top of ribbed foundation piles loaded in compression.*

The objective includes the question which punching cone element will occur, the small cone or the large cone shown in Figure 1.6(b). In order to find the answer, the study follows the next approach:

- a study into a legitimate numerical model to simulate the contact area of a ribbed pile and structural slab;
- a study into the influence of the pile - slab connection on the punching failure behaviour;
- a study into the influence of both bending and shear reinforcement on the punching failure behaviour;
- a study into the influence of the number of ribbed sides;
- a study into the influence of non symmetric load conditions on the punching failure behaviour.

### 1.4 Thesis outline

Chapter 1 includes a brief introduction to the punching shear failure phenomenon and the importance of this study.

Chapter 2 presents the relevant background information for a better understanding of the remaining thesis. This chapter consists mainly of various experimental and analytical studies.

In addition Chapter 2 presents several punching verification codes and the shear capacity of multiple concrete surface categories.

Chapter 3 includes a brief introduction to the finite element modelling principle. It presents the implemented numerical solution methods in the program ATENA.

Implemented material models are discussed in Chapter 4. This chapter is introduced to provide a brief background of the theory behind the finite element modelling.

Chapter 5 presents a validation study of a proper modelling technique for the contact area of the ribbed pile and the slab. Conclusions are drawn based on the comparison of numerical results with various experimental results.

Chapter 6 includes the analyses of the thesis objective. The punching shear behaviour is investigated based on a fictitious case study. A part of this chapter relates to the influence of additional reinforcement and the influence of non symmetric load conditions.

In Chapter 7 the conclusions and recommendations are given.

## Chapter 2

# Literature review

This chapter describes in general the current state of knowledge about the punching shear phenomenon. Experimental results together with analytical shear models are briefly discussed. The goal is to provide sufficient background information to be able to understand the remaining thesis.

### 2.1 Experimental studies

#### 2.1.1 Experiment of Elstner and Hognestad

In 1956, Elstner and Hognestad [46] investigated extensively the behaviour of relatively thin reinforced concrete slabs. They tested  $1830 \text{ mm}^2$  slabs, supported at the four edges and loaded up to failure by using a centrally located column, see Figure 2.1.

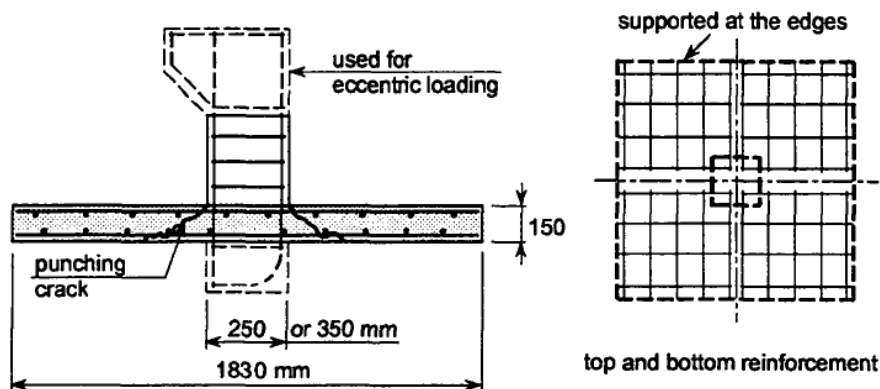


Figure 2.1: Setup of punching experiment Elstner and Hognestad [46]

The influence of the percentage of flexural reinforcement is illustrated in Figure 2.2(a) where the response curves are presented. The geometry of the tested slabs is left unchanged. In addition, along the response curves the load value  $P_{yield}$  is indicated, for which the first yielding of the reinforcement is measured on strain gages.

It is observed that slabs with a high percentage of reinforcement fail without warning, the so-called brittle failure.

This leads to the definition of two types of failure:

1. *flexural failure*, which is characterised by a rapid increase of the deflection for a slight increase of load;
2. *punching failure*, which characterised by a sudden failure along an inclined crack.

The influence of the concrete strength has been examined as well. This by varying systematically the compressive strength of concrete. In Figure 2.2(b) the response curves are represented, again without any change in slab geometry. The punching load increases from 355 kN to 546 kN with increasing concrete strength. The stiffness of the response is also increased. For slabs made of low compressive strength concrete, it is not possible to observe any yielding of the reinforcement because the punching shear failure occurs first.

The variable  $w$  and  $P$  at both axes from Figure 2.2 relates respectively to the relative vertical displacement measured at the edge of the tested slabs and the punching shear force.

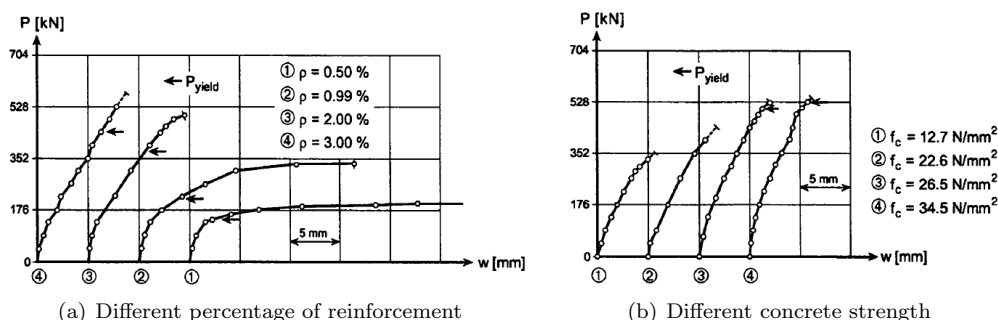


Figure 2.2: Results experiment of Elstner and Hognestad [46]

In case of a low reinforcement ratio, the strength of the slab is limited by its flexural capacity and punching failure occurs only after large plastic deformations. For intermediate reinforcement ratios, some yielding of the reinforcement is present, but punching occurs before yielding of the entire reinforcement. In this case, the strength of the slab is lower than its flexural capacity. For large reinforcement ratios, punching occurs before any yielding of the reinforcement takes place. In this case, the strength of the slab is lower than its flexural capacity.

### 2.1.2 Experiment of Bollinger

In 1985, Bollinger [7] investigated the behaviour of concrete slabs provided with different ring reinforcement layouts. The tested slab shown in Figure 2.3(a) was reinforced by concentric rings, placed at the boundary of the slab only. A second experiment is performed with an additional ring reinforcement in the critical region.

The experimental results shown in Figure 2.3(c) shows the role of the critical shear crack in punching shear strength of slabs. With a reinforcement layout like Figure 2.3(a), only radial cracks developed and the formation of circular cracks in the critical region was avoided. The

results of the second experiment with an additional ring reinforcement shows a decrease of the punching shear strength. For this test, the presence of the additional ring initiated the development of a crack in that region. The parameter  $\psi$  used in Figure 2.3(c) represents the vertical slab rotation with respect to the slab surface.

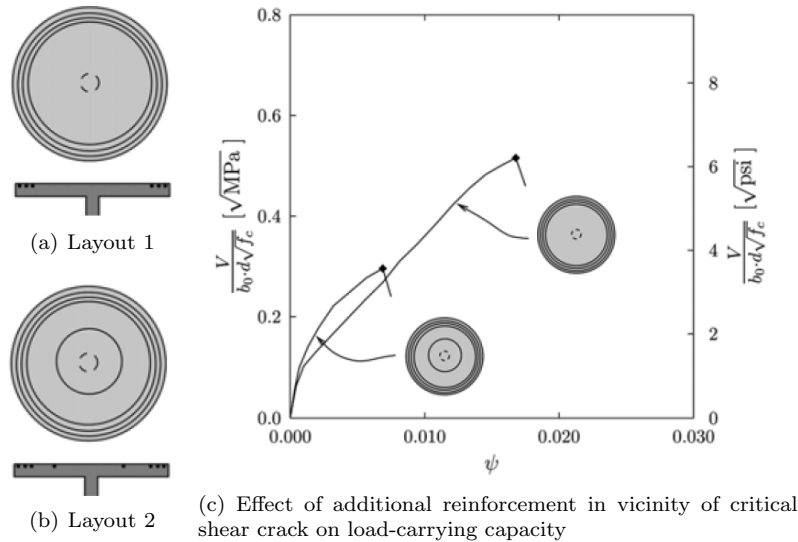


**Figure 2.3: Results experiment of Bollinger [7]**

The punching shear strength of the slab with reinforcement layout 1 and layout 2 are respectively 77.1 kN and 44.0 kN. This means a reduction of punching shear strength of approximately 43%.

### 2.1.3 Experiment of Kinnunen and Nylander

Kinnunen and Nylander [48] tested circular 150 mm thick slabs, 1840 mm in diameter, supported along the circumference and loaded on a column stub at the center. The influence of the reinforcement layout is demonstrated in Figure 2.4. One slab is made with ring reinforcement and the other is made with orthogonal reinforcement.

The overall behaviour of the two slabs are similar except for little differences like the shape of the punching shear crack and the crack pattern, shown in respectively Figure 2.4(b) and Figure 2.4(c).

It is observed that the shape of the punching crack is more inclined for the slab with ring reinforcement compared to the slab with orthogonal reinforcement. Besides the difference in the reinforcement layout, the percentage of reinforcement differs as well. These two dissimilarities results in a different shape of the punching crack.

In the slab with ring reinforcement, the tangential and the radial cracks can clearly be distinguished. The crack pattern of the slab with orthogonal reinforcement does not follow the tangential and radial geometry but looks more like a net, especially in the area near the column.

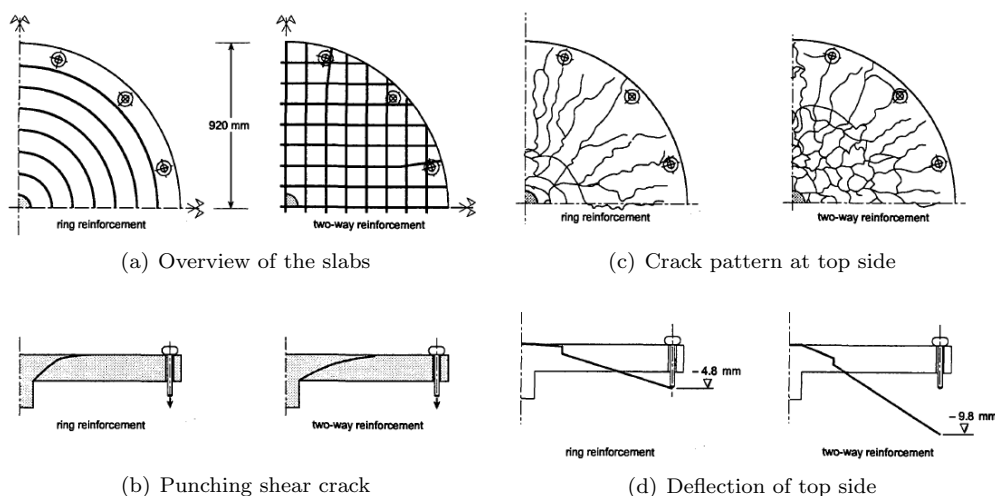


Figure 2.4: Results experiment of Kinnunen and Nylander [48]

The differences in crack patterns is explained by the fact that the state of stress in the slab with ring reinforcement is polar-symmetrical. Unlike the ring reinforcement, orthogonal reinforcement results in a state of stress that is orientated to the direction of the reinforcement. This direction results in a bi-directional stress state, which causes a different crack pattern.

The deflection of the top of the slab is also different between the two experiments as shown in Figure 2.4(d). For slabs with ring reinforcement less deflection is observed compared to the slab with orthogonal reinforcement. These difference in deflection illustrates that ring reinforcement inside the punching cone is stiffer than orthogonal reinforcement. This difference is caused by the dowel action of the reinforcement cutting across the punching shear crack. Dowel action is defined as a shear transfer mechanism between concrete and reinforcement where highly localised state of stress is observed [9]. For a slab made of orthogonal reinforcement, the punching shear crack intersects several reinforcement bars, whereas the other slab the punching crack intersects no bars.

#### 2.1.4 Experiment of Ka Lun Li

In 2000, K. Ka Lun Li [35] published a master thesis about the influence of size on punching shear strength failure of concrete slabs. The response of six two-way slab specimens, which were designed such that they would fail in punching shear, are investigated. The parameter introduced in the experiments is the thickness of the slab. The effects of this parameter on the shear strength is studied.

Six slab specimens are tested with an overall slab thickness  $h$  varying from 135 mm to 550 mm, while their widths varied from 925 mm to 1950 mm. The reinforcement was distributed uniformly along the width of the specimens. The specimens are numbered according to their effective depth e.g. specimen P100 corresponds to an effective depth of 100 mm.

Figure 2.5 consists of a table with a summary of the experimental results and a corresponding graph. It is observed that all specimens failed in punching shear.



From Figure 2.5, it can be seen that for effective depths up to 200 mm, the failure stress is relatively constant with a small increase. After a thickness of 200 mm the shear stress decreases as the effective depth increases. It is evident that for this test series, there is a significant size effect for effective depths greater than about 200 mm.

<i>Specimen</i>	$V_{max}$ [kN]	$V/b_0 d$ [N/mm <sup>2</sup> ]
P100	330	2.76
P150	583	2.78
P200	904	2.83
P300	1381	2.32
P400	2224	2.00
P500	2681	1.68

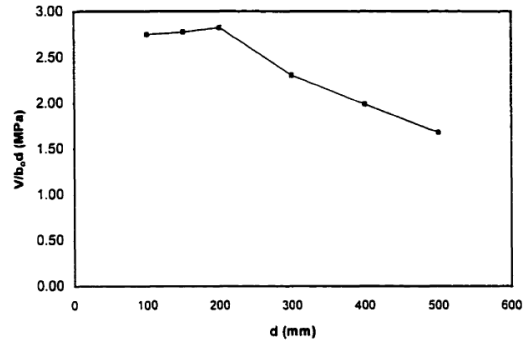


Figure 2.5: Results experiment of Ka Lun Li [35]

### 2.1.5 Experiment of Braam, Bosman and Van Rhijn

In 2004 C.R. Braam, A. Bosman and A. van Rhijn [16] performed a study into the failure behaviour of ribbed concrete piles embedded by a concrete slab under the action of tensile loading. The used concrete piles are prefabricated with internal or external ribs on two sides of the pile, the other two sides remained plane.

Figure 2.6 shows the result of the pull-out test of an external ribbed foundation pile (specimen number 2-1). It's clear to see that also when the pile is embedded into a slab, the typical cone shaped element appears after failure. This experiment confirms the expectations that the added application of ribbed sides have a positive effect on the shear strength along the pile face.



Figure 2.6: Punching shear cone element after failure [16]

Table 2.1 contains the geometry of all punching cones after failure. The crack slope  $\alpha$  is the average value of the left and right slope per cross-section. The slopes  $\alpha_1$  and  $\alpha_2$  are the slopes in respectively the  $R_1$  and  $R_2$  direction. The ribbed sides are orientated in the  $R_1$  direction and the plane sides are orientated in the  $R_2$  direction.

<i>Specimen</i>	<i>Rib geometry</i>	<i>Diam. in <math>R_1</math></i> [m]	<i>Diam. in <math>R_2</math></i> [m]	<i>Slope <math>\alpha_1</math></i>	<i>Slope <math>\alpha_2</math></i>
1-1	minimum	1,70	1,50	26°	30°
1-2	internal	1,20	1,20	29°	32°
2-1	minimum	1,60	1,45	29°	32°
2-2	external	1,65	1,35	27°	33°
3-1	maximum	1,75	1,35	26°	33°
3-2	internal	1,55	1,25	29°	36°

**Table 2.1: Diameters and the average internal crack slopes**

During the determination of the cone diameter, the top part of 150 mm is not taken into account. This due to the fact that the slope at this point decreases rapidly. This decrease in slope may cause local rupture at the end of the punching cone. This local rupture happened to the left part of the cone from Figure 2.6. The authors expect that this small local rupture will not have a significant influence on the pull out strength and that this is not representative for the slope of internal cracks.

The results from Table 2.1 show that the influence of internal ribs and external ribs seems to make no difference on the crack slopes  $\alpha_1$  and  $\alpha_2$ . All diameters and slope angles are in the same order of magnitude. Otherwise, the length of  $R_1$ , orientated along the ribbed sides, has in almost all the experiments a higher magnitude compared to the magnitude of  $R_2$ . This leads to the conclusion that the ribbed sides do have a better shear behaviour compared to the plane sides. It is noticeable that also the plane sides benefit from the ribbed sides, despite the fact the crack angle is steeper, the plane sides account for a large extend in the failure strength. The experiment with maximum internal ribs shows a larger distinction in results between the sides with and without ribs.

The results of all the pull out tests are shown in Table 2.2, together with the theoretical failure load according to CUR 77 [14].

<i>Specimen</i>	<i>Rib geometry</i>	<i><math>f_{ctm,o}</math></i> [MPa]	<i><math>F_u</math> experiment</i> [kN]	<i><math>F_u</math> theory</i> [kN]	<i>Ratio</i> [-]
1-1	minimum	2,90	2483	374	6,6
1-2	internal	2,30	2373	297	8,0
2-1	minimum	2,50	2399	323	7,4
2-2	external	2,40	2329	310	7,5
3-1	maximum	2,30	2421	320	7,6
3-2	internal	2,15	2179	299	7,3

**Table 2.2: Failure load comparison based on experimental data and the theory**

The theory underestimates the capacity of all pull out tests significantly. In general, the experimental capacity is more than seven times the theoretical capacity. This statement requires a remark. After reaching the failure load, a fully developed cone element appeared.

A likely conclusion is that a pile with ribs at all sides would not increase the pull out strength significantly, while the failure load of the theoretical approach is twice as high. What remains is that the experiment/theory ratio is still about a factor three to four. Another aspect is the presence of a prestressing force during the experiment. The CUR 77 verification code doesn't include a prestressing factor. It is expected that this resulted in increased pull out forces.

### 2.1.6 Discussion

Based on the analyses of the experiments given in section 2.1, several parameters can significantly influence the shear capacity of structural slabs. The most important parameters are mentioned in this section.

Increasing the flexural reinforcement has significant positive effects on the punching shear capacity, see section 2.1.1. This experiment shows that changes in the amount of reinforcement has also major consequences for the behaviour of the total mechanism. The degree of yielding at failure ranged from none for slabs with a high reinforcement ratio, to practically full yielding for slabs with low reinforcement ratios. In other words, the ductility decreases by higher reinforcement ratios. Increasing the amount of reinforcement makes the mechanism more stiff and decreases the vertical displacement of the slab. The layout of the reinforcement bars is an important aspects as well, shown in section 2.1.2.

Also the concrete compressive strength is an important factor in the punching strength. As the concrete compressive strength increases, the punching shear capacity increases as well, as shown in Figure 2.2(b). In 2008, Metwally et al. [28] proposed that the increase of capacity as function of the compressive strength is less than the rate of  $\sqrt{f_c}$  as introduced by the ACI 318-08 code [1]. Metwally et al. found an increase in the order of  $\sqrt[3]{f_c}$  as included in the EC 2 [10] code expression.

The size-effect in punching failure was revealed with the experiments performed by Ka Lun Li in section 2.1.4. This experiment shows that the nominal stresses of a relative thin slab is higher compared to the nominal stress of a relative thick slab. Another experiment carried out by Bažant and Cao [56] concluded the same size-effect phenomenon. This experiment also studied the behaviour of the slab after reaching the peak load. A thick slab shows little softening after reaching the peak, whereas a thin slab exhibits an softening response after the peak. The load-deflection curve of a thin slab is similar to an elastic perfectly plastic behaviour, while the curve of a thick slab looks like a direct tension test. Bažant and Cao concluded that the behaviour of a thick slab being brittle is related to linear elastic fracture mechanics, while the thin slab behaves more close to the plasticity theory.

## 2.2 Analytical studies

Different punching shear models are proposed in the past years, all with a different approach. The analytical model of Talbot [5], Kinnunen and Nylander [48], Nielsen [42] and Muttoni [4] are briefly discussed. This section will give a clear view of the differences in analytical approaches.

### 2.2.1 The model of Talbot

In 1913 Talbot [5] proposed a model to determine the punching shear strength of slabs. The model of Talbot is also known as *the control surface model*. This simplified model is based on the definition of the nominal shear stress, which is calculated by dividing the punching load by the circumferential surface of the element. The strength of the concrete slab is verified by comparing this nominal shear stress with a reference shear stress which depends on the characteristic properties of concrete.

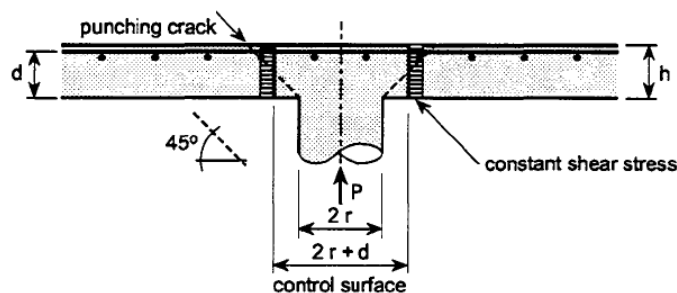


Figure 2.7: The analytical model of Talbot [5]

The area of this cylinder is highly discussable and has been the subject of some debate. The different points of view on the diameter are discussed in section 2.3. In most codes the diameter of the perimeter is a function of the effective depth of the slab. The effective depth is defined as the distance from the centroid of the reinforcement to the compression face of the concrete. The control perimeter of the cylinder is defined with parameter  $u$ . In case the punching load concerns a circular shaped column, like Figure 2.7, the nominal shear stress introduced by Talbot becomes:

$$\tau_n = \frac{F}{u d} = \frac{F}{\pi(2r + d) d} \quad (2.1)$$

Where	$\tau_n$	= nominal shear stress	[N/mm <sup>2</sup> ]
	$F$	= load	[N]
	$u$	= control perimeter	[mm]
	$r$	= radius column	[mm]
	$d$	= effective depth	[mm]

This model is based on the assumption of a constant nominal shear stress over the slab height. Further extension of this model is possible by introducing empirical factors which depend for example on the amount of longitudinal reinforcement, slab geometry and shape of the column.

### 2.2.2 The model of Kinnunen and Nylander

The derivation of this model is based on the 61 experiments performed in 1960 on circular slabs with circular columns [48]. The results of these tests are discussed in section 2.1.3. The observations of these tests, especially the formation of shear cracks, the deformations and the expansion of the concrete and reinforcing bars are important fundamentals of their theory.

The theory is based on the fact that in statics all forces on a single element are in equilibrium. A small slice is cut out from the slab and is represented as a stiff sector. The rigid segment is limited at the sides by two radial cracks and at the front by a tangential shear crack. This segment turns around a centre of rotation located at the the root of the tangential crack. The failure criterion is defined by the ultimate shear expansion of the concrete at the bottom of the slab. The theory is from origin derived for concrete slabs with ring reinforcement and is expanded to slabs with flexural reinforcement by introducing a correction factor  $\kappa$  to compensate the dowel action. In case a rectangular column is used, the circumference must be transposed into the corresponding circumference of a circular column.

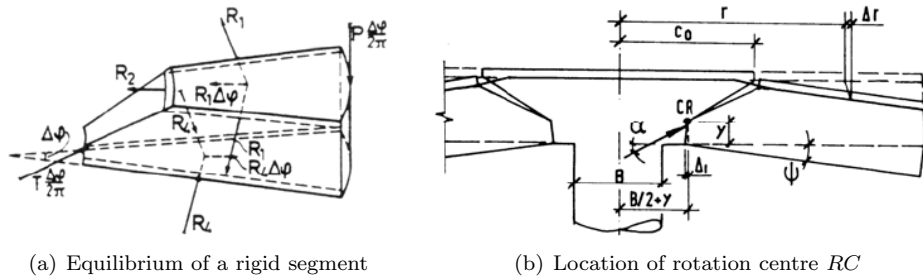


**Figure 2.8: The analytical model of Kinnunen and Nylander [48]**

To get the predicted ultimate punching load of concrete slabs without shear reinforcement, equation 2.2 and equation 2.3 have to be set equal by an iteration on the ratio of the concrete compression zone  $k_x$ . Equation 2.2 for the determination of  $V_u$ , is derived by setting  $\Sigma V = 0$ . It is noticeable that this equation depends on the ultimate concrete stress  $\sigma_{cu}$ .

$$V_u = \kappa \pi \eta d^2 k_x \frac{1 + \frac{2k_x}{\eta}}{1 + \frac{k_x}{\eta}} \sigma_{cu} \left( \frac{\tan \alpha (1 - \tan \alpha)}{1 + \tan^2 \alpha} \right) \quad (2.2)$$

Where	$V_u$	= ultimate shear force	[N]
	$\kappa$	= correction factor for dowel action	[-]
	$\eta$	= size factor	[-]
	$d$	= effective depth	[mm]
	$k_x$	= ratio of concrete compression zone	[-]
	$\sigma_{cu}$	= ultimate concrete stress	[N/mm <sup>2</sup> ]
	$\alpha$	= inclination of conical shell	[°]

Equation 2.3 depends on the yield stress of the used reinforcement bars, the ratio of reinforcement and the shape. This equation is derived by making use of moment equilibrium

$\Sigma M = 0$ . Three different cases have to be considered in dependence on the location where the yield stress of the steel is reached. Equation 2.3 is based on the case that the yield stress is reached inside the area of the conical shell.

$$V_u = \kappa 4 \pi \rho f_y d r_j \left[ 1 + \ln \left( \frac{l_{slab}}{2r_u} \right) \right] \frac{1 - \frac{k_x}{3}}{(l_{slab}/d) - \eta} \quad (2.3)$$

Where	$\rho$	= reinforcement ratio	[-]
	$f_y$	= yield stress reinforcing steel	[N/mm <sup>2</sup> ]
	$r_j$	= radius circular area inside the shell	[mm]
	$l_{slab}$	= length of the slab	[mm]
	$r_u$	= ultimate shell radius	[mm]

So far, the Kinnunen and Nylander model remains one of the best models for the phenomenon of punching. Recently, Broms [8] and Hallgren [26] proposed some improvements to account for high strength concrete and size effects. While this proposal led to good results, this model was never directly included in building codes because its application is too complex.

### 2.2.3 The model of Nielsen

The analytical model of Nielsen [42] is published in 1976 and is based on the theory of plasticity. The next basic assumptions are supposed:

1. concrete is a perfectly plastic material;
2. the failure criterion is based in Coulomb's law, see section 2.4;
3. the concrete tensile strength is very low.

The ultimate punching force is calculated by making use of the law of conservation of energy, the work performed by the applied loads is equal to the amount of fracture energy of the conical shell. The shape of the conical shell is described by a straight line and a catenary shaped line, see Figure 2.9.

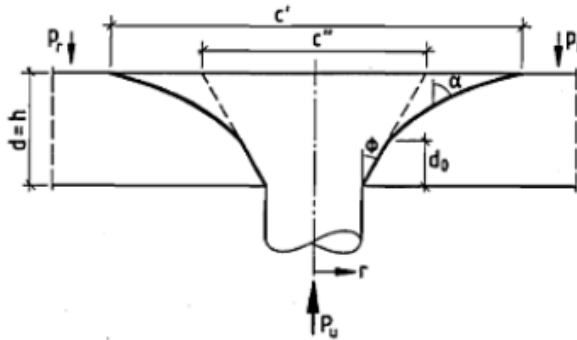


Figure 2.9: The analytical model of Nielsen [42]

This model is set by an iterative variation calculation which gives the factors  $A$ ,  $B$  and  $C$ . Equation 2.4 describes the cracking force of the conical shell element and equation 2.5 describes the cracking force of the catenary shell. The ultimate force  $F_u$  is defined by the summation of equations 2.4 and 2.5:

$$V_{u1} = 0.5 \pi f_c d_0 (c'' + d_0 \tan \phi) \frac{1 - \sin \phi}{\cos \phi} \quad (2.4)$$

$$V_{u2} = 0.5 \pi f_c \left[ k_2 C (d - d_0) + k_2 \left( \frac{c'}{2} \sqrt{\frac{c'^2}{4} - C^2} - AB \right) - k_3 \left( \frac{c'^2}{4} - A^2 \right) \right] \quad (2.5)$$

Where	$V_{ui}$	= ultimate shear force, i=1,2	[N]
	$f_c$	= concrete compressive strength	[N/mm <sup>2</sup> ]
	$d_0$	= height of equal conical and catenary shell	[mm]
	$c'$	= catenary shell diameter	[mm]
	$c''$	= conical shell diameter	[mm]
	$\phi$	= angle conical shell	[°]
	$k_i$	= material constants, i=2,3	[-]

The assumption that concrete is a perfectly plastic material is a significantly simplification of the mechanical behaviour of concrete. The ratio of reinforcement is also not considered in this model.

### 2.2.4 The model of Muttoni

As shown in Figure 2.2(a), the punching strength of a concrete slab decreases with an increasing slab rotation. This correlation is has been explained by Muttoni and Schwartz [4] as follows: the shear strength is reduced by the presence of a critical shear crack that propagates through the slab into the inclined compression strut carrying the shear force to the column.

The experiment performed by Bollinger, see section 2.1.2, emphasises this shear crack theory. The experimental results show the role of the critical shear crack in punching shear strength of slabs. With a reinforcement layout like Figure 2.3(a), only radial cracks developed and the formation of circular cracks in the critical region was avoided. The results of the experiment with an additional ring reinforcement shows a decrease of the punching shear strength. For this test, the presence of the additional ring initiated the development of a crack in that region.

The opening of the critical shear crack reduces the strength of the inclined concrete compression strut carrying the shear stress. This reduction eventually leads to the punching failure. According to Muttoni and Schwartz [4], the width of the crack can be assumed to be equivalent to the product of the slab rotation and effective depth,  $\psi d$ . This assumption was the base of the semi-empirical failure criterion formulated in 1991 as:

$$\frac{V_R}{b_0 d^3 \sqrt{f_c}} = \frac{1}{1 + \left( \frac{\psi d}{4} \right)^2} \quad (2.6)$$

Where	$V_R$	= shear force resistance	[N]
	$b_0$	= perimeter of critical section	[mm]
	$d$	= effective depth	[mm]
	$f_c$	= concrete compressive strength	[N/mm <sup>2</sup> ]
	$\psi$	= slab rotation	[rad]

In 2003 Muttoni [40] proposed an improved formulation for the failure criterion. This improved formulation, according to Walraven [52], takes into account the roughness of the crack and its capacity to transfer shear forces. Two extra parameters are introduced to the formulation, the maximum aggregate size and a reference aggregate size.

$$\frac{V_R}{b_0 d^3 \sqrt{f_c}} = \frac{3/4}{1 + 15 \frac{\psi d}{d_{g0} + d_g}} \quad (2.7)$$

Where	$d_{g0}$	= reference aggregate size	[mm]
	$d_g$	= maximum aggregate size	[mm]

Figure 2.10 compares the the results of 99 punching tests [41] with equation 2.7. In this figure, the slab rotation  $\psi$  is multiplied by the factor  $d/(d_{g0} + d_g)$  to cancel the effects of the slab thickness and aggregate size.

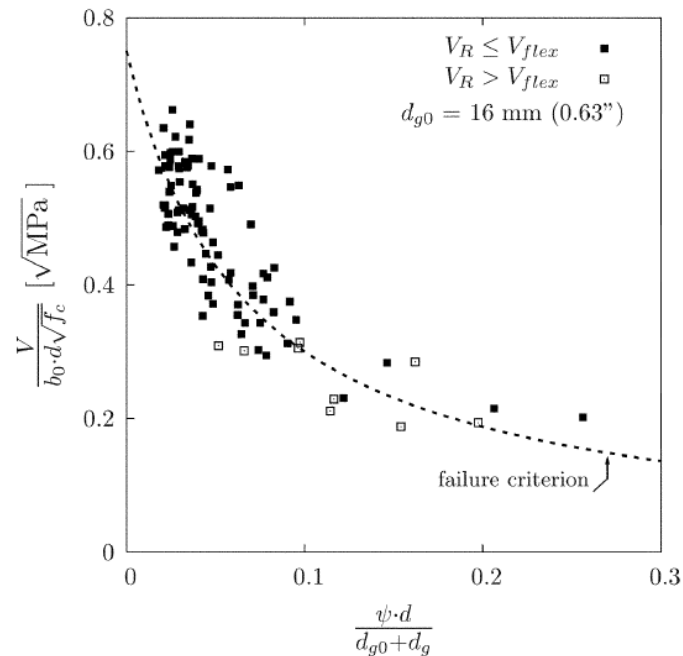


Figure 2.10: The analytical model Muttoni [40]



To enable a punching shear calculation according to equation 2.7, Muttoni [40] proposed a load-rotation relationship given by the next expression.

$$\psi = 0.33 \frac{L}{d} \frac{f_y}{E_s} \left( \frac{V_d}{8 m_{Rd}} \right)^{3/2} \quad (2.8)$$

Where	$L$	= axis to axis spacing of column	[mm]
	$f_y$	= yield stress reinforcing steel	[N/mm <sup>2</sup> ]
	$E_s$	= elastic modulus of reinforcing steel	[N/mm <sup>2</sup> ]
	$V_d$	= design shear force	[N]
	$m_{Rd}$	= flexural capacity of the slab	[N]

Equation 2.8 is formulated for intermediate columns. For corner columns the constant 8 needs to be replaced by 2 and for edge columns it needs to be replaced by 4. Equation 2.7 is a bit adjusted to reach a target fracture of 5% and to include a model factor to cover irregularities in span lengths and disposition of the loading. Also a partial safety factor of concrete ( $\gamma_c = 1.5$ ) is introduced.

$$\frac{V_{Rd}}{b_0 d^3 \sqrt{f_c}} = \frac{2}{3\gamma_c} \frac{1}{1 + 20 \frac{\psi d}{d_{g0} + d_g}} \quad (2.9)$$

The design procedure starts by calculating the factored slab rotation  $\psi_d$  by using equation 2.8. From that value, the corresponding punching shear strength of the slab (point B of Figure 2.11) is found by making use of equation 2.9. The design is safe when the strength obtained by equation 2.9 is larger than the design shear force  $V_d$ .

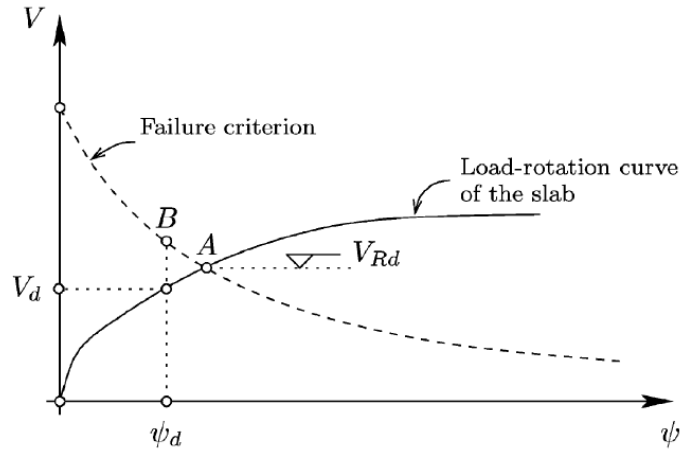


Figure 2.11: Design procedure to check punching shear strength

### 2.2.5 Discussion

The analytical model of Talbot is one of the simplest models for punching shear verification. Cone-shaped-element is replaced by a cylindrical element. The interpretation of the size of this cylinder depends on the used design code. It is a simple model without any iteration procedures and therefore introduced in many codes as the basis of the punching verification.

The Kinnunen and Nylander model served as a basis for the Swedish and Swiss design codes of the 1960s. While this model is leading to good results, this model was never directly included in design codes because its application is too complex.

The model of Nielsen is an model with good verification results in case of ultimate punching forces. Present reinforcement is not taken into account, which is a disadvantage of this model. The assumption that concrete is a perfectly plastic material is a significantly simplification, and therefore not often used in practise.

The model proposed by Muttoni is an alternative model where the slab rotation is the leading parameter instead of the maximum shear stress. This model reflects the same rotation behaviour observed by 99 punching experiments. It is a complex model in case a maximum punching shear strength must be calculated, because it is an iterative procedure. There er is simpler method to verify the acting shear force.

## 2.3 Punching shear verification

Although extensive research has been done on punching shear of slabs, to date there is still no generally applicable, rational theory. The current building code design procedures are mainly based on empirical studies [39]. This because punching shear is a three-dimensional problem and several simplifications are thus generally adopted.

The discussed design provisions are the American Concrete Institute 318-08 (ACI 318-08), the Eurocode 2 (EC 2), the British Standard 8110 (BS 8110) and the Civieltechnisch Centrum Uitvoering Research en Regelgeving 77 (CUR 77) [1, 2, 10, 14].

The ACI 318-08, EC 2 and BS 8110 codes are developed for cases where the applied force, like a column, acts at the surface of the slab. The CUR 77 is a different code and is used specially for ribbed foundation piles where the pile face is, fully or partly, embedded by an underwater concrete slab.

The ACI 318-08, EC 2 and BS 8110 are all making use of the Talbot model, see section 2.2.1 for the explanation of parameters and the background behind this analytical model.

The design codes EC 2 and BS 8110 proposes empirical factors in their design formulas for estimating the punching shear capacity in slabs without transverse reinforcement. The EC 2 and BS 8110 expressions are written in terms of the concrete compressive strength, size effect factor and reinforcement ratio in orthogonal directions. The size effect is defined as the decreasing nominal shear strength with increasing size of the member [10]. The design code ACI 318-08 adopts a simpler expression in which the flexural moment reinforcement and size effect factors are neglected, so the shear strength is assumed to be constant.

With respect to punching shear in non-axis-symmetrical conditions, theoretical or empirical approaches usually extend the axis-symmetry formulation by correcting it with a series of factors. Reworking of the theoretical approach is typically not performed [33]. Asymmetrical conditions could be the result of a non-uniform reinforcement layout, eccentric loading and/or an asymmetrical slab or column geometry. These additional factors are not included during the design code study.

### 2.3.1 ACI 318-08

The ACI 318-08 code considers a critical section located at a distance  $d/2$  from the periphery of the concentrated load. The shape of the perimeter depends on the geometry of the column and is rectangular for rectangular columns.

The concrete punching shear capacity according to ACI 318-05 is given by equation 2.10.

$$V_R = \frac{1}{3} b_0 d \sqrt{f_c} \quad (2.10)$$

Where	$V_R$	= shear force resistance	[N]
	$b_0$	= perimeter of critical section	[mm]
	$d$	= effective depth	[mm]
	$f_c$	= concrete compressive strength	[N/mm <sup>2</sup> ]

### 2.3.2 EC 2

EC 2 considers a critical section located at a distance  $2d$  from the periphery of the concentrated load. The shape of the perimeter is straight along the sides with round corners.

The concrete punching shear capacity according to EC 2 is given by equation 2.11.

$$V_R = 0.18 \left[ 1 + \sqrt{\frac{200}{d}} \right] b_0 d (100 \rho_l f_{ck})^{1/3} \quad (2.11)$$

Where	$V_R$	= shear force resistance	[N]
	$b_0$	= perimeter of critical section	[mm]
	$d$	= effective depth	[mm]
	$\rho$	= bending reinforcement ratio, $\neq 0.02$	[-]
	$f_{ck}$	= characteristic concrete compressive strength	[N/mm <sup>2</sup> ]

It is noticeable that the part between the straight brackets accounts for the size factor. This was discussed in section 2.1.4.

### 2.3.3 BS 8110

BS 8110 considers a critical section located at a distance  $1.5d$  from the periphery of the concentrated load. The shape of the perimeter is straight along the sides with straight corners. The BS 8110 codes includes also a size factor, but with a different expression compared to the EC 2 code.

The concrete punching shear capacity according to BS 8110 is given by equation 2.12.

$$V_R = 0.27 \left[ \sqrt[4]{\frac{400}{d}} \right] b_0 d (100 \rho_l f_{cu})^{1/3} \quad (2.12)$$

Where	$V_R$	= shear force resistance	[N]
	$b_0$	= perimeter of critical section	[mm]
	$d$	= effective depth	[mm]
	$\rho_l$	= bending reinforcement ratio, $\neq 0.02$	[-]
	$f_{cu}$	= ultimate concrete compressive strength	[N/mm <sup>2</sup> ]

### 2.3.4 CUR 77

CUR Recommendation 77 contains design rules for unreinforced underwater concrete slabs. This recommendation gives a prediction about the pull out strength of a ribbed tension pile in underwater concrete:

$$F_u = 0.8 f_b n D(h - a_r) \quad (2.13)$$

Where	$F_u$	= ultimate load	[N]
	$f_b$	= concrete tensile strength	[N/mm <sup>2</sup> ]
	$n$	= number of ribbed sides	[-]
	$h$	= slab height	[mm]
	$a_r$	= distance between the ribs	[mm]

### 2.3.5 Discussion

The design approaches to the punching shear capacity found in ACI 318-08, EC 2 and BS 8110 show some similarities and dissimilarities.

All the models propose a sectional approach based on the check of shear stresses on a critical control perimeter at a given distance from the column. ACI 318-08 considers a control perimeter located at a constant distance  $d/2$  from the column while EC 2 consists in checking all the perimeters located between the column up to a distance  $2d$ , taking the weakest perimeter as the designing one. This approach is more complicated but it permits to get rid of variations in strength prediction occurring with a constant control perimeter when the geometry of the slab is slightly changed.

The three codes consider that the uplift loads applied inside the critical control perimeter can be subtracted to the shear force taken into account.

A study performed by Sagasetta et al. [33] shows that the prediction models according to EC 2, BS 8110 and ACI 318-08 are reasonable. The EC 2 formula provided the most accurate predictions whereas the BS 8110 method gave slightly more conservative results. The ACI 318-08 formula provided the largest scatter in the predictions, proven by the high coefficient of variation between the results. This is not a surprise since the ACI formula neglect the presence of reinforcement and doesn't take into account a size factor.

The ACI 318-08 is also the most conservative code with an average ratio value of 1.2 times the actual strength. All results are shown in Figure 2.12. The solid dots and triangles represents experiments where shear failure was governing and the empty dots and triangles represents experiments where flexure failure was governing.

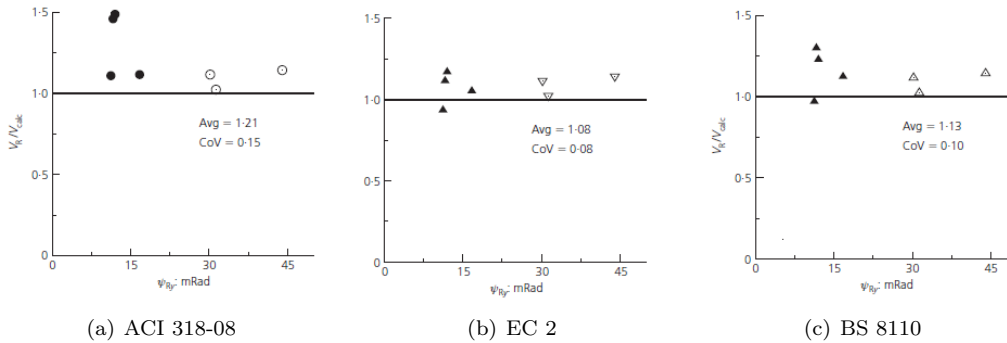


Figure 2.12: Comparison between design codes according to Sagasetta [33]

Another comparison was performed by Muttoni in 2008 [41]. Muttoni compared 87 experimental results with the design codes ACI 8318-08 and EC 2, see Figure 2.13.

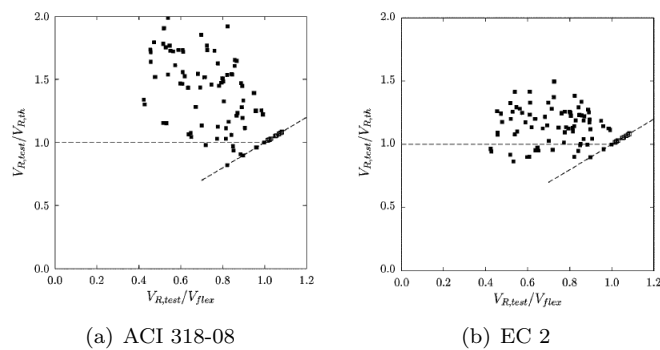


Figure 2.13: Comparison between design codes according to Muttoni [41]

The results shown in Figure 2.13 show the same trend as the results from Figure 2.12. The ACI 318-08 shows a great scatter in results compared to the EC 2 results. The lack of a size factor and reinforcement factor in the ACI 318-08 expression could be the explanation of this scatter.

## 2.4 Interface between concrete cast at different times

To verify the capacity of the interface between prefabricated concrete and in-situ concrete, it is essential to know the shear stress capacity of this joint. Several experiments were performed about the shear behaviour of smooth and toothed contact surfaces in the past. The considered codes and guidelines are based on the shear failure criterion of Mohr-Coulomb. Each formula uses each own coefficients, obtained experimentally. The Mohr-Coulomb criterion [22] consists of a shear failure area according Coulomb's law of friction and the fail hypotheses according to Mohr, see Figure 2.14. The shear failure area described by Coulomb depends on the next components:

- *cohesion*, this is the force of attraction between two layers of concrete and is formed by a combination of a chemical reaction and micro roughness on both sides of the concrete;
- *coefficient of friction*, which describes the ratio of the force of friction between two bodies and the force pressing them together.

Mohr-Coulomb criterion for negative values of compression stress is given with the next expressions corresponding to Figure 2.14:

$$\tau = c - \sigma_c \tan(\phi) \quad (2.14)$$

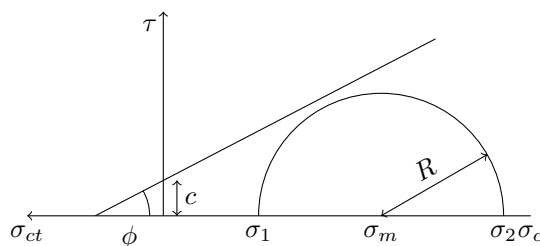


**Figure 2.14: The Mohr-Coulomb shear failure criterion**

Where	$\tau$	= shear stress	[N/mm <sup>2</sup> ]
	$c$	= cohesion	[N/mm <sup>2</sup> ]
	$\sigma_c$	= principal compressive stress	[N/mm <sup>2</sup> ]
	$\phi$	= angle of internal friction	[°]
	$\sigma_u$	= ultimate compressive stress	[N/mm <sup>2</sup> ]
	$\sigma_1$	= minimum negative principal stress	[N/mm <sup>2</sup> ]
	$\sigma_2$	= maximum negative principal stress	[N/mm <sup>2</sup> ]

With increasing stress, the circle radius  $R$  will increase and the circle will shift to the right due to an increased  $\sigma_m$ . Shear failure occurs in case the circle intersects the Coulomb part of the failure criterion.

### 2.4.1 EC 2

The EC 2 section 6.2.5 proposes the following formula to calculate the maximum shear resistance among reinforced concrete joints:

$$v_{Rdi} \leq c + \mu \sigma_n + \rho f_{yd} (\mu \sin \alpha + \cos \alpha) \quad (2.15)$$

Where	$v_{Rdi}$	= design shear resistance at the interface	[N/mm <sup>2</sup> ]
	$c$	= cohesion	[N/mm <sup>2</sup> ]
	$\sigma_n$	= normal compressive stress	[N/mm <sup>2</sup> ]
	$\mu$	= friction coefficient	[-]
	$\rho$	= reinforcement ratio	[-]
	$f_{yd}$	= design yield stress of reinforcement steel	[N/mm <sup>2</sup> ]
	$\alpha$	= angle of indentations, limited by $45^\circ \leq \alpha \leq 90^\circ$	[°]

The factors  $c$  and  $\mu$  depend on the surface class and are shown in Table 2.3. The factor  $c$  correlates to the force of attraction between two materials, and  $\mu$  correlates to a friction constant which describes the ratio of the force of friction between two bodies. The code makes a distinction between the next surfaces conditions:

- *very smooth*, a surface cast against steel, plastic or specially prepared wooden moulds;
- *smooth*, a slipformed or extruded surface, or a free surface left without further treatment after vibration;
- *rough*, a surface with at least 3 mm roughness at about 40 mm spacing, achieved by raking, exposing of aggregate or other methods giving an equivalent behaviour;
- *indented*, a surface with indentations complying with Figure 2.15.

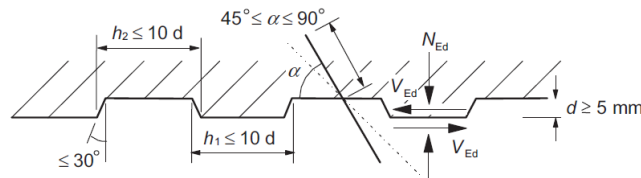


Figure 2.15: Indented construction joint [10]

Surface class	Cohesion [N/mm <sup>2</sup> ]	Friction coefficient [-]
Very smooth surface	0.025 $f_{ctd}$	0.5
Smooth surface	0.20 $f_{ctd}$	0.6
Rough surface	0.4 $f_{ctd}$	0.7
Indented surface	0.5 $f_{ctd}$	0.9

Table 2.3: Cohesion and friction coefficient according to EC 2 section 6.2.5 [10]

### 2.4.2 FIP

The Fédération Internationale de la Précontrainte (FIP) committee for prefabrication has made recommendations for the verification of shear stresses [43]. The committee distinguished ten categories based on its roughness. Category one represents for a very smooth surface and category ten represents a toothed surface. The FIP divided the ten categories into two groups:

- *Category A*, roughness category 1 to 6;
- *Category B*, roughness category 7 to 10.

The FIP recommends for each category the coefficients for the cohesion and friction constant.

<i>Category</i>	<i>Cohesion</i> [N/mm <sup>2</sup> ]	<i>Friction coefficient</i> [-]
Category A	0.2 $f_{td}$	0.6
Category B	0.4 $f_{td}$	0.9

**Table 2.4: Cohesion and friction coefficient according to FIP [43]**

### 2.4.3 Daschner

In 1986, Daschner [20] performed a study to the relation between the roughness and shear strength of a contact surface. Daschner studied also the verification model proposed by the FIP. The experiments include reinforced and unreinforced contact areas. One of Daschner intentions was to analyse the extent to which the FIP model was safe enough. The most important conclusions were:

- the FIP committee design categories are valid, see Table 2.4;
- the presence of normal compressive stresses proved to be a substantial influence factor to the shear capacity of a concrete joint;
- the quantity of the tying reinforcement also influenced the structural behaviour strongly in a positive manner.

For this thesis only the properties of smoothed and toothed surfaces are of importance. Daschner found for these surfaces the next values for the cohesion and friction constant:

<i>Category</i>	<i>Cohesion</i> [N/mm <sup>2</sup> ]	<i>Friction coefficient</i> [-]
Smooth surface	0.6	1.1
Toothed surface	1.5	1.7

**Table 2.5: Cohesion and friction coefficient according to Daschner [20]**



#### 2.4.4 Nissen

The values for cohesion and the friction coefficient were also experimentally investigated by Nissen et al. [29]. They measured larger values compared to design codes, both for the cohesion and the coefficient of friction, for a surface which was combed by a steel rake, see Table 2.6.

<i>Category</i>	<i>Cohesion</i> [N/mm <sup>2</sup> ]	<i>Friction coefficient</i> [-]
Combed surface	1.69	1.54

**Table 2.6:** Cohesion and friction coefficient according to Nissen et al. [29]



## Chapter 3

# Finite element modelling

Finite element modelling (FEM) is a method to study the behaviour of complex structures by making use of computer simulations. This method is based on solving a large matrix of partial differential equations.

FEM is developed during the fifties and its use increased rapidly during the eighties. The reason for the slow start was the lack of computer capacity.

### 3.1 Non-linearity

During a FEM analysis, the structure is divided into a finite number of elements. The behaviour and properties are described in so called integration points. These point are located inside an element and the number of integration points per element depends on the complexity and accuracy of the analysis. Each element is connected to its neighbouring element by nodes. At these nodes equilibrium conditions are solved by means of algebraic equations. FEM is applicable for linear and non-linear analyses. In a non-linear FEM analysis it is possible to follow the non-linear structural responses throughout the loading history. The load history is programmed as the load divided into several load increments. A mathematical description of the structural response is presented by a system of algebraic equations:

$$\underline{K} \underline{p} = \underline{f} \quad (3.1)$$

Where  $\underline{K}$  is the stiffness matrix  
 $\underline{p}$  is the displacement vector  
 $\underline{f}$  is the unknown internal force vector

Three different types of non-linearity in structural mechanics are distinguished:

1. material non-linearity;
2. geometric non-linearity;
3. boundary non-linearity.

A material non-linearity analysis is executed in case the material properties are e.g. a function of time, temperature or maturity. Examples are non-linear elasticity, plasticity and cracking. A geometric non-linearity analysis is executed in case the deformation is large enough that equilibrium equations must be written with respect to the deformed structural geometry. During this analysis the loads may change direction or magnitude. Boundary non-linearity is when the displacement depends on boundary conditions. The most frequent boundary non-linearities are encountered in contact problems. Example of contact problems are gap openings, possible sliding with frictional forces and situations where the contact area changes in time.

## 3.2 Numerical solution methods

In order to solve the system of non-linear equations, see equation 3.1, iterative solution methods are used. The scope of these solution methods is to find, within a certain error, a numerical solutions to the system of algebraic equations that correlate the external forces to the structural response:

$$f_{ext} = f_{int} + \varepsilon_{error} \quad \text{with} \quad \varepsilon_{error} \ll 0.1 \quad (3.2)$$

ATENA makes use of the next two default solution methods to carry out the iteration process:

- Newton-Raphson Method;
- Arc Length Method.

Both methods can be enhanced by means of the *Line Search* iteration.

### 3.2.1 The Newton-Raphson iteration

The Newton-Raphson (NR) iteration is an iterative solution method. The Newton Raphson method can be used for both deformation increments and load increments and is therefore a suitable method.

In the NR iteration method the stiffness relation is evaluated every iteration. This means that the prediction is based on the last known or predicted situation. After each iteration, the solution is checked whether the solution was sufficient or whether a new iteration must be executed. The Newton-Raphson method yields a quadratic convergence characteristic. This means that the NR method converges to the final solution within a few iterations, but due to the stiffness matrix update every increment this iteration method is relatively time consuming. The system of equations to be solved are:

$$\mathbf{K}(p_{i-1}) \cdot \Delta p_i = q - f(p_{i-1}) \quad (3.3)$$

Where  $\mathbf{K}(p_{i-1})$  is the stiffness matrix in the previous iteration  
 $\Delta p_i$  is the deformation increment due to loading increment  
 $q$  is the total applied load in the nodes  
 $f(p_{i-1})$  is the internal reaction forces in the nodes

All the values for the  $(i - 1)$  - *th* iterations have already been calculated during previous solution step, the only unknown is  $\Delta p_i$ . The iteration procedure continues until the solution satisfies a certain convergence criteria. In ATENA these are:

- displacement error tolerance;
- residual error tolerance;
- absolute residual error tolerance;
- energy error tolerance.

The lower the tolerance the more accurate the solution becomes. The disadvantage is that this requires more computer capacity. The values of the convergence limits are set by default to 0.01. Smaller load increments increases the probability of finding equilibrium within each step.

The concept of the Newton Raphson solution method is depicted in Figure 3.1.

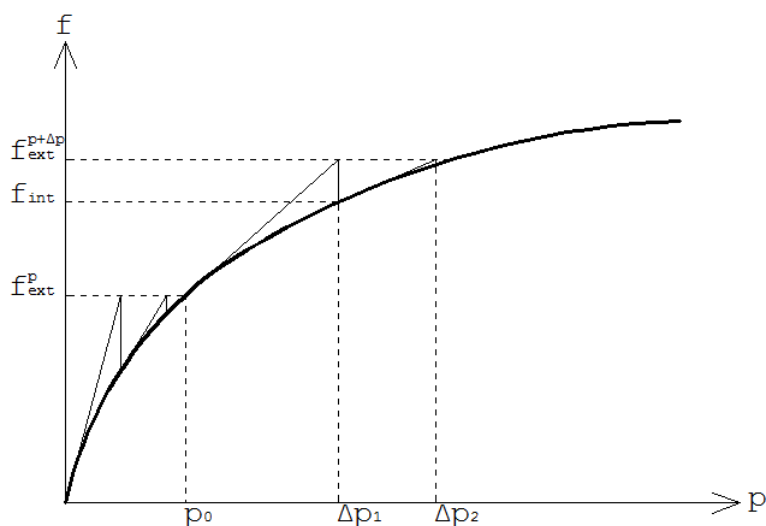


**Figure 3.1: Regular Newton-Raphson iteration**

The stiffness matrix depends on the deformation and is therefore updated for each iteration. However, the recalculation of the stiffness matrix is very time consuming. The Modified Newton Raphson (Mod-NR) method only evaluates the stiffness relation at the beginning of every displacement or load increment, in other words:

$$\mathbf{K}(p_{i-1}) \simeq \mathbf{K}(p_0) \quad (3.4)$$

It produces very significant time saving, but it also exhibits worse convergence of the solution procedure. Usually the Mod-NR method needs more iterations, but every iteration is faster compared to the NR method.

The concept of the Modified Newton Raphson solution method is depicted in Figure 3.2.

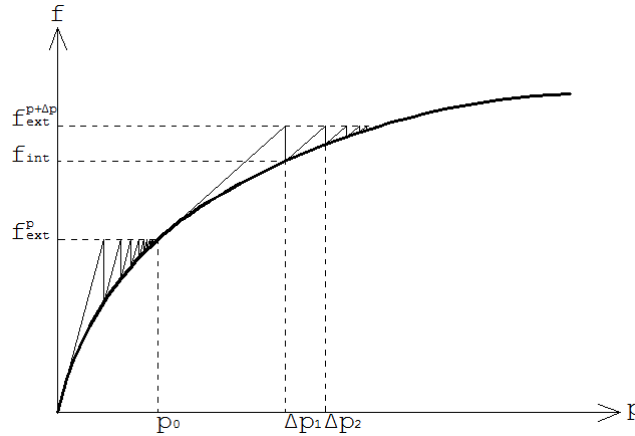


Figure 3.2: Modified Newton-Raphson iteration

### 3.2.2 Arc length iteration

The Arc-length method is together with the Newton-Raphson an often used iteration method. The reason for this is its robustness and computational efficiency which guaranty good results. With ordinary iteration methods the predictions for the displacement increments can become significantly large. This is the case especially if the load-displacement graph is almost horizontal. This may result in large predictions for the displacement with a fixed load increment. The Arc-length a iteration method that can solve this problem. Snap-through and snap-back behaviour are examples where the arc-length method is highly recommended.

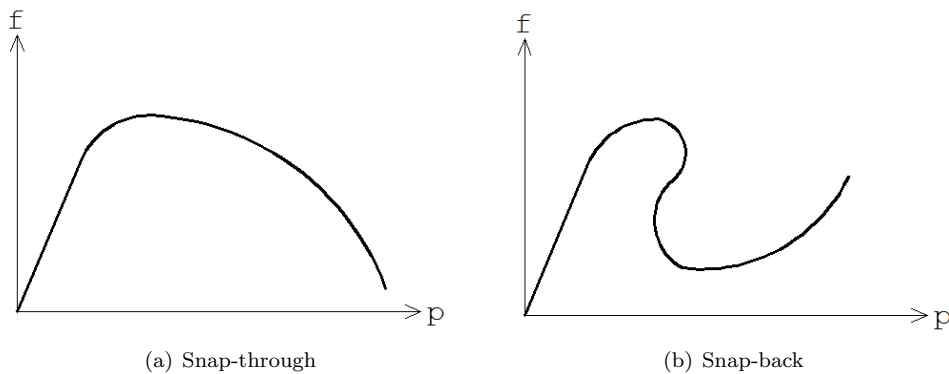


Figure 3.3: Phenomena in which arc-length control is recommendable

The primary task of this method is to observe complete load-displacement relationship rather than applying a constant loading increment as it is in the NR method. At the end of each step both loading and displacement conditions become fixed. The fixation is performed by establishing the length of the loading vector.

In the NR formulation the degrees of freedom were associated with the displacements, but for this method a fictitious degree of freedom for the loading must be introduced, the load multiplier  $\lambda$ .

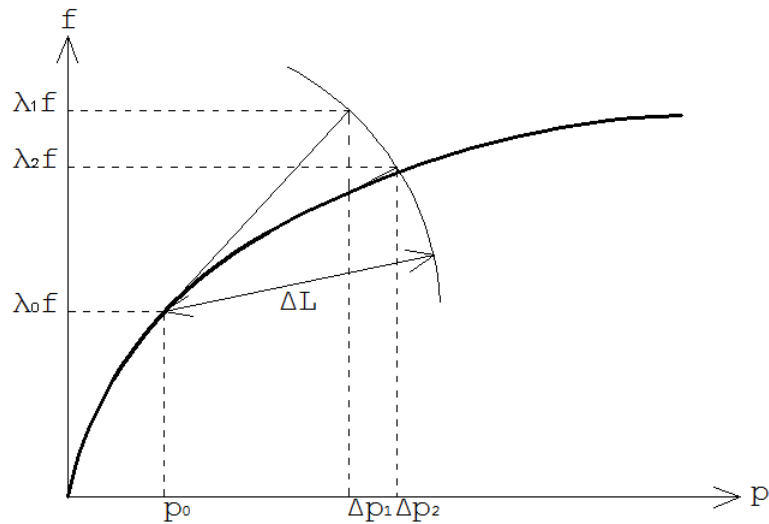


Figure 3.4: Arc-length control

### 3.2.3 The line search method

ATENA makes use of the line search method to optimise the iteration technique. This method only helps to stabilize and to speed up the convergence process. The method introduces a new parameter  $\eta$  which becomes the iterative step length. The basic idea behind  $\eta$  is to minimize work of current out-of-balance forces on displacement increment. It is recommendable to use the line search method in combination with an iteration solver because it can accelerate or damp the speed of analysis of the load-displacement relationship.





## Chapter 4

# Modelling of reinforced concrete in ATENA

During this thesis, the software program ATENA 3D [15] is used for the finite element modelling. ATENA is developed by Cervenka Consulting specially for concrete structures and therefore highly recommendable for modelling punching shear failure. For a better understanding of finite element analyses the implemented theories and modelling considerations are presented.

### 4.1 Material modelling

Realistic non-linear analyses require adequate definitions of material models. When simulation the structural behaviour by means of a FEM analyses, aspects regarding the input parameters are of a big importance. It is important to make a distinction between the different goals of analyses before determining the input parameters. If the aim is to simulate the actual response of a conducted experiment, material parameters as close as possible to the real specimen properties are desirable. On the other hand, if the purpose is to simulate the response of a non-conducted experimental test it is applicable to assign mean values to the material models. If the aim of the analysis is to obtain a proper design, a safety format must be adopted. In this case the characteristic values should be divided with a partial safety factor. The obtained ultimate load from the analysis corresponds to the design resistance.

Constitutive models serve as rational tools to describe the material behaviour and therefore are of big importance for the numerical analysis. ATENA uses advanced constitutive models that enables a simulation of the real structure in service as well as in ultimate loading conditions. The redistribution of internal forces due to the non-linear material behaviour is taken into account and the resulting deformation and stress state satisfies all requirements of mechanics:

1. equilibrium of forces;
2. compatibility of deformations;
3. material laws.

The FEM analysis forms the fundamental theory for this thesis. A good understanding of the different material models and their theories is of big importance. The next sections are

written with the help of the ATENA Theory Manual [51]. It is recommendable to see this manual for further background information.

#### 4.1.1 Concrete model

The structural response of concrete with non-linear material behaviour can be distinguished in two stages. Concrete is assumed to be isotropic and homogeneous up to crack initiation. Up to this phase the concrete is modelled with a linear-elastic relation. At the time the crack initiation starts, several advanced constitutive relations that are capable of describing the non-linear behaviour in three dimensions need to be employed in the material model.

During this thesis the fracture-plastic model *CC3DNonLinCementitious2* for the non-linear analyses is used. This model is capable of describing concrete cracking, crushing and plastic behaviour. The basic material properties used for model are shown in Figure 4.1. Each part of the stress-strain diagram is intended to describe the actual behaviour of concrete in different phases. The fracture-plastic model is a combination of different models for each part of the curve.

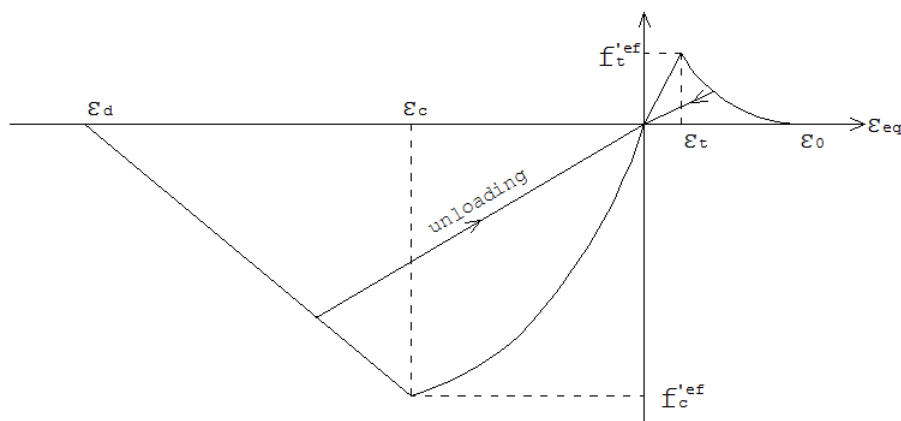


Figure 4.1: Uniaxial stress-strain law for concrete

The fracture-plastic model combines constitutive models for tensile and compressive behaviour. This model is based on the smeared crack formulation and crack band model. The model includes the Rankine failure criterion, exponential softening and it can be used as rotated or fixed crack model. The Menétrey-Willam [44] failure surface provides the basis for the hardening/softening plasticity model.

The fracture-plastic model makes use of the method of strain decomposition as it was introduced by de Borst [21] to combine fracture and plasticity models together into a single model such that plasticity is used for concrete crushing and the Rankine fracture model for cracking:

$$\epsilon = \epsilon^e + \epsilon^p + \epsilon^f \quad (4.1)$$

Where  $\varepsilon^e$  is the elastic strain component  
 $\varepsilon^p$  is the plastic strain component  
 $\varepsilon^f$  is the fracture strain component

The increments of the plastic and fracture strain must be evaluated based on the used material models. These models are briefly discussed during the next sections.

### Rankine fracturing model for concrete cracking

The Rankine-fracturing model is used for concrete cracking. The fracture model is based on the classical orthotropic smeared crack formulation and crack band model. Compared to the discrete cracking model, the smeared crack model approach is more advantageous, giving satisfying accuracies of global results. The feature of the smeared cracking approach is that the cracks are smeared over an entire element. This means that the model disables the cracks to fully open and thus the transfer of tensile stresses through the crack is somewhat overestimated compared to reality. Within the smeared crack concept two options are available for crack models: the fixed crack model and the rotated crack model. In both models the crack is formed when the principal stress exceeds the tensile strength. It is assumed that the cracks are uniformly distributed within the material volume.

In the fixed crack model the crack direction is given by the principal stress direction at the moment of the crack initiation. During further loading this direction is fixed and represents the material axis of the orthotropy. In the rotated crack model, the direction of the principal stress coincides with the direction of the principal strain. This means that no shear strain occurs on the crack plane and only two normal stress components must be defined.

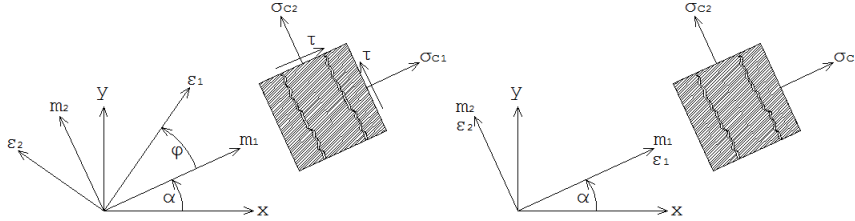


Figure 4.2: Fixed and rotated crack model

Note that the following expressions are given in tensor notation. The intention here is only to illustrate the fundamental theory the material model uses.

The criterion used for the Rankine fracturing model:

$$F_i^f = \sigma_{ii}'^t - f_{ti}' \leq 0 \quad (4.2)$$

Which simply means that as long as the stress is less than the strength of concrete, the concrete is uncracked. The stress is calculated by the so-called *elastic predictor*:

$$\sigma_{ij}'^t = \sigma_{ij}'^{n-1} + E_{ijkl}' \cdot \Delta \varepsilon_{kl}' \quad (4.3)$$

If the Rankine failure criterion is not met, the increase in fracture strain is calculated by assuming that the final stress state must satisfy:

$$F_i^f = \sigma_{ii}'^t - f_{ti}' = \sigma_{ii}'^t - E_{iikl} \cdot \Delta \varepsilon_{kl}'^f - f_{ti}' = 0 \quad (4.4)$$

After substitution (4.4) into (4.3) a formula for the increment of the fracturing multiplier  $\Delta\lambda$  is recovered:

$$\Delta\lambda = \frac{\sigma_{kk}'^t - f_t'(w_k^{max})}{E_{kkkk}} \quad (4.5)$$

This equation must be calculated with iterations since the tensile strength is controlled by the crack opening.

The fictitious crack model developed by Hillerborg et al. [3] is considered, in which the tensile strength is controlled by the crack opening. The crack width is calculated by:

$$w_k^{max} = L_t(\bar{\varepsilon}_{kk}'^f + \Delta\lambda) \quad (4.6)$$

Where  $L_t$  is the characteristic length  
 $\bar{\varepsilon}_{kk}'^f$  is the the total value of fracturing strain in k-direction

The softening behaviour of concrete in tension is the one derived experimentally by Hordijk [27], where the crack width is related to the stress:

$$w_c = 5.14 \frac{G_f}{f_t'^{ef}} \quad (4.7)$$

Where  $w_c$  is the crack opening at the complete release of stress  
 $G_f$  is the fracture energy needed to create a unit area of stress-free crack  
 $f_t'^{ef}$  is the effective tensile strength

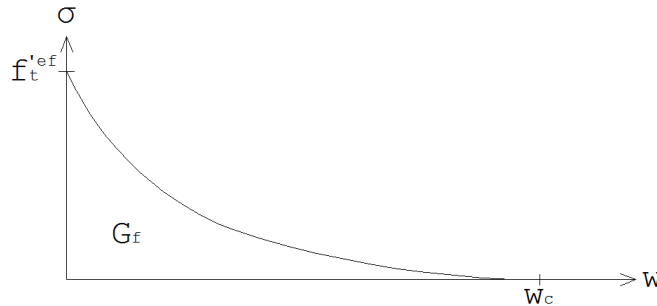


**Figure 4.3: Stress-crack opening law according to Hordijk [27]**

In heavily reinforced concrete structures, the cracks cannot fully develop and concrete contributes to the steel stiffness. This effect is called tension stiffening and in the used material model it can be simulated by specifying a tension stiffening factor  $c_{ts}$ . This factor represents the relative limiting value of tensile strength in the tension-softening diagram. The effect of

tension stiffening has not been included in the present study.

The shear strength of cracked concrete is calculated using the Modified Compression Field Theory of Vecchio and Collins [23]. This theory states that the compressive strength should decrease when the transverse tensile strain increases. Cracked concrete is less strong and softer compared to the concrete specimens used for testing. The  $r_{c,lim}$  parameter is related to the transverse tensile strain, and the decrease of the compressive strength depends on the stage the concrete is cracked. The default value in ATENA allows a maximum decrease of 80%.

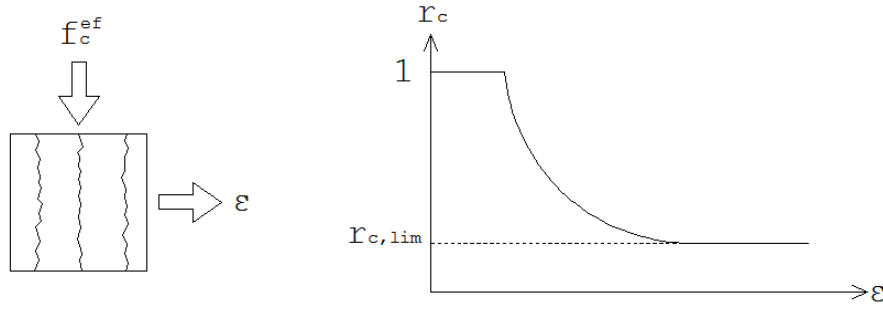


**Figure 4.4: Reduction of compressive strength due to the development of lateral tensile strains**

$$f_c^{ef} = r_{c,lim} \cdot f_c \quad (4.8)$$

### Plasticity model for concrete crushing

New stress state in the plastic model is computed using the predictor-corrector formula. Note that the following expressions are given in tensor notation. The intention here is only to illustrate the fundamental theory the material model uses.

$${}^{(n)}\sigma_{ij} = {}^{(n-1)}\sigma_{ij} + E_{ijkl} (\Delta\varepsilon_{kl} - \Delta\varepsilon_{kl}^p) = \sigma_{ij}^t - E_{ijkl} \Delta\varepsilon_{kl}^p = \sigma_{ij}^t - \sigma_{ij}^p \quad (4.9)$$

The plastic corrector  $\sigma_{ij}^p$  is computed directly from the yield function by return mapping algorithm.

$$F^P(\sigma_{ij}^t - \sigma_{ij}^p) = F^P(\sigma_{ij}^t - \Delta\lambda l_{ij}) = 0 \quad (4.10)$$

The crucial aspect is the definition of the return direction  $l_{ij}$ , which can be defined as:

$$l_{ij} = E_{ijkl} \frac{\partial G^P(\sigma_{kl}^t)}{\partial \sigma_{kl}} \quad \text{then} \quad \Delta\varepsilon_{ij}^p = \Delta\lambda \frac{\partial G^P(\sigma_{ij}^t)}{\partial \sigma_{ij}} \quad (4.11)$$

Where  $G^P(\sigma_{kl}^t)$  is the plastic potential function, whose derivative is evaluated at the predictor stress state  $\sigma_{ij}^t$  to determine the return direction.

The plasticity model for concrete in compression is based on the Men etreyWillam [44] failure surface. The position of the failure surface is not fixed but it can expand and move along the hydrostatic axis, simulating the hardening and softening stages. This model differs from the other published formulations in its ability to handle physical changes like crack closure and it is not restricted to any particular shape of hardening-softening laws. The model can be used to simulate concrete cracking, crushing under high confinement and closure due to crushing in other material directions.

The hardening/softening law is based on uniaxial compressive tests. The law is shown in Figure 4.5.

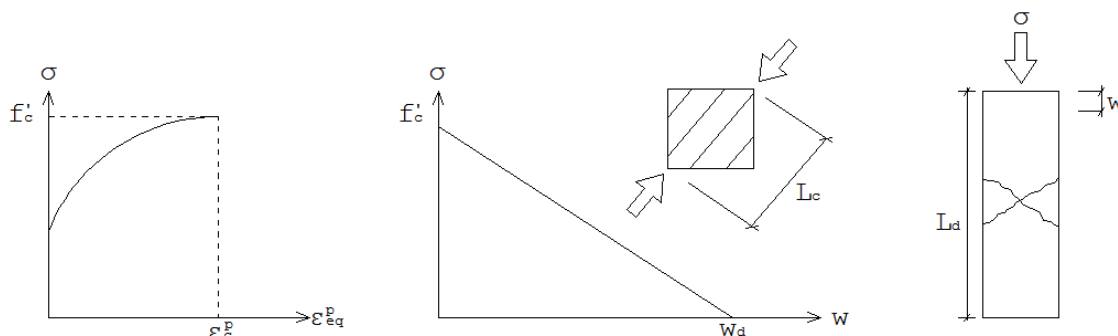


**Figure 4.5: Compressive hardening/softening based on experimental observations by van Mier [38]**

$$w_d = \varepsilon_{eq}^p \cdot L_c \quad (4.12)$$

Where  $w_d$  is the plastic displacement  
 $L_c$  is the length scale parameter  
 $\varepsilon_{eq}^p$  is the value of equivalent plastic strain

The elliptical hardening curve and the linear softening curve are based on the work of van Mier [38]. The softening is described as a linear decrease of the compression strength. In this way, the energy needed for generation a unit area of the failure plane is indirectly defined. From the experiments of van Mier, the value of  $w_d$  is determined to be 0.5 mm for normal concrete. This value is used as default for the definition of the softening in compression. The elliptical part is given by the following expression:

$$\sigma = f_{co} + (f_c - f_{co}) \sqrt{1 - \left( \frac{\varepsilon_c - \varepsilon_{eq}^p}{\varepsilon_c} \right)^2} \quad (4.13)$$

The coefficient for plastic flow direction enables simulation of volume change when the concrete is subjected to compression. The default value in ATENA for this factor is 0, which means no change in volume. Positive values indicates concrete expansion, whilst negative values results in concrete compacting. A volume decrease is only reasonable during high triaxial state of stresses. During the analyses conducted in this study the parameter has

been set to the default value of 0.

Aggregate interlock is the projection of aggregate particles from one side of a crack in concrete into recesses in the other side so as to effect load transfer in compression and shear. This phenomenon is investigated in 1980 by J. Walraven [52] and illustrated in Figure 4.6.

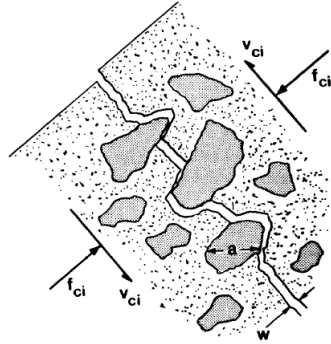


Figure 4.6: Transmitting shear stresses across the crack by aggregate interlock

#### 4.1.2 Reinforcement model

The reinforcement can be included in two ways, either as smeared or as discrete bar elements. In this study the reinforcement bars are modelled as discrete bars.

The used stress-strain law is bi-linear with hardening. The parameters are the elastic modulus of the steel  $E_s$ , the yield stress  $\sigma_s$ , the ultimate stress  $\sigma_t$  and the ultimate strain  $\epsilon_{lim}$ .

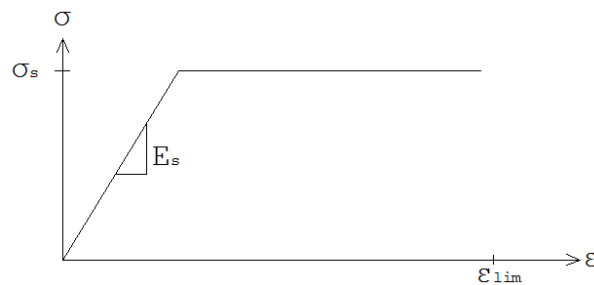


Figure 4.7: The bilinear stress-strain law for reinforcement

## 4.2 Structural definition

Most of the geometrical properties are defined as macro-elements which can be modelled in every required shape. Other types of elements are reinforcement bars, external cables and different types of springs.

Element types are assigned to each macro-element. Commonly three dimensional solid elements are used for macro-elements representing concrete material. In addition to solid

elements, there is also the option to use shell elements. Shell elements are thinner forms of solid elements and are used in cases where bending is of interest. The difference is that the strain distribution perpendicular to the element surface is linear and that cross-sections remain plain after deformation. Shell elements are more computationally effective compared to the solid elements.

The reinforcement is modelled as one dimensional line elements with an assigned bar diameter. These elements are embedded into the concrete elements. Apart from modelling separate one dimensional line elements, a smeared approach is also an option. With this option the reinforcement is spread along the macro-elements by assigning a reinforcement ratio. The contact area between the reinforcement bars and the surrounding concrete can be assigned either a perfect bond or a bond-slip relation. The parametric study from Öman and Blomkvist [19] conducted in 2006 showed that the bond features was less significant in their study to punching shear behaviour. That is why in this thesis perfect bond is assigned.

Important input parameters are the boundary conditions. Boundary conditions can be assigned to nodes, lines or surfaces. The choice between depends on which most resembles the actual support. The boundary conditions specifies the allowing or preventing displacement in three coordinates. These conditions are often used to simplify symmetrical structures.

An assembly of macro-elements can be used in case of irregular structures. Special attention is required for the contact surfaces between adjacent macro-elements. The properties of this contact prescribe the structural behaviour between the surfaces. Three different types of connections can be assigned to a contact surface, a rigid connection, an interface connection and no connection. The interface connection is prescribed by so-called GAP-elements. These elements describes the physical properties of contacts between two surfaces. This material model is used to simulate the contact properties between the concrete foundation pile and the surrounding concrete floor.

### 4.2.1 GAP-elements

The interface material is based on the *Mohr-Coulomb criterion* with tension cut off. See section 2.4 for a detailed description of the Mohr-Coulomb criterion.

ATENA uses a constitutive relation for a general three-dimensional case in terms of tractions on interface planes and relative sliding and opening displacements:

$$\begin{Bmatrix} \tau_1 \\ \tau_2 \\ \sigma \end{Bmatrix} = \begin{bmatrix} K_{tt} & 0 & 0 \\ 0 & K_{tt} & 0 \\ 0 & 0 & K_{nn} \end{bmatrix} \begin{Bmatrix} \Delta v_1 \\ \Delta v_2 \\ \Delta u \end{Bmatrix} \quad (4.14)$$

The initial failure surface corresponds to Mohr-Coulomb equation 2.14, with ellipsoid in tension regime. After stresses violate this condition, this surface collapses to a residual surface which corresponds to dry friction, see Figure 4.8.

The  $K_{nn}$  and  $K_{tt}$  denote the initial elastic normal and shear stiffness respectively. Typically for zero thickness interfaces, the value of these stiffnesses correspond to a high penalty number. It is recommended to estimate the stiffness value using the next expressions:



$$K_{nn} = 100 \frac{E}{t} \quad (4.15a)$$

$$K_{tt} = 100 \frac{G}{t} \quad (4.15b)$$

Where  $E$  and  $G$  are respectively the minimal elastic modulus and the shear modulus of the surrounding material. The  $t$  represents the width of the interface zone. It is suitable due to numerical reasons if stiffness is about 10 times the stiffness of adjacent finite elements.

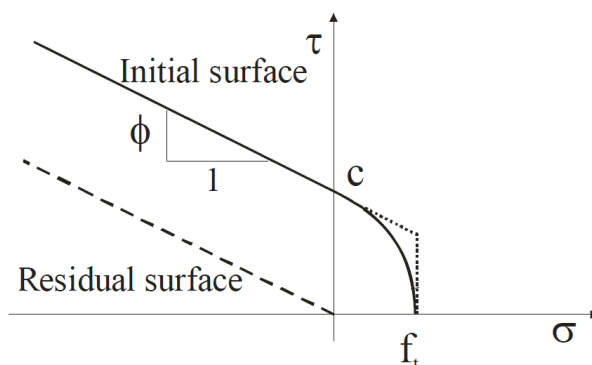


Figure 4.8: Failure surface for interface elements

### 4.3 Solution control setting

During FEM analysis, an iteration solver tries to find numerical equilibrium between external and internal forces. The solver attempts to reach equilibrium until the convergence criteria are satisfied, this means that the solver stops with performing iterations when the internal force reaches a value close enough to the external force. This option is designed to stop the analysis when the convergence errors at the end of a load step or iteration are so large, that continuing the analysis does not make sense with respect to results quality. The value of the allowable tolerance determines the accuracy of the equilibrium condition. A large tolerance will give a fast iteration procedure but will result in less accurate results, while a very low tolerance will increase the change of convergence instability. In ATENA the default values for tolerances for the different convergence criteria are presented in Table 4.1. The default values were used in the analyses within this thesis.

<i>Convergence criteria</i>	<i>Tolerance</i>
Displacement error tolerance	1.00%
Residual error tolerance	1.00%
Absolute residual error tolerance	1.00%
Energy error tolerance	0.01%

Table 4.1: Default values of error tolerances

Reducing the size of a load step increases the probability of reaching convergence. Problems with iteration might be the results of insufficient number of iterations, conservative error

tolerances or an inappropriate solution method.

It is important to review the iteration procedure after its completion to ensure that errors do not cause corrupt outcomes. It is inappropriate to trust on analysis output that have encountered high error values.

## Chapter 5

# Validation of modelling technique

The presence of internal or external ribs on a foundation pile is of big importance for the shear transfer capacity between the pile and the surrounding slab. This is emphasised by experimental shear tests conducted by J. Aziz [6]. The experimental results show a significantly increase of shear transfer capacity for toothed surfaces compared to smooth surfaces. The same counts for the ribs on a foundation pile which ensure a great material interlock.

The definition of a model is that it is a simplified representation of a real object. Also ATENA makes use of simplifications to simulate and predict the actual structural behaviour. The problem that directly occurs is the way of modelling the specific contact surface between pile and slab without losing the real behaviour. The goal of this validation study is to justify a proper modelling technique that simulates a failure mechanism which is related to punching shear.

One possibility to simulate the contact surface is to model the exact rib geometry. An appropriate interface material between the modelled ribs and slab should satisfy the concrete to concrete shear behaviour. The advantage of this modelling technique is the ability to observe the development of peak stresses close to a rib during the analysis. These peak stresses might introduce crack initiation which results in an undesirable failure mode. The disadvantage of this modelling technique is the difficulty of generating an appropriate element-mesh which fits both ribs and slab. The rib dimensions are significantly smaller with respect to the total structure. The difference in element mesh around the ribbed pile might introduce numerical errors at node connections.

For this study frictional based interface elements, the so called GAP-elements, are modelled to simulate the contact surface of the ribbed pile and slab. The interface material is based on the MohrCoulomb failure criterion as described in section 2.4. The ribbed pile is modelled as a rectangular pile with planed sides. Each contact surface between the pile and slab is related to its own interface material which describes the physical properties of the contact area. By changing the frictional parameters, different shear properties can be simulated, like smooth, rough and toothed surfaces. The upper limit value describes a perfectly bonded connection, simulated with infinity friction parameters. The lower limit value described a sliding surface with no connection at all, which is related to friction parameters equal to zero. The actual behaviour is somewhere in between these two limit values. By calibrating the

frictional parameters the structural behaviour can be simulated for different surface classes.

In order to validate the modelling technique with interface elements, reliable numerical simulations have been conducted and compared to experimental results. Experiments conducted by C.R. Braam, A. Bosman and A. van Rhijn [16], described in section 2.1.5, have been simulated using FEM analyses. This experiment is also published by the Dutch concrete journal *Cement* during an edition about underwater concrete [45]. The goal of this experiment was to check the safety of the current verification code CUR 77 [14] for ribbed foundation piles. All experimental specimens showed a failure mechanism which relates to punching shear. It is this occurred failure mechanism in combination with the presence of rib geometry which makes this experiment highly usable for the modelling validation.

## 5.1 Laboratory tests for comparison

### 5.1.1 Geometrical data and loading

It is important to keep in mind that reported quantities are not always correct due to human errors and shortcomings of equipment. The tested specimens are square shaped slabs with a length of 3750 mm and a height of 500 mm. A footing of 425 mm is present at full slab circumference to guarantee some free space underneath the center of the slab. Each specimen is supported by a steel frame with four rectangular contact surfaces, see Figure 5.1(c).

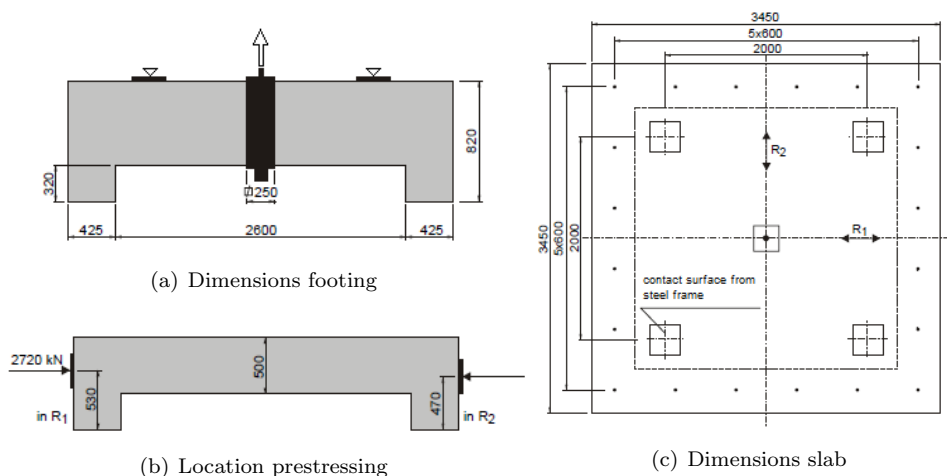


Figure 5.1: Experimental setup pull-out tests Braam et al. [16]

The concrete pile of 250x250 mm was loaded in upward direction by making use of a tensile rod applied at the center of the pile. The tensile rod was connected to a hydraulic jack. The pile was exposed to a displacement controlled load with an incremental velocity of 1.0 mm/min. All dimensions of the test specimens are shown in Figure 5.1.

Prestressing cables are applied to simulate the bracing effect of sheet walls. The total prestressing force  $F_p$  was 2720 kN per direction, divided over six cables. This prestressing force is equivalent to a compression stress  $\sigma_c$  of 1.36 N/mm<sup>2</sup>. The cables are placed at different heights to prevent an intersection, see Figure 5.1(b) for the exact location per direction.

The total experiment includes six specimen investigations with three different rib geometries. The next series are distinguished:

- series 1, minimum external;
- series 2, minimum internal;
- series 3, maximum internal.

The advantage for external ribs is that the indentations don't affect the net pile cross-section. This is explained with Figure 5.2(b), the original cross-section of 250 mm is at some locations reduced to 200 mm due to the internal indentations. This area reduction causes increased stress values. The disadvantage of external indentations is the inconveniences in prefabrication, continuously adjusting the steel mould to a specific rib geometry or rib distance is a cumbersome process. The rib geometry for internal indentations is easily adjustable in a steel mould by placing small steel triangles at each desirable side. The dimensional properties per series are shown in Figure 5.2. For each series two specimens are tested.

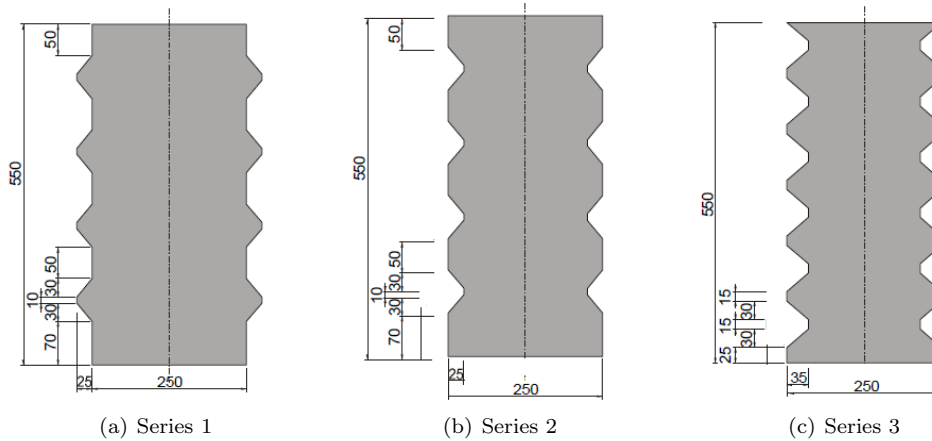


**Figure 5.2:** The different rib geometries of all series

### 5.1.2 Material data

The strength properties of each specimen were determined by making use of tensile splitting tests of concrete cubes. The cubes were poured with the same concrete mixture as the corresponding specimen slab. The mean splitting strength is often not used as a concrete parameter during calculations, that is why the mean tensile strength is derived by making use the next equation (according to CUR 52 [12]):

$$f_{ctm} = 0.9 \cdot f_{ct,spm} \quad (5.1)$$

Where  $f_{ct,spm}$  = mean splitting strength of concrete [N/mm<sup>2</sup>]  
 $f_{ctm}$  = mean tensile strength of concrete [N/mm<sup>2</sup>]

The short term mean tensile strength of each specimen is determined by making use of the concrete maturity concept. To make sure the strength properties of the specimen and cubes

are equivalent, temperature sensors were placed in both members. The temperature sensors were connected to a maturity computer. The maturity computer monitors the strength development based on the increase of temperature. The specimen strength is directly derived from the cubic splitting tests.

Table 5.1 shows the mean tensile strength of the concrete cubes with the related maturity. The tensile strength of each specimen is based on the reached maturity.

<i>Specimen</i>	<i>Maturity cube</i> [°Ch]	<i>f<sub>ctm</sub> cube</i> [N/mm <sup>2</sup> ]	<i>Maturity specimen</i> [°Ch]	<i>f<sub>ctm</sub> specimen</i> [N/mm <sup>2</sup> ]
1-1	5250	2.84	5696	2.90
1-2	4330	2.30	4261	2.30
2-1	5629	2.86	4545	2.50
2-2	4505	2.56	4033	2.40
3-1	4008	2.36	3753	2.30
3-2	3678	2.15	3539	2.15

**Table 5.1: Concrete maturity data and centric tensile strengths**

The used cables are Dywidag prestressing cables [30] with strength properties as shown in Table 5.2.

<i>Diameter</i> [mm]	<i>Steel grade</i> [N/mm <sup>2</sup> ]	<i>Area</i> [mm <sup>2</sup> ]	<i>Elastic modulus</i> [N/mm <sup>2</sup> ]	<i>Density</i> [N/mm <sup>3</sup> ]
32	950	804	205000	$78.50 \cdot 10^{-6}$

**Table 5.2: Dywidag prestressing cable properties**

All concrete piles are prefabricated with a concrete class corresponding to B55.

### 5.1.3 Results and observations from experiments

Table 5.3 contains all experimental results like failure loads, crack angles and cone diameters. Slope angles  $\alpha_1$  and  $\alpha_2$  are respectively in  $R_1$  and  $R_2$  direction. The  $R_1$  direction is the direction with the ribbed sides and the  $R_2$  direction is the direction with the plane sides of the pile. See Figure 5.3 for a schematic presentation of the crack angles and cone diameters.

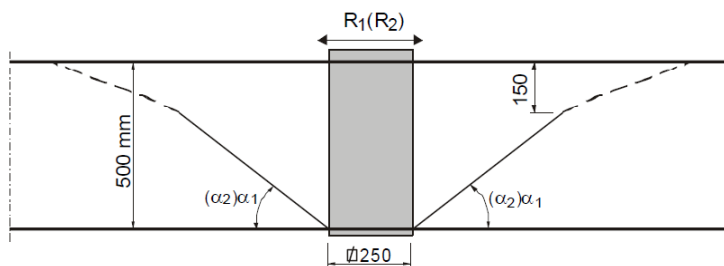


**Figure 5.3: Presentation of pull-out cone for directions  $R_1$  and  $R_2$**

<i>Specimen</i>	<i>Failure load</i> [kN]	<i>Diam. in R<sub>1</sub></i> [m]	<i>Diam. in R<sub>2</sub></i> [m]	<i>Slope α<sub>1</sub></i>	<i>Slope α<sub>2</sub></i>
1-1	2483	1.70	1.50	26°	30°
1-2	2373	1.20	1.20	29°	32°
2-1	2399	1.60	1.45	29°	32°
2-2	2329	1.65	1.35	27°	33°
3-1	2421	1.75	1.35	26°	33°
3-2	2179	1.55	1.25	29°	36°

**Table 5.3: Experimental results conducted by Braam et al [16]**

First of all it is noticeable that all specimen failures are caused by punching shear. The difference between internal and external ribs doesn't seem to influence the punching load capacity of the slab significantly. The difference in failure load is with 2% relatively small, see Table 5.3. The mean tensile strength is directly related to the failure load. Specimen 3-2 with a relative low tensile strength of 2.15 N/mm<sup>2</sup> shows the lowest failure load of 2179 kN and vice versa for specimen 1-1 with a relative high tensile strength of 2.9 N/mm<sup>2</sup> with a corresponding failure load of 2483 kN.

The results show also that the influence of internal ribs and external ribs seems to make no difference on the crack angles  $\alpha_1$  and  $\alpha_2$ . All diameters and slope angles are in the same order of magnitude without extremes. However, the magnitude of  $\alpha_1$ , orientated along the ribbed sides, is in almost all the experiments lower compared to the magnitude of  $\alpha_2$ . This tends to the conclusion that the ribbed sides do have a larger cone radius compared to the plane sides. It is noticeable that also the plane sides benefit from the ribbed sides, despite the fact the crack angle is steeper, the plane sides account for a large extend in the failure strength.

## 5.2 Finite element modelling of laboratory tests

### 5.2.1 Boundary conditions and loading

In order to reduce the required computer capacity only a quarter specimen has been modelled. In the symmetries, boundary conditions were introduced such that free movement was prevented in the direction with geometrical continuity. In order to represent the stiff support surfaces, steel plates are modelled at the bottom of the pile and at the slab surface.

The modelling principles are described by Figure 5.4. The constraints in z-axis are modelled to simulate the steel support structure and the constraints in x-axis and y-axis to simulate slab continuity. The dimensions correspond to a quarter of the original specimen shown in Figure 5.1.

The modelled prestressing force of 453 kN per cable is equivalent to the prestressing force applied before testing. The amount of prestressing force during the experiment was not measured. Potential losses due to shrinkage, relaxation or the order of stressing the cables has due to absence of information not been taken into account.

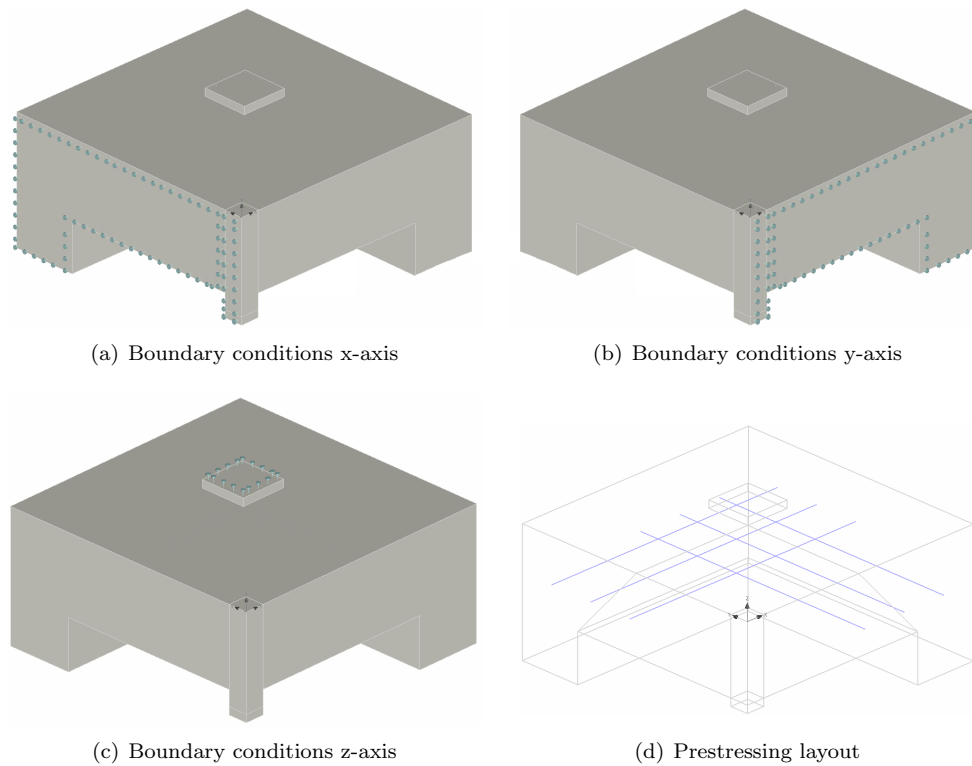


**Figure 5.4: Boundary conditions and prestressing layout**

The modelled specimen is in accordance with the experiment loaded with a prescribed displacement at the bottom of the pile. During each load step the displacement increases with 0.5 mm in upward direction.

### 5.2.2 Material properties

The strength parameters for the concrete slab are based on the mean tensile strength derived experimentally from splitting tests described in section 5.1.2. The mean values instead of characteristic values are chosen to get the material parameters as close as possible to the real specimen properties. The mean values of the modulus of elasticity and the concrete compressive strength in terms of the mean tensile strength, in accordance to EC 2 Table 3.1 [10], are given by:

$$E_{cm} = 22 \left( \frac{f_{cm}}{10} \right)^{0.3} \quad (5.2)$$

$$f_{cm} = f_{ck} + 8 \text{ N/mm}^2 \quad (5.3)$$

Where  $E_{cm}$  = mean modulus of elasticity of concrete [N/mm<sup>2</sup>]  
 $f_{cm}$  = mean compressive strength of concrete [N/mm<sup>2</sup>]  
 $f_{ck}$  = characteristic compressive strength of concrete [N/mm<sup>2</sup>]



The concrete slab material properties are summarised in Table 5.4.

<i>Specimen</i>	$f_{ctm}$ [N/mm <sup>2</sup> ]	$f_{cm}$ [N/mm <sup>2</sup> ]	$E_{cm}$ [N/mm <sup>2</sup> ]	$G_f$ [N/mm]
1-1	2.90	38.05	32850	$30.00 \cdot 10^{-3}$
1-2	2.30	29.22	30350	$28.75 \cdot 10^{-3}$
2-1	2.50	32.06	31204	$29.25 \cdot 10^{-3}$
2-2	2.40	30.63	30800	$28.85 \cdot 10^{-3}$
3-1	2.30	29.22	30350	$28.75 \cdot 10^{-3}$
3-2	2.15	27.19	29700	$28.50 \cdot 10^{-3}$

**Table 5.4: Concrete slab material parameters**

The prefabricated pile is modelled in accordance to EC 2 Table 3.1 [10] mean material parameters to simulate the used concrete class of B55.

$f_{ctm}$ [N/mm <sup>2</sup> ]	$f_{cm}$ [N/mm <sup>2</sup> ]	$E_{cm}$ [N/mm <sup>2</sup> ]	$G_f$ [N/mm]
4.20	63.00	38000	$138.60 \cdot 10^{-3}$

**Table 5.5: Concrete pile material parameters**

The prestressing cables are modelled with bilinear stress-strain material behaviour. The used parameters are in accordance with the actual used Dywidag [30] prestressing cables shown in Table 5.6. The manufacturer includes a 5% deviation in elastic modulus, this has been taken into account to make a safe approximation.

<i>Diameter</i> [mm]	<i>Steel grade</i> [N/mm <sup>2</sup> ]	<i>Area</i> [mm <sup>2</sup> ]	<i>Elastic modulus</i> [N/mm <sup>2</sup> ]	<i>Density</i> [N/mm <sup>3</sup> ]
32	950	804	194800	$78.50 \cdot 10^{-6}$

**Table 5.6: Dywidag prestressing cable properties**

### 5.2.3 Interface material

Interface material is introduced to simulate the frictional properties of the smooth and ribbed side of the pile. The friction properties are based on the Mohr-Coulomb shear failure criteria as described in section 2.4. Two different surface classes are modelled to make a distinction between the ribbed and plane side of the pile. Both frictional properties according to EC 2 section 6.2.5 [10] are used to make an approximation for common used interface parameters.

Different interfaces are modelled to investigate the influence of friction parameters with respect to the structural behaviour. The two material models are named *Interface 1* and *Interface 2* and the characteristics are shown in Table 5.7.

<i>Surface class</i>	Interface 1		Interface 2	
	<i>Cohesion, c</i> [N/mm <sup>2</sup> ]	<i>Friction, <math>\mu</math></i> [-]	<i>Cohesion, c</i> [N/mm <sup>2</sup> ]	<i>Friction, <math>\mu</math></i> [-]
Smooth	0.27	0.60	0.20	0.50
Indented	0.66	0.90	0.50	0.80

Table 5.7: Implemented friction coefficients

### 5.2.4 Finite elements

The concrete slab is modelled with three dimensional solid linear tetrahedral elements. The concrete pile and the steel plates are modelled with three dimensional solid linear brick elements. A linear tetrahedral element contains 4 nodes compared to the 10 nodes of a quadratic element. This means that for quadratic tetrahedral elements the total number of integration points triples instead of a linear element. Although this increase of integration points lead to more accurate FEM results [31], it requires also directly three times more computer capacity. This amount of computer capacity was not available and therefore linear elements are used.

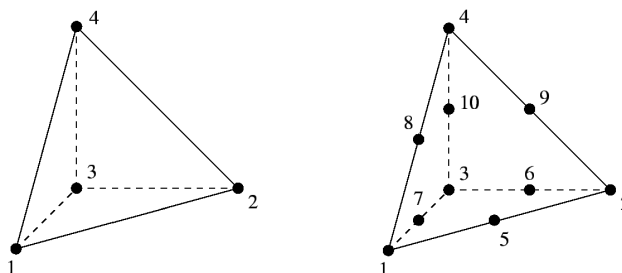


Figure 5.5: Linear and quadratic tetrahedral element

The mesh density specially around the pile is increased to improve the accuracy of the analysis in this important region of the slab. To reduce the total analysis capacity the other regions of the slab are modelled with a relative coarse mesh, see Figure 5.6.

Monitoring points are introduced to compare the structural behaviour based on load-displacement graphs. The location of the monitoring points shown in Figure 5.6(b) are in accordance with the locations of the vertical displacement sensors of the actual experiment.

<i>Macroelement</i>	<i>Mesh type</i>	<i>Element type</i>	<i>Elements</i>
Slab	3D tetrahedral	linear	9285
Prefabricated pile	3D brick	linear	32
Plate slab surface	3D brick	linear	16
Plate pile base	3D brick	linear	9

Table 5.8: Finite element mesh generation

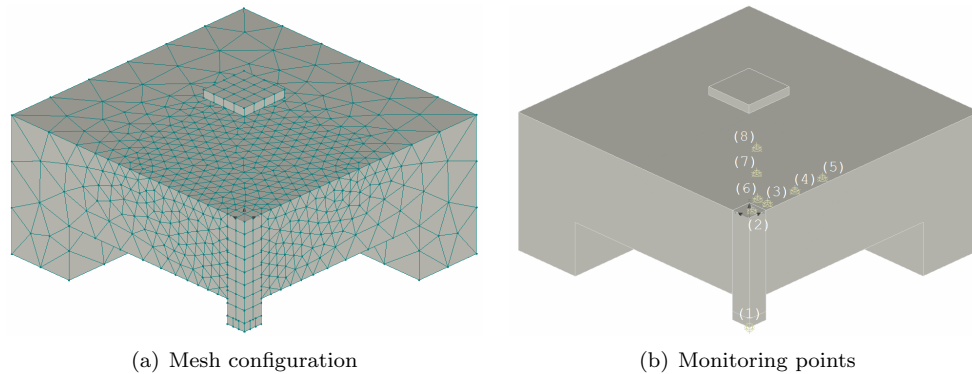


Figure 5.6: Mesh configuration of modelled specimen and monitoring points

### 5.3 Results from numerical analyses

To gain the ability of comparing different numerical results, two specimens are selected for the numerical analysis. A difference in concrete tensile strength and a difference in rib geometry were the most important selection criteria. From these criteria specimens 1-1 and 3-1 are selected for the analysis. For these specimens a load-displacement graph and a crack pattern development are made. The load-displacement graph for both numerical and experimental study are shown in one figure to compare the structural behaviour till slab failure. The crack development shows by means of subsequent load steps the cause of the occurred failure mechanism and the path towards this mechanism.

First of all, it is noticeable that in accordance with the experimental results all FEM analyses showed a punching shear failure mechanism. In first instance, this is an important result in the validity of modelling punching shear with friction interfaces at locations with a concrete to concrete surface.

Table 5.9 contains the results of the four FEM analyses. The slopes  $\alpha_1$  and  $\alpha_2$  are in accordance with Figure 5.3. The slope  $\alpha_1$  corresponds to the ribbed side of the pile and  $\alpha_2$  to the smooth side.

Specimen	<i>Experiment</i>		<i>FE Interface 1</i>		<i>FE Interface 2</i>	
	1-1	3-1	1-1	3-1	1-1	3-1
Failure load [kN]	2483	2421	2216	2186	2176	2010
Slope $\alpha_1$	26°	26°	28°	33°	29°	29°
Slope $\alpha_2$	30°	33°	35°	35°	35°	34°

Table 5.9: Experimental results versus numerical results

The failure load of specimen 1-1 and specimen 3-1 both with Interface 1 differs within a 10% deviation from the experimental results. This difference is partly explained by the natural scatter in results which is typically related to brittle failure. This deviation is also visible with the scatter in the experimental failure loads with theoretically equal concrete strengths, see Table 5.3.

The differences are most likely caused by a combination of multiple material uncertainties, simplifications in implemented material models and element inaccuracy. Parameters such as the concrete compressive strength, modulus of elasticity and fracture energy are estimated based on expressions from the EC 2 [10] and the ATENA Theory Manual [51]. The uncertainty in these important input parameters might lead to less accurate results compared to the actual situation. Different parameter studies are conducted in the past to investigate which conditions influence the punching capacity the most. J. Ozbolt et al. [32] and P. Menétrey [37] concluded that one of the most influential parameter is the amount of fracture energy, an increase leads directly to a significant higher failure load. D. Faria et al. [18] stated that an increase in elastic modulus was not effective for the punching capacity. The opinions about the influence of the compression strength differs within different studies. Menétrey concluded that the tensile strength controls the punching failure instead of the compression strength like Faria states. Since the hypothesis of most analytical models [1, 2, 10] are based on the compressive strength, the study of Faria tends to draw the right conclusion. However, this contradiction is not absolute as the compression strength depends physically on the tensile strength.

The measurement of the crack angle is due to the implemented smeared crack model with a certain inaccuracy. The slopes shown in Table 5.9 are the average values of the contour area plots with relative high values of crack widths. Despite of the inaccurate measuring process, the average values correspond with a scatter to the experimental results. Noticeable is that in all cases the slopes of the FE analysis are larger compared to the actual slopes. The differences are not significantly and are most likely caused by the modelled element size, a mesh with smaller element dimensions could have lead to a more detailed crack inclination.

An important observation is the accordance in a lower magnitude of  $\alpha_1$  compared to  $\alpha_2$  for all analyses. This result validates the conclusion that specific surface conditions of a contact can be modelled with proper friction properties. Which exact friction parameters correspond to a specific contact surface is a point of interest. This calibration is only possible if all the other material parameters are for sure in line with the actual situation. In this simulation the absence of qualitatively input data makes this calibration inaccurate to draw conclusions.

For sure is the fact that the modelled friction parameters from Table 5.7, show good agreement with the experimental results. This implies that the behaviour of a smooth surface can be simulated with a relative low cohesion and friction coefficient compared to an indented surface. This is supported with the presentation of different crack angles in Table 5.9. The importance of proper friction parameters is emphasised with the different results from the analysis with Interface 1 and Interface 2. Interface 2 is modelled with slightly lower friction properties compared to Interface 1. This leads directly to a lower failure load, and quite different crack angles. Although the difference in failure load, the interface properties were not of importance for the occurring failure mechanism.

### 5.3.1 Crack pattern development

The crack development during the numerical analysis corresponds to the development of cracks prescribed by S. Guandalini [25] which is stated to be related to punching shear failure. The FEM results show also strong similarities with the appearing crack pattern observed during the experiment. Figure 5.8 shows the development of cracked elements at different load steps just before failure. It is important to notice that a crack filter is active for crack widths smaller than 0.1 mm. The reason for this filter is to avoid the presentation of micro cracks which make the pictures less clear. The crack filter of 0.1 mm is also convenient to see the similarities in visible cracks at slab surface between the actual and the numerical experiment.

The first radial cracks start to form just after the end of the linear stage of the specimen. During load increments these cracks start to increase in both number and width. Crack widths more than 0.1 mm appear towards the failure load. These radial cracks start at the circumference of the pile and develop in diagonal direction towards the supporting plate, see Figure 5.8(a). This diagonal crack is clearly visible during the experiment shown in Figure 5.7.



**Figure 5.7: Top view of specimen surface during the experiment**

For load steps closer to the failure load, the radial cracks start to increase in number and length. This crack development corresponds to the visible observations during the experiment. During the FEM analysis a radial crack appears perpendicular to the pile face towards the edge of the slab, see Figure 5.8(b). This development is visible as well during the experiment.

At the same time the radial cracks increases in length, the first internal cracks start to develop from the bottom of the pile under a gradient to the slab surface, see Figure 5.8(c). From load step 6 the number of radial cracks stagnated but the crack width increased. The failure load of the specimen corresponds to load step 7. At this load step a clear punching cone starts to appear at areas with a relative high values of principle fracture strain, see Figure 5.8(d). During the actual experiment, suddenly a truncated cone shaped element punches through the slab. During the analysis, the prescribed displacement still increases but the internal reaction force starts to decrease. This caused by the displacement controlled solving method and the decrease in force indicates that the maximum slab capacity has been reached. The load steps after failure show a significantly increase in crack width up to a few

millimetres, this is only numerically possible.

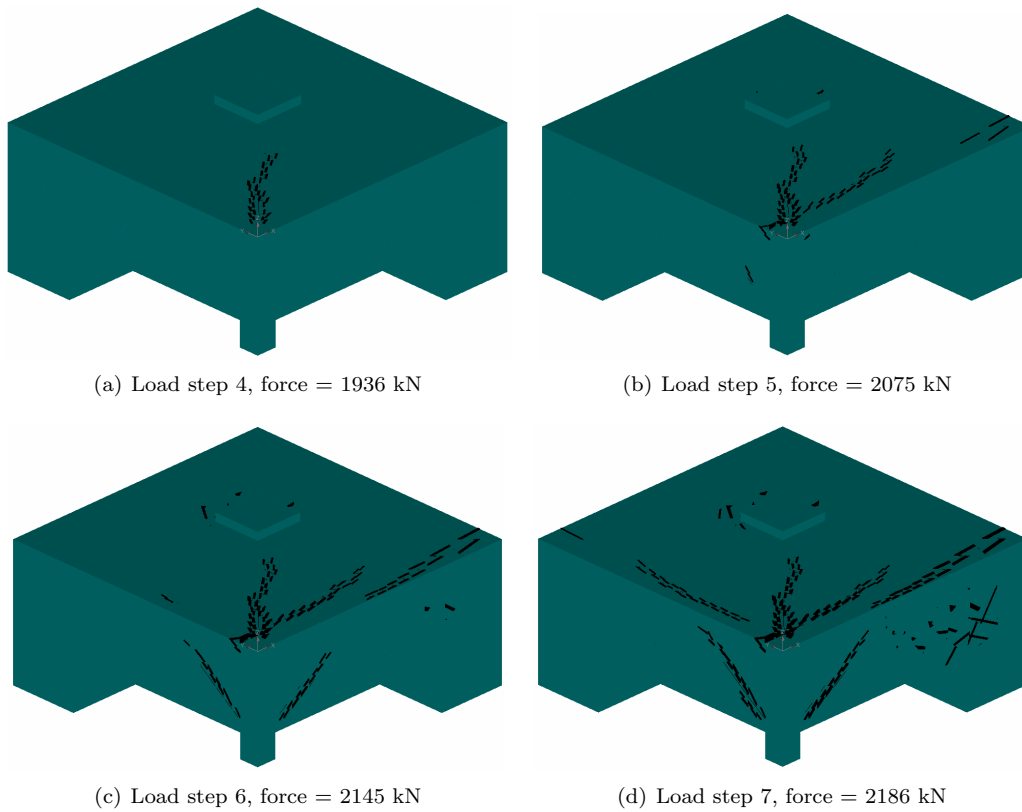
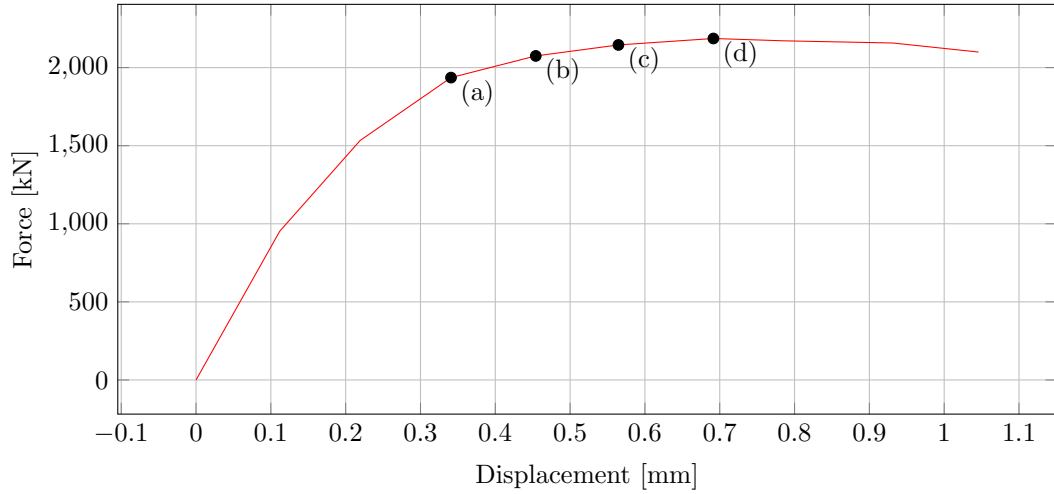


**Figure 5.8: Crack pattern development before failure of specimen 3-1 Interface 1 (crack filter 0.1 mm)**

### 5.3.2 Fracture strain development

To get a better understanding of the appearing crack formation, a principal fracture strain development is shown in Figure 5.9. Although the fracture strain corresponds to specimen 1-1 with interface 1, the crack pattern shows strong similarities with the crack development of specimen 3-1 with interface 1 shown in Figure 5.8.

Figure 5.9 shows contour area plots of slab zones with high values of fracture strain. These regions with high values are related to concrete fracture with visible cracks. During the analysis up to an applied load of 1566 kN only fracture strain appears at slab surface. This is in correspondence with the cracks shown in Figure 5.7. The direction of the strain shows that the cracks are the effect of hogging moment in the direction parallel to the edge. Load step 7 shows slightly the first internal fracture strain which corresponds to low magnitudes of crack widths. This strain development is caused by increasing shear forces. Load step 8 corresponds to an applied load just before slab failure and it's clearly visible that the internal strain developed rapidly. At this load step the slab has almost reached its capacity. Load step 10 corresponds to an applied force right after slab failure and the strain is fully developed over the full height of the slab. The green and red regions of Figure 5.9(d) shows the shape of the punching cone. This fracture strain causes stress free cracks which directly leads to failure.

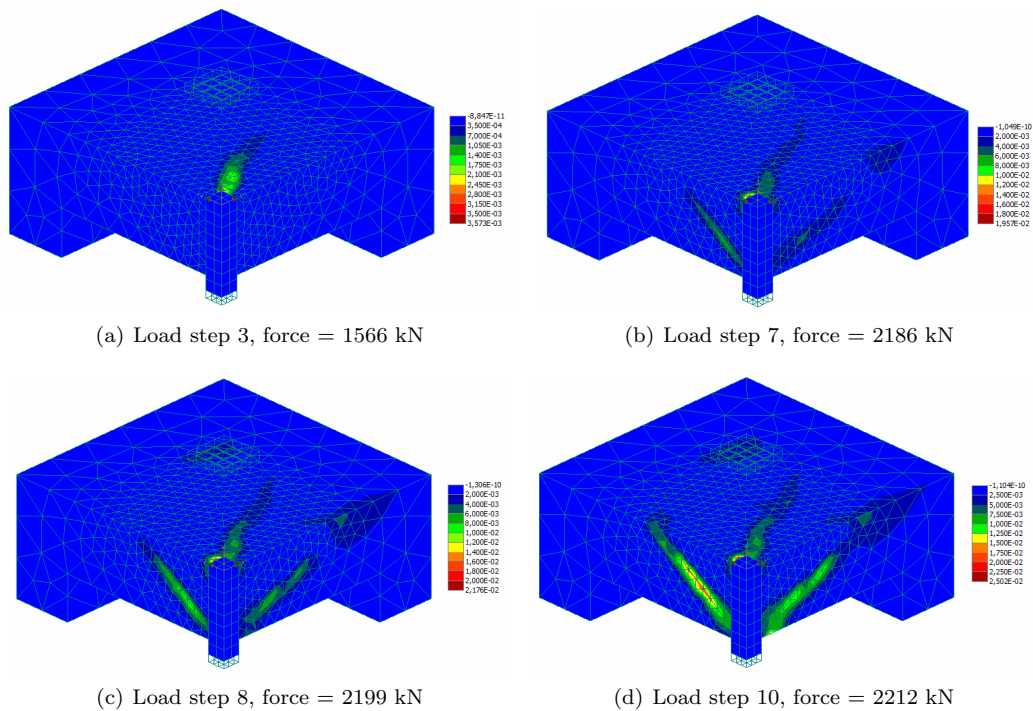


**Figure 5.9:** Development of principle fracture strain [-] of specimen 1-1 with interface 1

### 5.3.3 Load-displacement behaviour

Figure 5.10 illustrates the structural response of the test specimen during loading. The vertical axis presents the force at the bottom of the pile and the horizontal axis presents the vertical displacement of monitoring point 8, see Figure 5.6(b). It is noticeable that both experimental and numerical graphs are cut after a displacement of 0.6 mm. The experiment showed unpredictable displacements at this stage which indicated that the cone punched out of the slab. Due to the brittle failure, the data after specimen failure is not reliable, and therefore not shown. Also the FE analyses has reached its failure force at a displacement of about 0.6 mm.

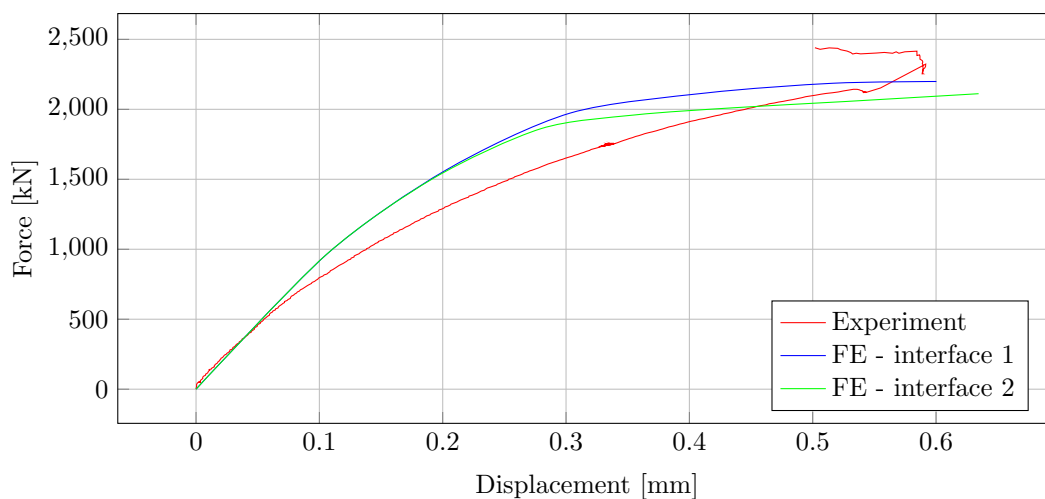


**Figure 5.10: Force-displacement graph of specimen 1-1 corresponding to monitoring point 8**

Both experimental and numerical responses show good agreement for the initial stiffness. However, after the linear stage has been reached the FE analyses show a stiffer behaviour compared to the response that was observed during the experiment. This is believed to be caused by the smeared crack formulation implemented in ATENA, which means that the model responds with significantly decreased stiffness after the crack is fully developed. In reality, cracking affects immediately the response as cracks are initially formed. This numerical modelling problem is corrected by reducing the fracture energy parameter. This parameter describes the amount of fracture energy needed to create a unit area of stress-free crack. By reducing this parameter, the structural response will behave more brittle. As mentioned in section 5.3, this reduction caused a decrease in punching capacity. Although a reduction of the fracture energy, still the FE analyses behave more stiff compared to the experiment. It is believed that this difference could not be the consequence of an overestimated elastic modulus of the concrete slab, since the initial stiffness fits perfectly. If the elastic modulus was overestimated, this should have influenced the linear stage as well. The stiffness decreasing at an earlier stage indicates an earlier crack formation stage. This could indicate an overestimation of the material parameters. This is explained in the scatter in material strengths, while all material input parameters are based on mean values. S. Ericsson [47] faced the same stiffness problem with his numerical study to the punching shear failure by using ATENA. Also M. Staller [50] (FEM program MARC) and L. Trautwein et al. [34] (FEM program DIANA), encounter the same stiffness problem after the linear stage compared to



experimental results.

The absence of information about the prestressing force during the experiment might have resulted in an increased stiffness of the slab. During the FEM analyses no losses caused by friction, shrinkage or relaxation have been taken into account. Also a perfect bond model between reinforcement and concrete has been modelled. The uniform compressive stress resulting from the prestressing cables might hence be overestimated. This causes a delay in the crack formation, which results in a more stiff behaviour.

The difference between the two modelled interface conditions is visible when the analysis starts to reach the its ultimate capacity. The friction properties of interface 2 are slightly lower compared to interface 1. This doesn't result in a significant difference in structural behaviour but more in a failure force reduction. This indicates that a small change in friction parameters is not that important for the overall structural response but more in terms of the ultimate load capacity.

It is important to mention that the deviation in overall structural response between the experiment and the FE analyses is not only caused by improper modelling of the interface material parameters. This deviation is mainly a combination of inaccuracy in material input and numerical errors due to implemented crack models, material models and the precession in element mesh. The experimental results could also be biased due to human errors or equipment and measurement errors.

Figure 5.11 presents the load-displacement graph of specimen 3-1 corresponding to monitoring point 4. The same structural behaviour is observed as the one for specimen 1-1. Both graphs show a correct initial stiffnes but a different response for stiffnesses after the linear stage.

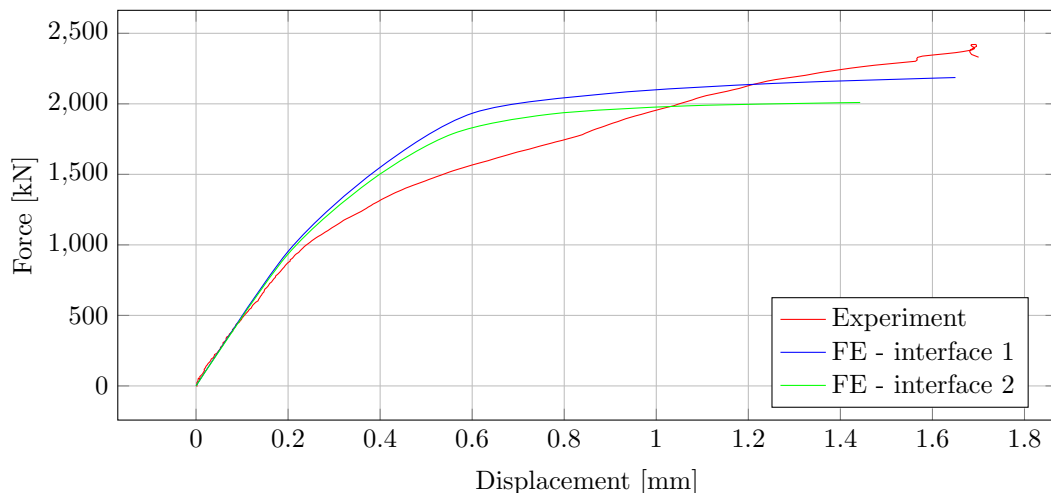


**Figure 5.11: Force-displacement graph of specimen 3-1 corresponding to monitoring point 4**

Noticeable is that the results from Figures 5.10 and 5.11 are selected based on their correctness with the experimental results. This does not insinuate that the results from the other monitoring points showed a complete different behaviour. Most of the results showed a behaviour comparable with the above presented figures, but just to less extent.

## 5.4 Discussion

The goal of this chapter was to validate if interface elements are allowed to use as a modelling technique for the contact area between a ribbed pile and slab with a failure mechanism related to punching shear. The numerical results of specimens 1-1 and 3-1 shows good agreement with respect to the failure mechanism. A clear cone element appeared during the FEM analyses and the corresponding crack development shows strong similarities with experiment observations. The structural responses of both analyses showed a deviation in stiffness after completing the linear phase. The main reason is the decrease of stiffness of the actual experiment after the first internal micro cracks occur, while the numerical model loses its stiffness at a later stage.

- despite of the slight deviations in outcome in the FEM analysis, the results justify the use of mean material parameters for modelling punching shear in ATENA;
- after the linear behaviour of the test specimen, the FEM analysis showed a more stiff response in comparison with the response observed from the experiments. It is believed that this is caused by the implemented smear crack concept. This cracking concept responds with decreased stiffness to cracking first after the crack is fully developed. During the experiment, cracking affects the response of the specimen as cracks are initially formed. To overcome is difficulty, the fracture energy is reduced to decrease the stiffness of the specimen;
- the FEM analyses were able to simulate the crack development that is related to punching shear failure. Although the analyses didn't showed a separate punching cone at ultimate load level, the crack pattern insinuates the shape of a cone element;
- the way of modelling the contact surface between the ribbed pile and slab with interface material in combination with friction properties is legitimate modelling technique. The crack inclination, which is contact surface dependent, showed good agreement with the experimental results;
- different contact surfaces can be modelled by varying the friction parameters.

## Chapter 6

# Finite element modelling of thesis objective

In this chapter the punching behaviour of structural slabs on top of ribbed foundation piles is studied by means of FEM analyses. For the modelling a fictitious slab is considered as illustrated in Figure 6.1.

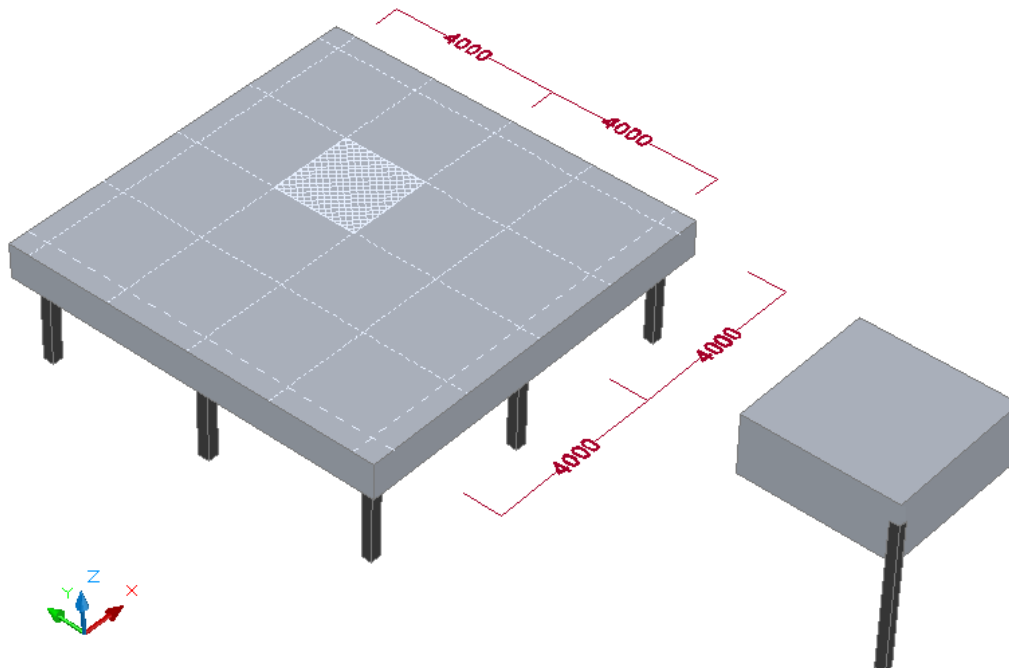


Figure 6.1: Considered field element from a fictitious infinite flat slab

## 6.1 General modelling considerations

Since the type of structural system is not within the range of available numerical and experimental data, only the validation model presented in Chapter 5 can give indications of a proper modelling technique. Since these FEM simulations of laboratory tests conducted by Braam et al. [16] show good agreement with the corresponding experimental results, the contact surfaces between the foundation pile and slab are again simulated with frictional interface elements.

### 6.1.1 Geometrical specifications

The modelled field element relates to a fictitious slab with spans of 4000 mm in both directions and a height of 800 mm. A rectangular ribbed foundation pile of 250 x 250 mm penetrates 500 mm into the slab. In order to reduce the required computer capacity, only a quarter field element of Figure 6.2(a) has been modelled. A quarter is modelled instead of an eighth to be able to model different contact properties per pile side.

Numerical errors often appear when concentrated prescribed displacements are assigned to single element nodes, therefore rectangular 200 x 200 mm steel plates are modelled at slab surface. The plates will avoid this numerical problem and spread the displacement over multiple element nodes. All geometrical specifications are presented in Figure 6.2.

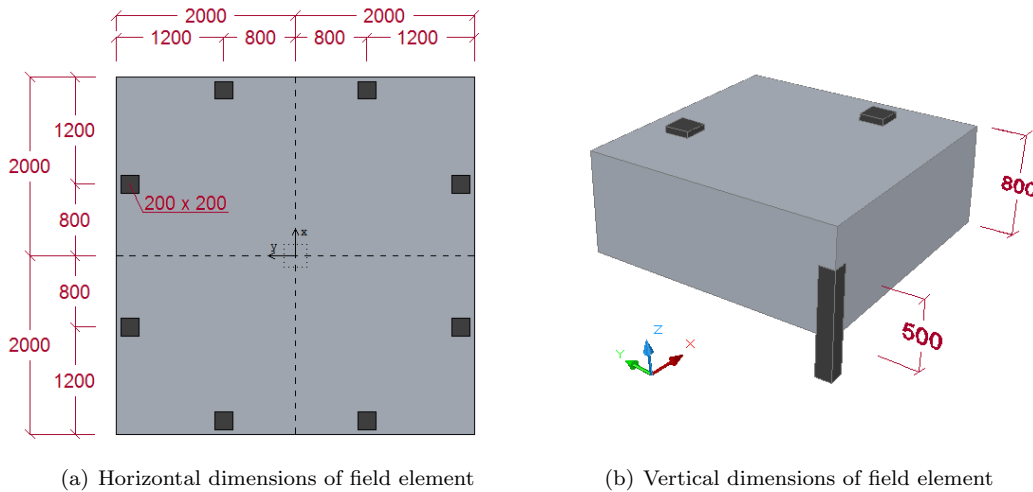


**Figure 6.2: Geometrical specifications of the investigated field element**

The foundation pile is modelled with a shortened length to minimize the amount of structural elements which reduces the run-time of the analysis. This is allowed since the slab behaviour is independent from the pile length.

### 6.1.2 Boundary conditions and loading

In the symmetry planes boundary conditions were introduced such that free movement was prevented in the direction with geometrical continuity. Steel plates are modelled at the bottom of the pile and at the slab surface in order to represent stiff support surfaces.

The modelling principles are described by Figure 6.3. The green dots shown in Figures 6.3(a) and 6.3(b) represents the constrains in x-axis and y-axis to simulate continuity. The bottom of the pile is constrained in z-direction to simulate a fixed foundation pile. Fixed pile movements in vertical direction are due to settlements highly debatable, but it goes beyond the scope of this thesis.

The field element is subjected to a prescribed displacements of 0.25 mm per load step which is located in the center of the steel plates, see Figure 6.3(d). The displacement controlled loading method is used to analyse also the structural behaviour after failure.

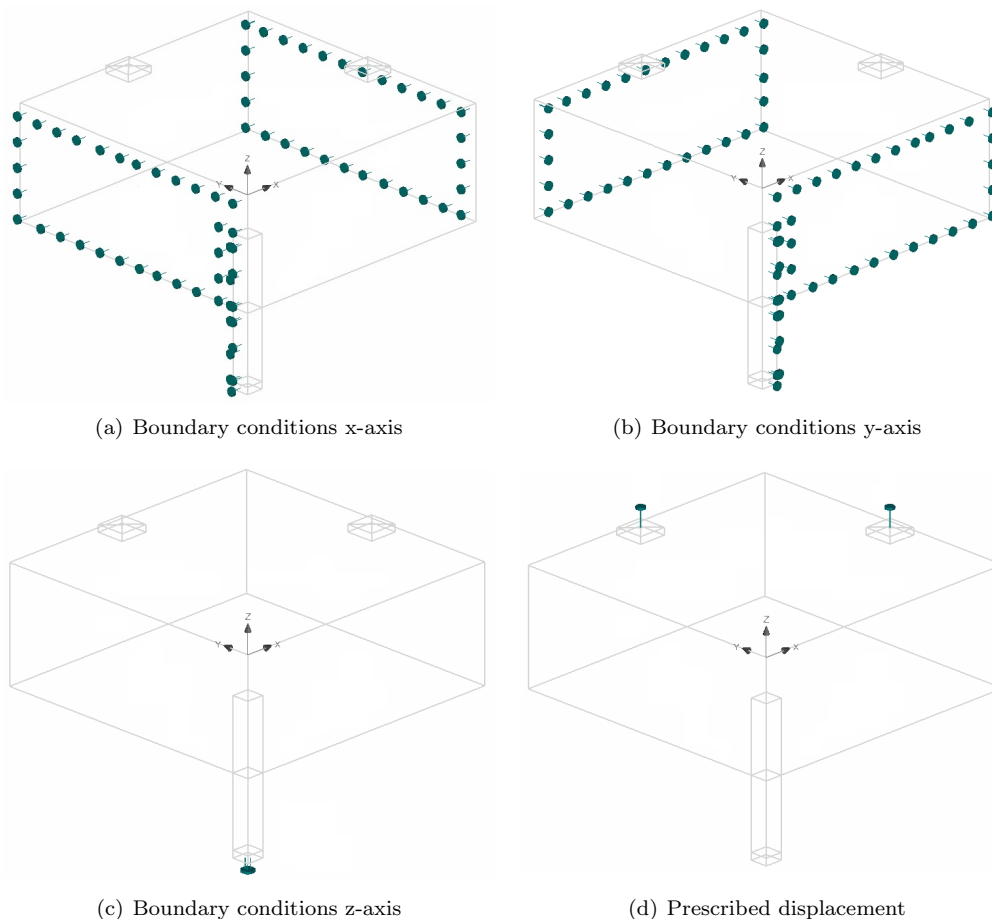


**Figure 6.3: Boundary conditions and loading**

### 6.1.3 Material properties

During the study, for the concrete material fracture-plastic model *CC3DNonLinCementitious2* for non-linear analyses is used as described in Chapter 4.

The concrete material parameters are based concrete class C30/37 which is commonly used in practise. The concrete class has left unchanged during all analyses. The material properties are modelled with mean values to simulate the properties of a real experiment. The material properties are given with Table 6.1.

$f_t$ [N/mm <sup>2</sup> ]	$f_c$ [N/mm <sup>2</sup> ]	$E_c$ [N/mm <sup>2</sup> ]	$G_f$ [N/m]	$\varepsilon_{cp}$ [-]
2.90	38.05	32850	28.75	$1.158 \cdot 10^{-3}$

**Table 6.1: Basic material properties for concrete slab**

The foundation pile is modelled with linear material behaviour to prevent crack formation in this structural member which is not of interest during this study. The modelled elastic modulus of 38000 N/mm<sup>2</sup> corresponds to a concrete class C55/67.

The steel plates are modelled with a linear stress-strain law. The supporting plates don't have a structural function and are only modelled for numerical reasons. Plastic deformation of these supporting plates is not a point of interest. The modelled elastic modulus is 210000 N/mm<sup>2</sup>.

The reinforcement bars are modelled with bilinear material behaviour as described in section 4.1.2. The material properties are base on reinforcement bars with a steel grade of B500, which implies an elastic modulus of 200000 N/mm<sup>2</sup> and a yield stress  $f_y$  of 500 N/mm<sup>2</sup>.

### 6.1.4 Finite elements

The concrete slab is modelled by three dimensional solid linear tetrahedral elements. The concrete pile and the steel plates are modelled with three dimensional solid linear brick elements. As mentioned in Chapter 5, the choice for the linear tetrahedral elements instead of quadratic elements is due to absence of required computer capacity. Although increased number of integration points lead to more accurate FEM results [31], it requires also directly more computer capacity.

The mesh density specially around the pile is increased to improve the accuracy of the analysis in this important region of the slab. To reduce the total analysis capacity the other regions of the slab are modelled with a relative coarse mesh, see Figure 6.4(a).

In the next paragraphs multiple force-displacement graphs are presented. The vertical displacement is measured at two different surface locations. Monitoring point 1 is located near the foundation pile to measure the displacement inside the punching cone perimeter. Monitoring point 2 is located between the two supporting plates to measure the vertical displacement outside the punching cone perimeter. Both monitoring points are shown in Figure 6.4(b).

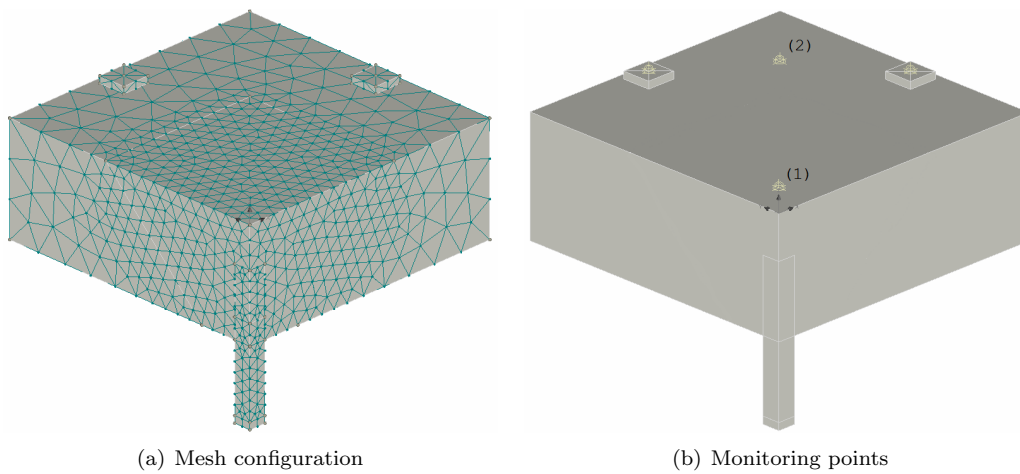


**Figure 6.4: Mesh configuration of modelled specimen and monitoring points**

Table 6.2 shows the mesh type, element type and the number of elements per construction member. It is noticeable that the choice for quadratic elements for the slab should increase the number of element nodes enormously.

<i>Macroelement</i>	<i>Mesh type</i>	<i>Element type</i>	<i>Elements</i>
Slab	3D tetrahedral	linear	9190
Prefabricated pile	3D brick	linear	452
Plates slab surface	3D brick	linear	29
Plate pile base	3D brick	linear	4

**Table 6.2: Finite element mesh generation**

### 6.1.5 Modelling scheme

The aims and the modelling scheme of the simulations are chronologically listed below. The list describes the path along the study is elapsed:

1. simulate punching shear behaviour with different interface material properties;
2. adding reinforcement to slab;
3. adding antisymmetry to slab spans

## 6.2 Boundary limits

The modelling problem of this study is the interface behaviour of the contact area between the ribbed foundation pile and the structural slab. The punching capacity is directly related to the shear transfer between these two construction members. The solution of this problem is limited to two ultimate situations. The lower boundary limit presents a sliding connection and the upper boundary limit represents a perfectly connected contact area. The actual

behaviour lies somewhere in the middle of these two boundary limits. In this paragraph both boundary limits are analysed to study the differences in failure behaviour such as crack development and slab displacements.

### 6.2.1 No interface connection

This situation presents a contact area without frictional properties. Related to this punching shear study, this situation could be a conservative assumption for modelling a smooth pile. It is expected that the slab depth, accountable for punching resistance, is equal to the distance between the pile top and slab surface.

Figure 6.5 presents a load-displacement graph of monitoring point 2. This is the relative displacement with respect to the centre of the slab. Monitoring point 2 is located between the prescribed displacements. The graph shows a failure load of 1100 kN corresponding to a vertical displacement of 1.77 mm. The analysis results show plastic material behaviour during the first load step, which suggests that the linear stage is reached after a load of about 400 kN.

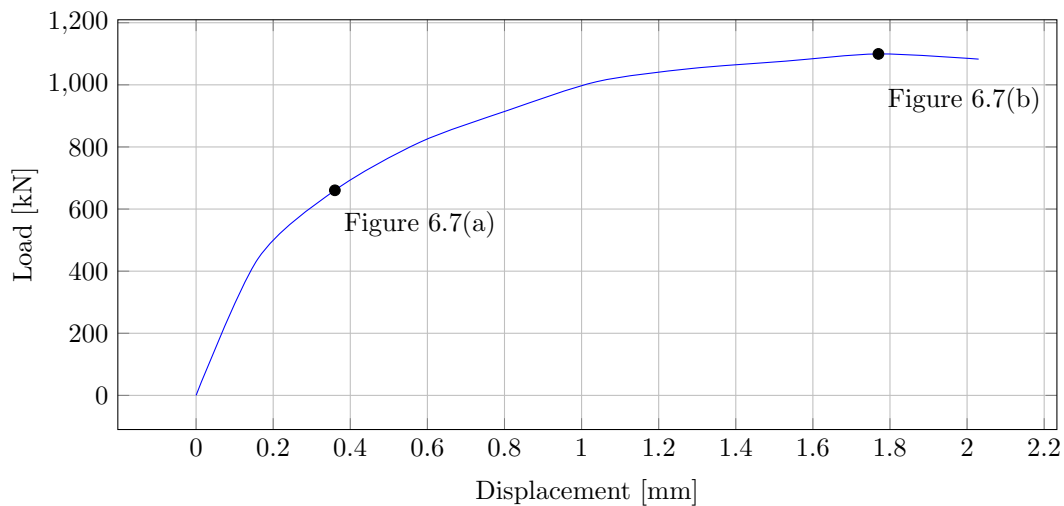


**Figure 6.5: Load-displacement graph of monitoring point 2 corresponding to sliding connection**

The rapid decrease of slab stiffness after the linear stage is explained by the increase of cracked elements at slab surface located around the foundation pile. These cracks are caused by hogging bending moments above the support. The bending stiffness is locally reduced by the presence of the pile and the sliding contact connection between pile and slab. The reduced bending stiffness at the region around the pile results in an increased slab deflection. This deflection stimulates the increase of the crack width at slab surface.

The deformed shape of the slab at failure is shown with Figure 6.6. A scale factor of 50 is introduced to make relative small deformations visible. The sliding behaviour of the contact surface is clearly visible with the low values of vertical displacement just around the pile.



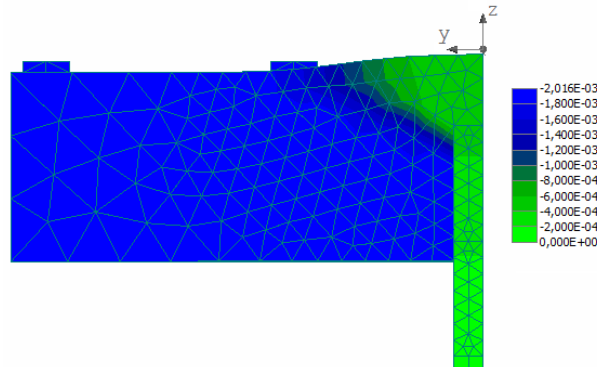


**Figure 6.6:** Vertical slab displacement (z-axis) of field element after failure [m] (scale factor = 50)

Two load steps are briefly discussed to show the crack width development during the analysis up to failure. Figure 6.7(a) shows the crack width at load step 2 which corresponds to a displacement of 0.36 mm of monitoring point 2, see Figure 6.5. Although the crack width during this load step is in the magnitude of micro millimetres, the interior crack development insinuates the shape of a possible punching shear cone. The region around the pile head is the only cracked zone in the total mesh. The crack length and width are increasing during subsequent load steps. Figure 6.7(b) shows the crack width at failure, corresponding to a displacement of 1.77 mm of monitoring point 2. The crack inclination at failure is typical for punching shear which was expected. The shear crack angle is in accordance with the observed shear crack angle of about  $30^\circ$  during experiments conducted by Hallgren et al. [26]. This crack angle is typical for slender structures, where increased slab deflections stimulate the crack width development. From this it can be concluded that the sliding connection leads to a local reduction of the bending stiffness of the slab above the pile.

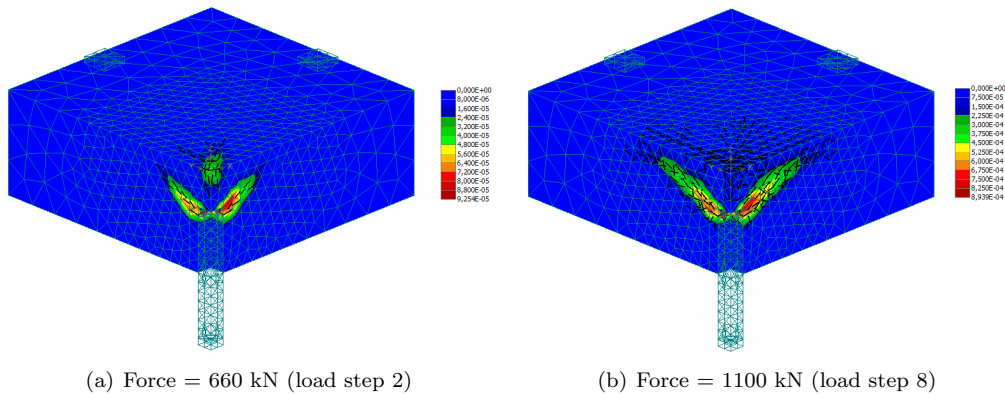


**Figure 6.7:** Crack width (no crack filter) of field element corresponding to no interface connection [m]

The FEM analysis shows that the FIB Model Code 2010 [24] design code, which uses a distance between pile head and slab surface as effective slab height is a conservative code. It is noticeable that the design code assumes a penetrated column without ribs.

## 6.2.2 Perfect interface connection

This situation corresponds to a perfect connection between the ribbed pile and slab. Related to this punching shear study, this situation could be a foundation pile monolithically connected to a structural slab. This situation simulates the upper boundary limit. It is expected that due to the perfect connection the crack initiation starts at the bottom of the slab.

Figure 6.8 presents the load-displacement graph of the considered mesh with perfect interface connections. The displacement corresponds to the vertical displacement of monitoring point 2. The presence of perfect interface connection results in a failure load of 7118 kN, which is significantly increased compared to the failure load of 1100 kN for the analysis without any interface connection.

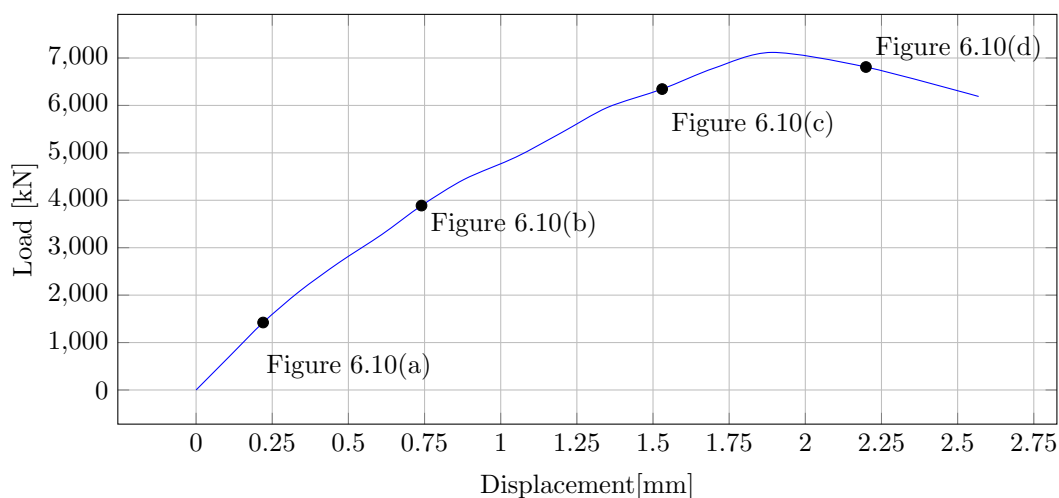
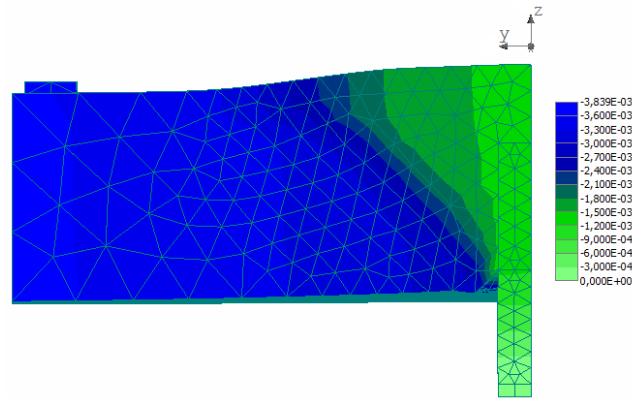


**Figure 6.8: Load-displacement graph of monitoring point 2 corresponding to perfect interface connection**

The brittle failure behaviour of punching shear is clearly visible in this graph. Without any warning the slab fails and the load drops. The deformed shape of the slab at failure is shown in Figure 6.9. A scale factor of 50 is introduced to make relative small deformations visible. The perfect connected behaviour of the contact surface is clearly visible with the vertical displacement of the surrounding concrete around the pile. This figure indicates also the crack angle of the punching cone. The shear crack propagates over the full slab height at an angle of about  $55^\circ$ , measured between the shear crack and the horizontal plane. This crack angle is in accordance with the observed punching angles of about  $50^\circ$  to  $60^\circ$  during experiments conducted by Nylander et al. [36]. These results are highly usable because the experiments consist of specimens with a low span-depth ratio. This is a considerably steeper angle than the shear crack angles observed in punching shear tests of more slender slabs [26].

The difference in shear crack angle is explained by the difference in bending stiffness related to the slenderness ratio. A high slenderness ratio corresponds to relative thin slabs which are more sensitive for bending. The increased deflection will stimulate the crack width development at slab surface, which is undesirable. Low slenderness ratios are less sensitive for bending and more sensitive for shear forces. This leads to a shear crack angle of about  $50^\circ$ . From this it can be concluded that the full slab height is accountable for the bending

stiffness, also the region around the foundation pile. This in contrast to the analysis with no interface connection, where the pile caused a local decrease of bending stiffness.



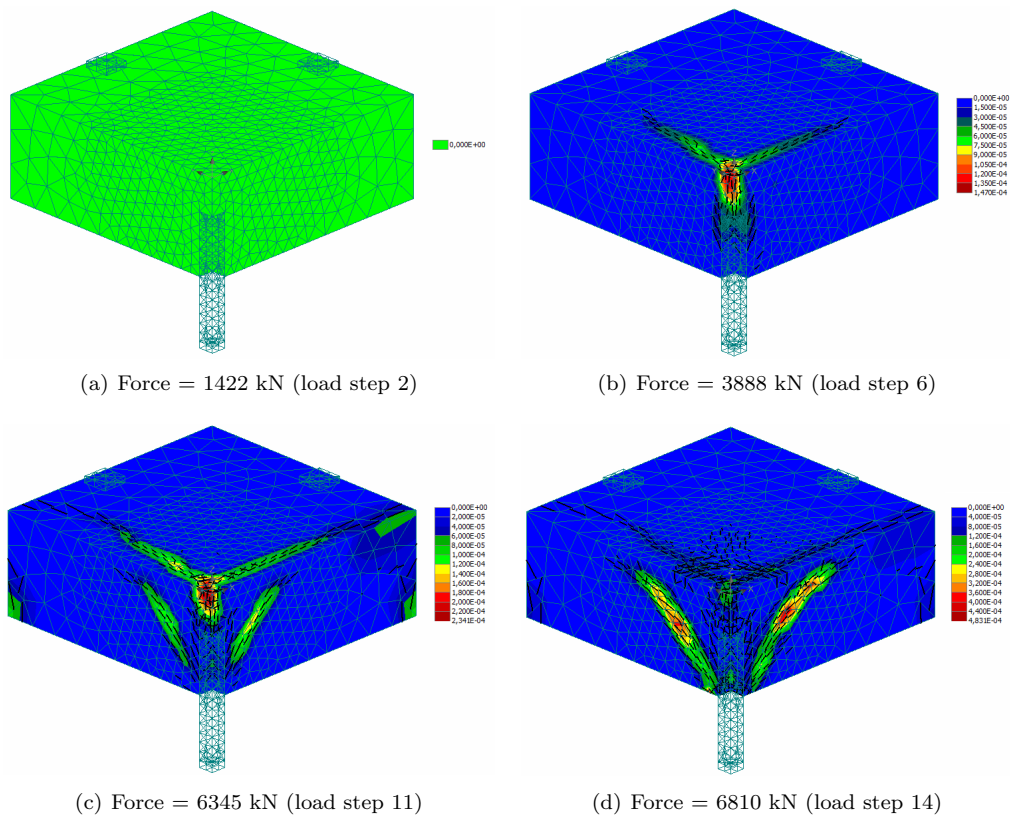
**Figure 6.9: Vertical slab displacement (z-axis) of field element after failure [m] (scale factor = 50)**

Figure 6.10 shows the crack width development during the analysis. During the first two load steps the concrete material is still elastic, this is shown in Figure 6.10(a). The mesh is free of cracks and the slab will return to its original state after removing the load. Load step 2 is related to a load of 1422 kN and corresponding displacement of 0.22 mm, see Figure 6.8.

After the linear stage, the plastic development starts directly above the pile head and spreads at the slab surface towards the element edges, see Figure 6.10(b). This radial crack is in correspondence with the crack development during the experiment conducted by Braam et al. [16] described in Chapter 5. The concrete strain at this load step is only located around the circumference of the pile. During subsequent load steps the radial cracks at slab surface start to increase in length and the first internal cracks start to develop.

At load step 11, Figure 6.10(c), the internal strain results in a crack width of about 0.1 mm. The crack width in the region above the pile head has doubled to about 0.2 mm. From this load step the possible punching cone element is already visible. Figure 6.10(d) presents the crack state just after failure. It is clearly visible that the crack width starts at the bottom of the slab and develops at an angle to slab surface. This indicates that with the assumption of perfect interface connection the full slab height is accountable in punching shear verification.

The assumption of a perfect connection is a progressive statement which will overestimate the actual behaviour. During the next section, different friction properties will be studied to find the optimal Mohr-Coulomb friction parameters.



**Figure 6.10: Crack width (no crack filter) of field element corresponding to perfect interface connection [m]**

### 6.3 Parameter study

The boundary limits described in the previous section are not realistic from practical point of view. The actual behaviour of the contact area lies somewhere in the middle of these ultimate conditions. It is a point of interest to know at which friction properties the full slab height is accountable for punching shear verification. That is why a parameter study is conducted for various combinations of cohesions and friction coefficients. To prevent magnitudes which are not usable from practical point of view, the range for both parameters are based on the results of experimental studies on shear capacity [20, 29]. This resulted in a range for the cohesion from 0.0 to 1.5 and a friction coefficient range from 0.0 to 1.6.

The goal of this parameter study is to find a transition point at which the shear transfer capacity of the contact surface is increased with such a magnitude that the final punching crack starts at the bottom of the slab. This implies a punching failure mechanism which accounts the full slab height, resulting in a significantly increased failure load. All geometrics and material properties are left unchanged during this study. Table 6.3 contains the results of all numerical analyses. The failure load is presented as a function of the cohesion and the coefficient of friction. The failure load of 1084 kN for the analysis with both friction properties equal to 0.0 corresponds like expected to the failure load of 1100 kN for the lower boundary limit discussed in the previous paragraph. The failure loads corresponding to a

friction coefficient of 1.6 are about 20% less compared to the perfect bond connection. A capacity increase of 20% is possible with higher friction coefficient values. From practical point of view a greater value than 1.6 is not reachable and therefore not analysed.

		Cohesion [N/mm <sup>2</sup> ]					
		0.0	0.2	0.5	0.7	1.0	1.5
Friction coef. [-]	0.0	1084	1120	1108	1092	1093	1030
	0.2	1260	1300	1252	1235	1274	1273
	0.5	1768	1778	1773	1770	1735	1768
	1.0	2584	2534	2559	2486	2473	2525
	1.4	5885	5638	5708	5813	5850	5791
	1.6	5792	5806	5761	5708	5917	5820

**Table 6.3: Failure loads corresponding to various combinations of friction coefficients and cohesion [kN]**

Figure 6.11 shows a surface chart of the contents shown in Table 6.3. The influence of the friction coefficient is clearly visible with the steep slope between a coefficient value of 1.0 and 1.4.

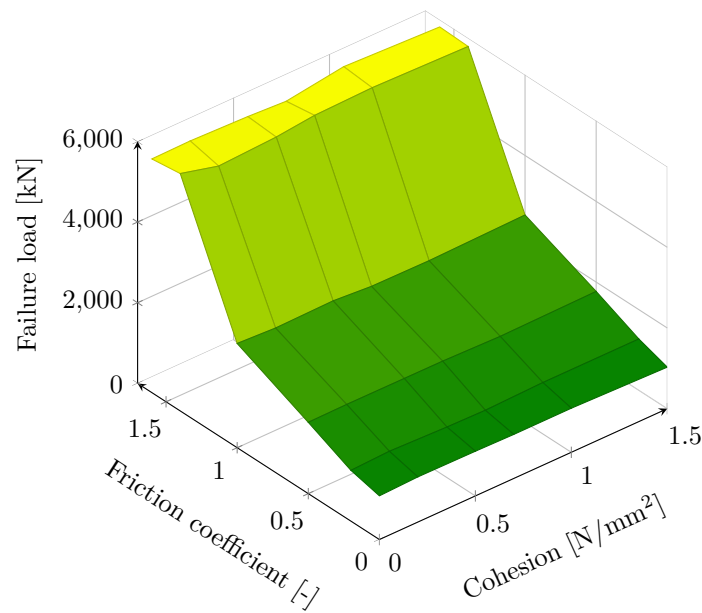


**Figure 6.11: Surface chart with failure loads corresponding to various combinations of friction coefficients and cohesion**

First of all, it can be observed that increasing the cohesion parameter doesn't affect the failure load. This absence of increased capacity holds for all investigated friction coefficients. Cohesion is the term for the force attraction between the two layers of concrete and is formed by a combination of a chemical reaction and micro roughness on both sides of the concrete.

From practical point of view this is important information. When two different concrete layers are cast at different times, the chemical reaction between both concrete mixtures is very limited since the concrete mixture of the foundation pile is already hydrated. No chemical reaction at all between the two construction members is for that reason a conservative but practical assumption. Typical values for the cohesion of monolithic concrete is in the range of  $f_c/4$  [17]. This is based on a connection caused by chemical reactions. This means for the modelled concrete compression strength of  $38.05 \text{ N/mm}^2$ , the cohesion magnitude should be in order of  $9.5 \text{ N/mm}^2$  to ensure a perfect cohesion. Since experimental studies [20, 29] into friction parameters found cohesion values up to  $1.7 \text{ N/mm}^2$ , the order of magnitude to reach perfect connection is out of the range. That is why the shear transfer capacity is not positively influenced by low values of cohesion.

On the positive side, increased values of friction coefficients lead to significantly more punching capacity of the slab. This coefficient describes the ratio of the force of friction between two bodies and the force pressing them together. The compression force results from the bending component in combination with the confined slab. The coefficient of friction depends on the used materials, e.g. ice on rubber has a low coefficient of friction, while steel on rubber relates to a relative high coefficient of friction. A significantly increase in slab capacity occurs between a coefficient of 1.0 and 1.4, which is clearly shown in Figure 6.11. The difference in failure load is explained with the difference in failure mechanism.

Roughly two failure mechanism can be distinguished:

1. punching cone starting from pile head to slab surface;
2. punching cone starting from slab bottom to slab surface.

The first mechanism occurs for friction coefficient values less or equal to 1.0 and the second mechanism occurs for coefficients values more than 1.4. Between these two clear failure mechanisms, a transition zone appears. This transition zone is described with unpredictable failure behaviour. A cross-section of Figure 6.11 is shown in Figure 6.12 for a constant cohesion value of  $1.0 \text{ N/mm}^2$ . The three distinguished zones are discussed during the next sections.

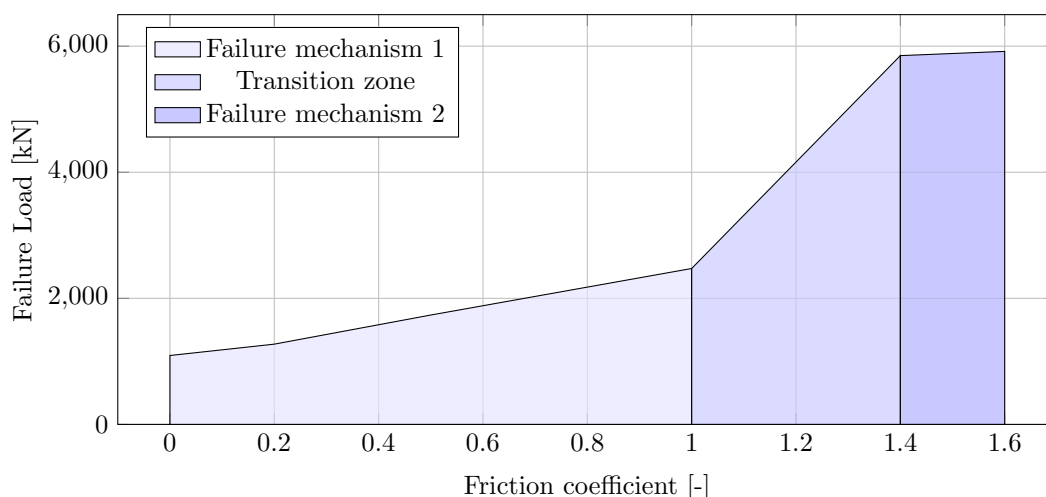


Figure 6.12: Failure load - Friction coefficient graph (Cohesion =  $1.0 \text{ N/mm}^2$ )

### 6.3.1 Failure mechanism 1

The first mechanism occurs when the friction parameters of the contact area are not capable of transferring the introduced shear forces from slab to foundation pile. From theoretical point of view this means:

$$\tau_E \geq \tau_R \tag{6.1}$$

Where  $\tau_E$  = applied shear stress [N/mm<sup>2</sup>]  
 $\tau_R$  = resisting shear stress [N/mm<sup>2</sup>]

The  $\tau_R$  is calculated by making use of equation (2.14) which consists both friction parameters. The result is sliding contact surface with a punching cone which starts at the pile head towards the slab surface. Figure 6.13 shows the development of principal fracture strain which is typical for this failure mechanism. The shown strain development is related to a cohesion of 1.0 N/mm<sup>2</sup> and a friction coefficient of 1.0.

Like presented in Table 6.3, this combination of parameters correspond to a relative low slab capacity due to the small punching cone perimeter. Figure 6.13(b) shows the final fracture strain at slab failure which indicates that only the topside of the slab is accountable for punching resistance. The punching cone shows similarities with the punching cone shown in Figure 6.6, representing no interface connection between pile and slab.

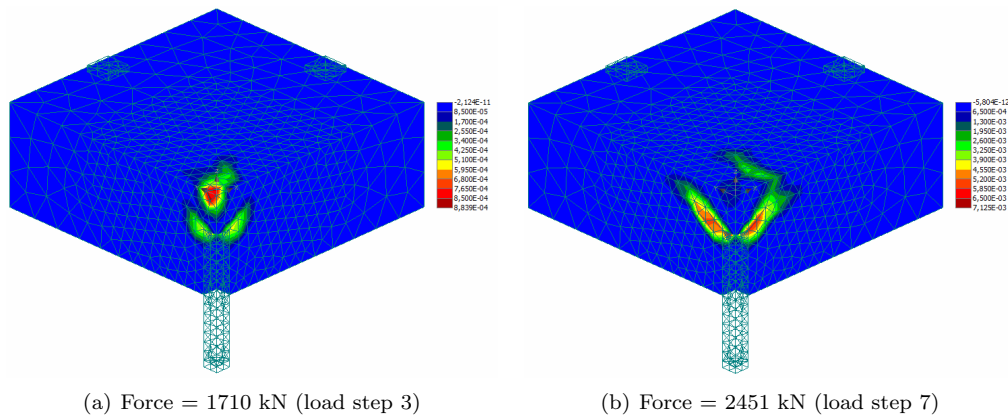


**Figure 6.13:** Development of principal fracture strain [-] ( $c = 1.0 \text{ N/mm}^2$ ,  $\mu = 1.0$ )

### 6.3.2 Transition zone

Figure 6.12 indicates that there is a turning point in failure mechanism between the corresponding friction coefficients. FEM analyses show that the area between the 1.0 and 1.4 is a transition area with unpredictable punching shear behaviour. This is visible with the different graphs shown in Figure 6.14. The blue line represents the structural behaviour corresponding to a friction coefficient of 1.2 and a cohesion of 1.0 N/mm<sup>2</sup>. The line is unpredictable and doesn't show a clear failure mechanism. The blue line insinuates that after the first cone element has developed from pile head to slab surface, each following load step

results in a piecewise failure of the interface area which stops when the bottom of the pile has been reached. From practical point of view, this could be the piecewise failure mechanism of separate ribs on a pile during a load increment. The red and green line, corresponding to respectively a friction coefficient of 1.0 and 1.4, show a more predictable and smooth behaviour with a clear failure load.

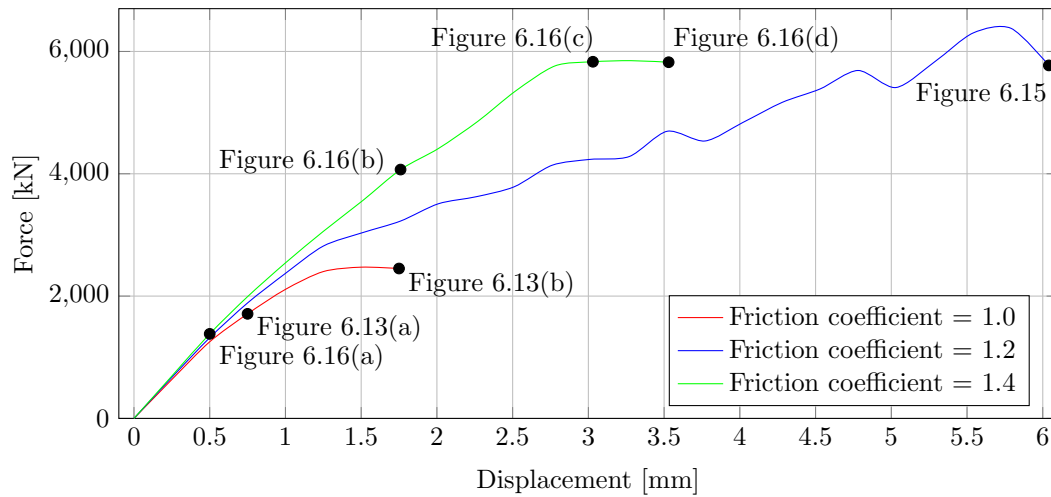


Figure 6.14: Load-displacement graph of monitoring point 2 corresponding different friction coefficients (Cohesion = 1.0 N/mm<sup>2</sup>)

Figure 6.15 shows the fracture strain at failure. The final shear crack propagates from top to bottom, which corresponds to the large punching cone. It is the unpredictable behaviour up to the failure load which makes the friction coefficient of 1.2 undesirable.

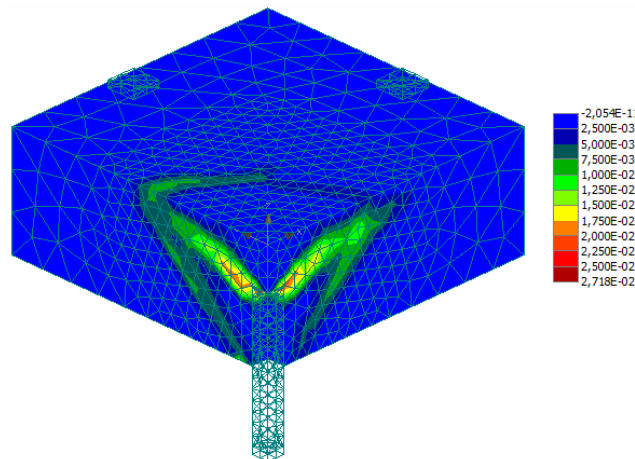


Figure 6.15: Principal fracture strain at failure [-] ( $c = 1.0 \text{ N/mm}^2$ ,  $\mu = 1.2$ )



### 6.3.3 Failure mechanism 2

During the analysis with perfect shear transfer, the reached failure load was 7118 kN. This failure load differs with about 20% from the failure load corresponding to a friction coefficient of 1.4. The reason for this increase is the difference in failure mechanism compared to the mechanism which occurred with a friction coefficient of 1.0.

Like shown in Figure 6.16, the full slab height is accountable for punching resistance. This is caused by an adequate shear transfer between pile and slab. Figure 6.16(a) corresponds to the linear stage which is visible by extremely small magnitudes of the strain. Figure 6.16(c) shows what happens when the contact surface is capable of shear force transfer. After 'failure mechanism 1' is fully developed from pile head to slab surface, the second internal punching cracks start to develop. This second crack initiation introduces a new failure mechanism with relating increase of failure load. Because the larger the punching cone, the greater the concrete resistance against this failure mechanism. Figure 6.16(d) corresponds to an applied load just after failure. The final occurred failure mechanism shows strong similarities with perfect interface connection.

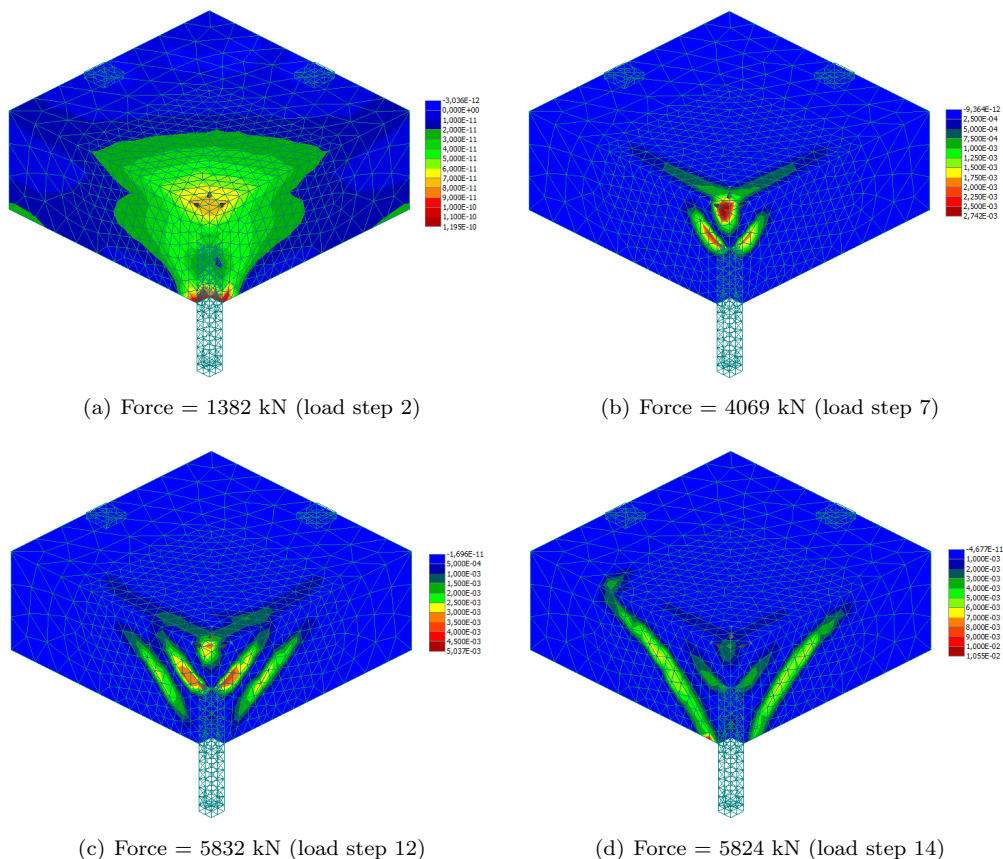


Figure 6.16: Development of principal fracture strain [-] ( $c = 1.0 \text{ N/mm}^2$ ,  $\mu = 1.4$ )

### 6.3.4 Numerical analyses vs. experimental studies

During the parameter study various combinations of friction parameters are investigated. The result is that for the modelled field element, the friction coefficient should be at least 1.4 for a failure mechanism which accounts the full slab height for punching shear resistance. This failure mechanism is highly desirable since this results in a significant increase of the slab capacity. From the value of 1.4, the contact area is capable enough to transfer the introduced shear stresses from slab to pile. The result is that the length of the penetrated pile is accountable in the total length of the effective depth of the slab. For values less than 1.4, the applied shear stresses are larger compared to the shear resistance, resulting in a small punching cone.

Although extensively experimental research into ribbed surfaces is necessary to determine the practical friction parameters, the current knowledge shows (discussed in section 2.4) that the found parameters during the FEM analyses are not necessarily unreachable from practical point of view. The coefficient of friction is the critical parameter. Based on experimental results, the minimum required value is feasible. It is important to mention that these results are without safety factors. If safety factors are taken into account, like in the Dutch design code EC 2 [10], the minimum required friction coefficient is not complied. The EC 2 prescribes a friction coefficient of 0.9 for indented surfaces which corresponds with respect to the numerical analyses to a reduced slab capacity.

Extensively research into the shear capacity of ribbed surface is necessary to verify the need of a safety factor.

## 6.4 Influence of reinforcement

The specimen considered in the previous sections are unreinforced structural slabs. The influence of longitudinal reinforcement on the punching shear strength is debatable since the American design code ACI 318-08 [1] doesn't include a reinforcement factor in its verification formula, while the Eurocode 2 [10] accounts for present reinforcement. During this section a comparison is made between different reinforced slabs. The modelled reinforcement is divided into longitudinal reinforcement (bending reinforcement) and stirrups (shear reinforcement). By dividing the types of reinforcement over multiple analyses, the influence can be obtained separately from each other. The interface conditions ( $c = 1.0$  and  $\mu = 1.5$ ) are unchanged during the analyses.

### 6.4.1 Bending reinforcement

The slab is firstly modelled with a longitudinal reinforcement grid of  $\varnothing 25-200$  at the top and bottom side of the slab. This represents a reinforcement ratio of 1.23 %, which is an often used reinforcement ratio from practical point of view [53]. Figure 6.18 presents the modelled reinforcement layout.

The influence of longitudinal reinforcement is as expected not significantly with regard to the punching shear capacity. The failure load increased from 5699 kN to 6062 kN, which is an increase of about 6%. Figure 6.17 shows a load-displacement of both analysis.

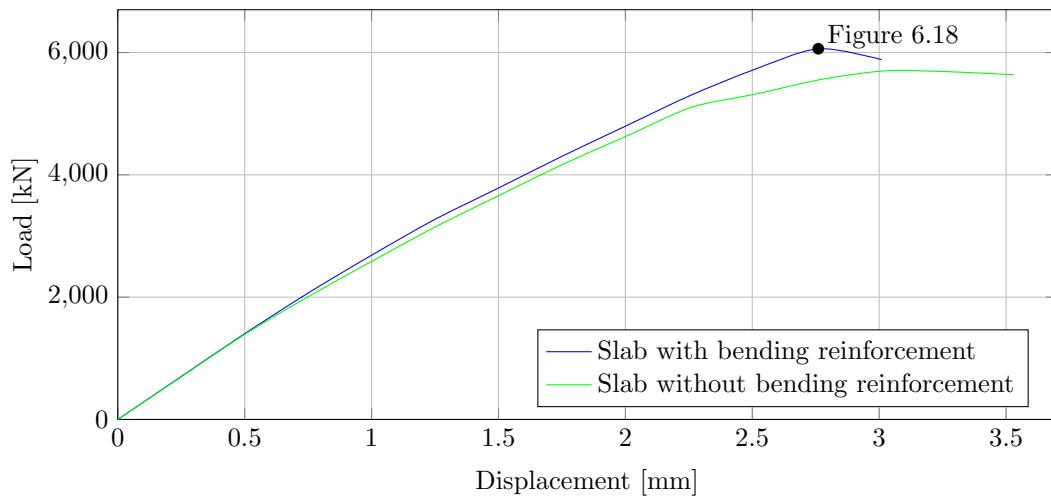


**Figure 6.17: Reinforced vs. unreinforced load-displacement graph ( $c = 1.0$  and  $\mu = 1.5$ )**

The slight increase of the slab capacity is explained by the rather low span/depth ratio of the considered slab. The combination of shear forces and bending moments cause punching failure [13]. Due to the small span with respect to the slab height, the failure mechanism depends more on the bending moments than to the shear forces. Because the bending moments are not governing in the occurring failure mechanism, the influence of flexural reinforcement is almost negligible. This is experimentally validated by Hallgren et al. [36] with punching shear tests on column footings with low span/height ratios. Their conclusion was that the ratio of flexural reinforcement only slightly influenced the punching shear strength. The brittle behaviour is explained by Figure 6.18 which shows the principal stress of the reinforcement at failure.

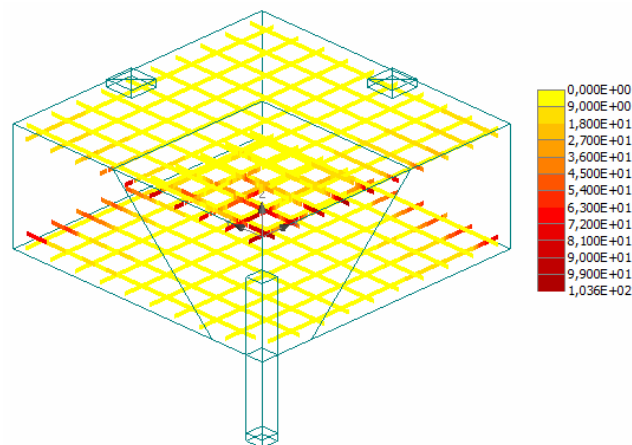


**Figure 6.18: Principal stress of bending reinforcement at failure [ $\text{N}/\text{mm}^2$ ]**

Longitudinal reinforcement bars become active when the flexural deformation starts to increase in tensile regions. These regions are above the support and at mid-span. The maximum tensile stress in the reinforcement bars reach a magnitude of about  $104 \text{ N/mm}^2$ . This is just 20% of the modelled steel capacity. The unreinforced slab shows a more ductile behaviour before slab failure due to the increased crack widths with corresponding stiffness reduction. These crack widths are limited during the analysis with longitudinal reinforcement.

The occurring crack pattern during failure shows strong similarities with the pattern observed during experimental studies with two-way reinforcement [48]. The occurring crack pattern behaves like a net, especially in the area near the column. The explanation for this crack pattern is the state stress that is orientated to the direction of the reinforcement. This direction results in a bi-directional stress state, which causes a crack pattern as shown in Figure 6.19.

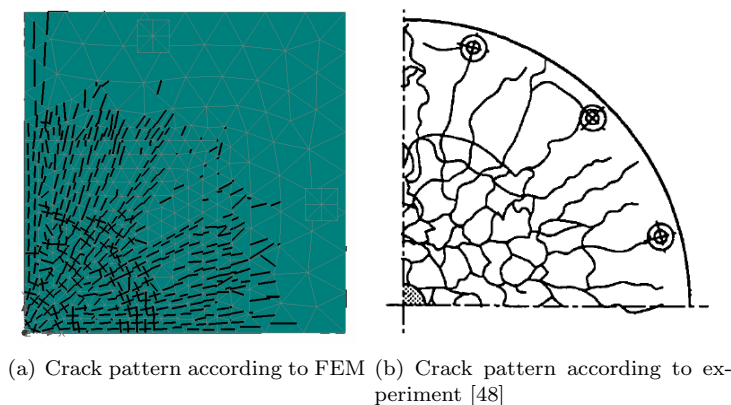


**Figure 6.19: Top view of specimen with cracked elements after failure (no crack filter)**

The crack development observed during FEM analyses without bending reinforcement showed a more predictable pattern with one or two concentrated major cracks. The presence of reinforcement steel leads to an increased number of cracks but simultaneously to a crack width reduction.

#### 6.4.2 Shear reinforcement

Shear reinforcement is added to the numerical model. It is expected from experimental results based on slabs with shear reinforcement [36] that adding stirrups has a positive influence on the slab capacity. Especially for slabs with low slenderness ratios, where shear forces are more governing compared to the bending forces. Stirrups are situated near the foundation pile where high values of shear stress are located. The shear force transfer mechanism is presented according to the so called *truss analogy*. The analogy makes use of compression struts and tensile ties as mechanism to transfer shear forces. Concrete behaviour is weak under tension which results in fracture of the tensile tie. By adding shear reinforcement at these locations, the steel functions as tensile ties in the truss analogy. This results in an increased shear capacity of the slab.

The goal is to investigate to what extent stirrups does influence the failure mechanism and therewith the slab capacity. The modelled  $\text{Ø}16\text{-}150$  stirrups are based on practical assumptions [53]. Figure 6.20 shows a top view the pile with both bending and shear reinforcement layouts.

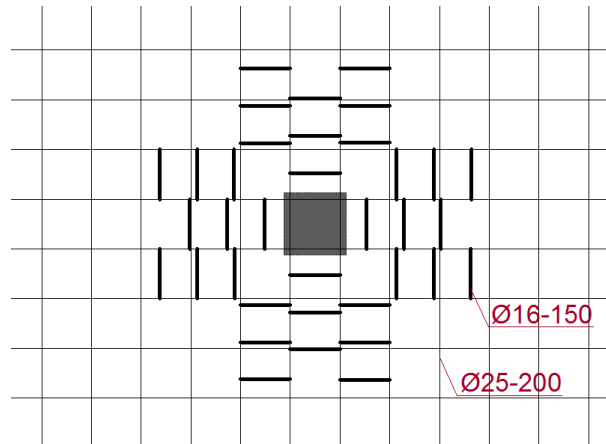


**Figure 6.20:** Shear reinforcement layout located around the foundation pile

During the analyses without reinforcement, it was concluded that the influence of the cohesion is neglectable for the slab capacity. It was the friction coefficient which influenced the failure load. It is against this background that during this section the cohesion remains constant at  $0.5 \text{ N/mm}^2$  and only the friction coefficient variates. The modelled friction parameters are in accordance with Table 6.3.

As expected, the slab capacity increased significantly with shear reinforcement, as shown in Table 6.4. This emphasises the conclusion that for slabs with a low span to depth ratio, the shear failure is the decisive failure mechanism. Table 6.4 presents the failure load corresponding to analyses with shear reinforcement and without shear reinforcement.

<i>Friction coefficient</i> [-]	<i>Failure load without stirrups</i> [kN]	<i>Failure load with stirrups</i> [kN]	<i>Ratio</i> [-]
0.0	1108	4165	3.8
0.2	1252	5079	4.1
0.5	1773	8276	4.7
1.0	2559	10824	4.2
1.4	5708	11220	2.0
1.6	5761	11240	2.0

**Table 6.4:** Comparison of failure load for slab with and without shear reinforcement

First of all it is noticeable that for all friction coefficients an increase of slab capacity is observed. A change in failure load ratio occurs between a friction coefficient of 1.0 and 1.4. The ratio for friction coefficients up to 1.4 is roughly a factor four, while during analyses with coefficients from 1.4 a ratio is observed of roughly two. The increase of slab capacity is clearly visible with the graphs shown in Figure 6.21.

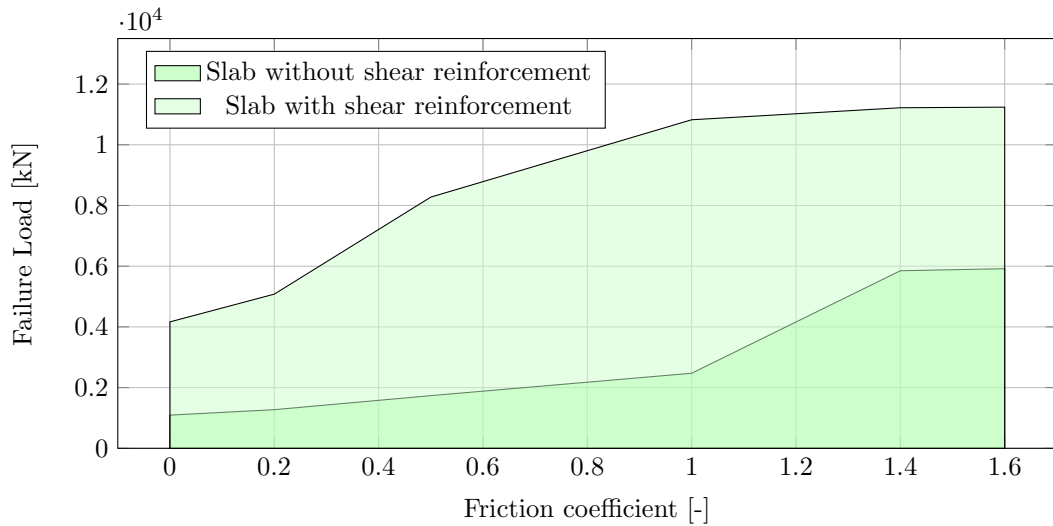


Figure 6.21: Failure load - Friction coefficient graphs ( $c = 0.5 \text{ N/mm}^2$ )

It is important to mention that from a friction coefficient of 1.0 the failure behaviour changed from brittle to ductile. This change in behaviour results in an inaccurate failure load due to the absence of a clear drop after slab failure. This is explained by the structural behaviour graphs shown in Figure 6.22.

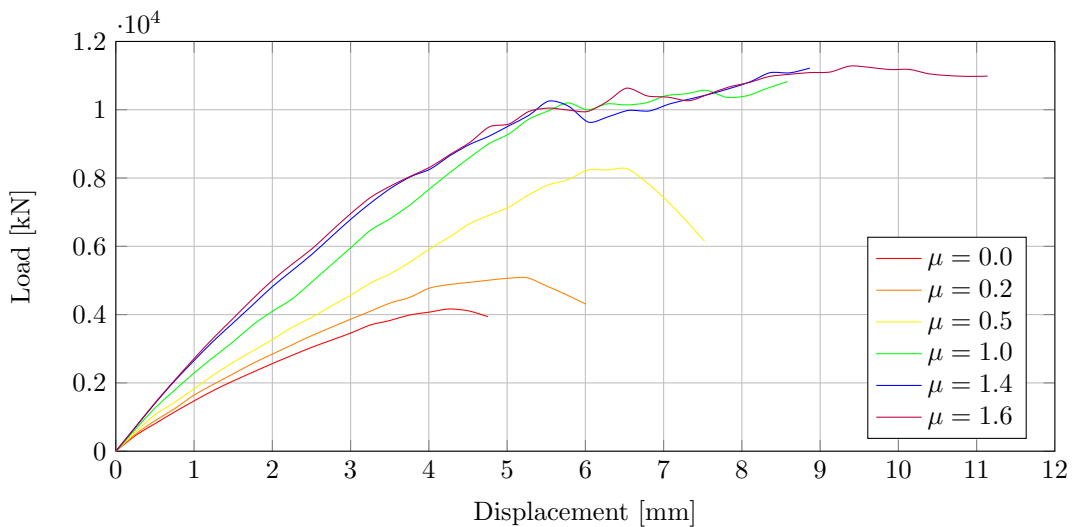


Figure 6.22: Load - Displacement graph for different friction coefficients

For all different friction coefficients the corresponding structural behaviour is shown. The load - displacement graphs can roughly be divided into two failure mechanisms:

- *brittle failure*, which is characterised by a sudden failure;
- *ductile failure*, which is characterised by a rapid increase of deflection for al slight increase of load.

Both failure mechanisms are discussed in the next sections.

### Brittle failure

The brittle failure mechanism is characterised by a sudden failure along an inclined crack. This mechanism relates to a failure without structural warning, e.g. large deflection before failure. This failure mechanism is observed for friction coefficients up to 1.0.

The slab capacity increased from 1773 kN to 8276 kN for a friction coefficient of 0.5 by the addition of shear reinforcement. This is an increase of about the factor 4.7, which is caused by an increased shear capacity. The addition of the modelled shear reinforcement does not result in a different failure mechanism. The shear transfer between pile and slab is increased but not adequate to develop a punching cone over the full slab height. The crack initiation starts at the top area of the foundation pile. This is shown in Figure 6.23, which presents the principal fracture strain of the concrete at slab failure. This figure corresponds to a friction coefficient of 0.5, nevertheless, the observed crack development also applies to lower coefficient values. The inclined shear crack is clearly visible.

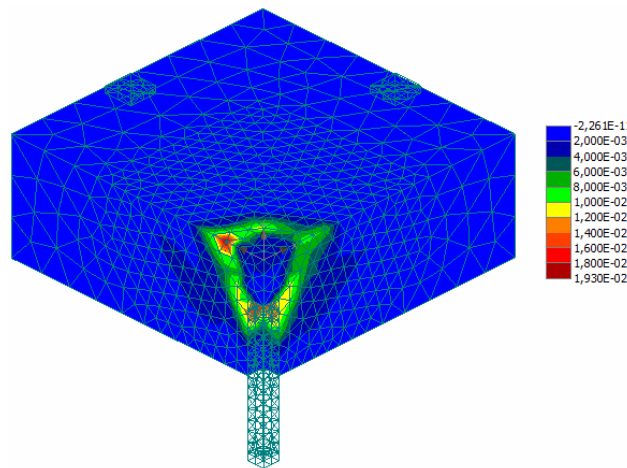


**Figure 6.23:** Principal fracture strain at failure [-] ( $c = 0.5 \text{ N/mm}^2$ ,  $\mu = 0.5$ )

The brittle behaviour is explained by the stress and strain state of the reinforcement at failure, shown in Figure 6.24.

The yield stress of  $500 \text{ N/mm}^2$  is only reached in the inner stirrups, while the outer stirrups are practically not active. This indicates that not all stirrups are fully used in the shear transfer mechanism. The principle strain shown in Figure 6.24(b) shows that only a very small part of all stirrups are subjected to a strain which reaches the failure strain of 45%

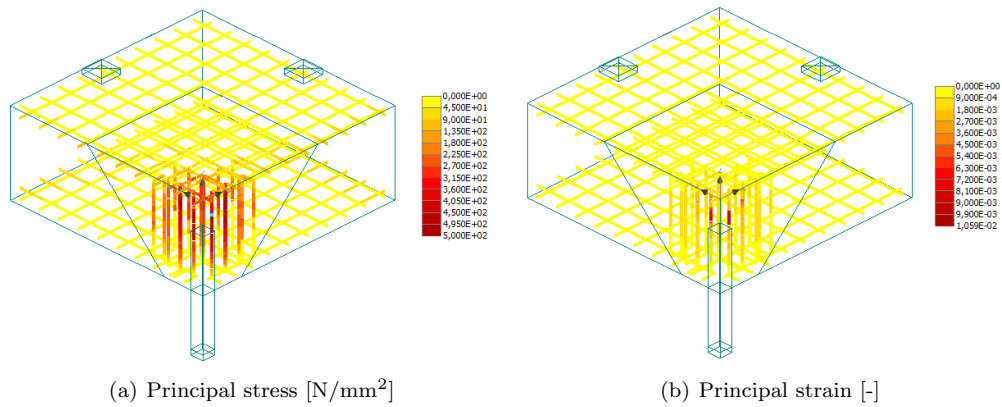


**Figure 6.24: Principal stress and strain at failure ( $c = 0.5 \text{ N/mm}^2$ ,  $\mu = 0.5$ )**

for steel bars. All other stirrups are only subjected to very low magnitudes of strain. The reinforcement bars have a great capacity left before failure. This indicates that the failure is caused by concrete fracture and therefore the corresponding brittle failure behaviour.

### Ductile failure

The ductile failure is characterised by rapid increase of the deflection for a slight increase of the load. This mechanism is highly desirable since large deflections indicate an upcoming failure.

Figure 6.25 presents the principal fracture strain of the concrete at a load of 10984 kN corresponding to a friction coefficient of 1.6. The zones with high values of concrete fracture strain indicate the perimeter of the punching cone. The presentation of strains is also observed for friction coefficients with a value more than 1.0.

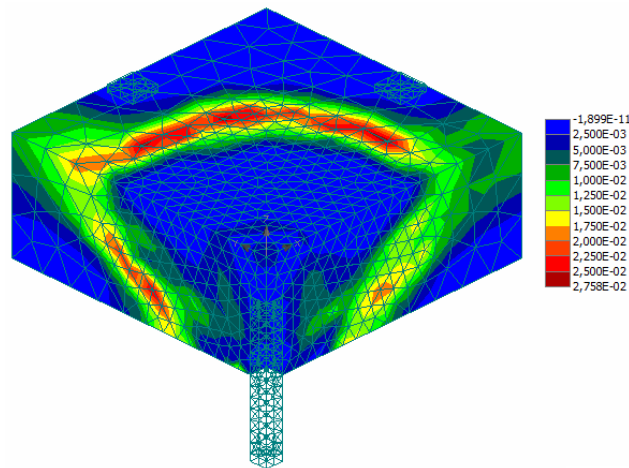


**Figure 6.25: Principal fracture strain at failure [-] ( $c = 0.5 \text{ N/mm}^2$ ,  $\mu = 1.6$ )**



A friction coefficient of 1.0 is adequate to ensure an active shear transfer from pile to the slab. The result is that all stirrups are optimal used in the truss analogy for shear transfer. This results in a shift of the shear crack propagation from the foundation pile to the outer stirrups.

The ductile structural behaviour is explained by Figure 6.26, which shows the stress and strain state of the reinforcement before failure.

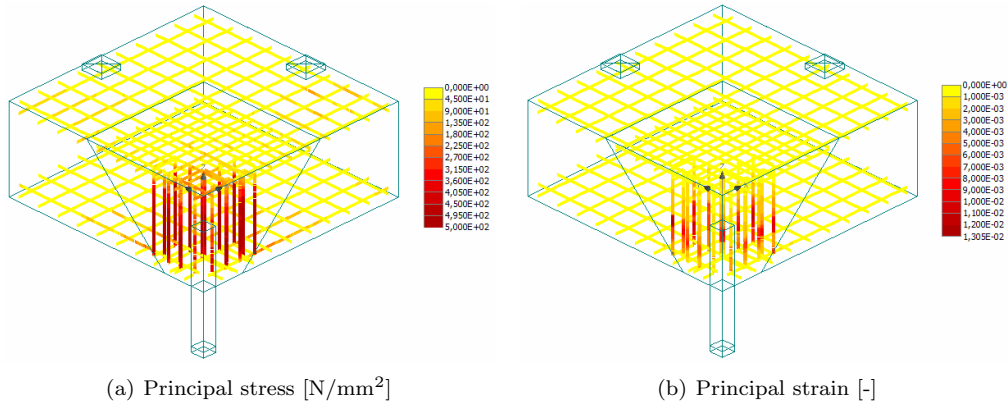


**Figure 6.26: Principal stress and strain at failure ( $c = 0.5 \text{ N/mm}^2$ ,  $\mu = 1.6$ )**

All shear reinforcement bars reach the yielding stress of  $500 \text{ N/mm}^2$ , which indicates that all bars are active in the shear transfer. Because all stirrups are active, the shear crack shifts away from the pile towards the outer stirrups. Figure 6.26(b) shows that the bars do not have reached their ultimate strain capacity. This means that the displacement could increase further until the ultimate steel strain of  $45\%$  is reached.

## 6.5 Influence of a smooth pile surface

Up to this paragraph, the foundation pile is modelled with ribbed interface properties at two sides, which represents a pile with four ribbed sides because of the introduced symmetry lines. Usually, manufacturers fabricate foundation piles in horizontally orientated steel moulds. After concreting the pile, it is more convenient to smooth the top surface. The result is a pile with three ribbed sides and one smooth side. The numerical simulation of a pile with three ribbed sides and one side smooth is not performed because of symmetry reasons. Therefore, an analysis to a pile with two smooth sides and two ribbed sides is performed.

From chapter 5 it can be concluded that the influence of one smooth side was not significant for the final the punching shear crack. Noticeable is that the considered specimen was prestressed, which resulted in an increased shear capacity of the contact area with respect to the Mohr-Coulomb friction law due to the increase of compression forces.

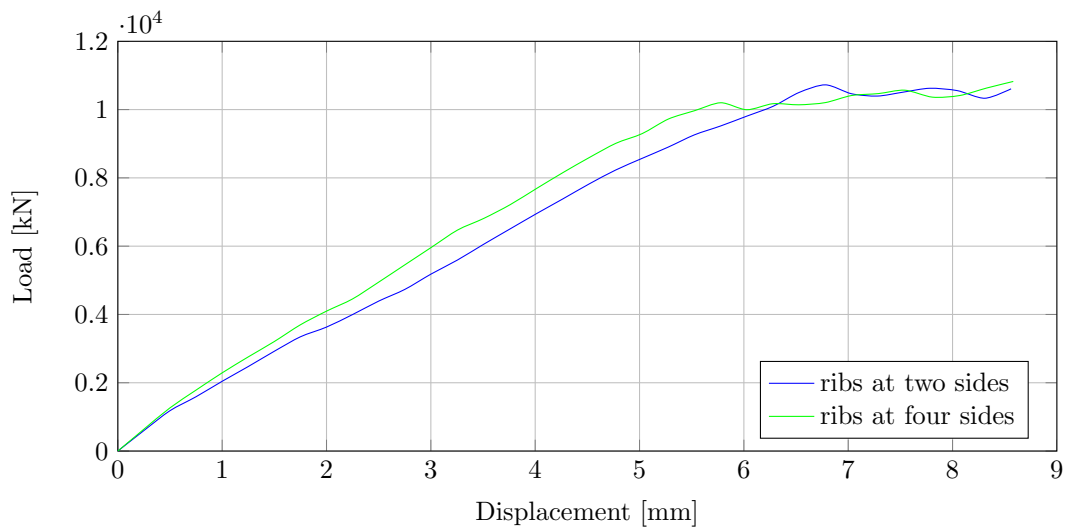
Bases on chapter 5, it is expected that the presence of one smooth side will not result in a significant change of failure mechanism. The friction properties of the smooth side are based on the Eurocode 2 [10] provision, see Table 2.3. The friction properties of the ribbed side are based on the results of the parameter study.

Table 6.5 presents the modelled surface conditions with the associated friction properties. The analysis is conducted with the presence of bending and shear reinforcement.

<i>Surface condition</i>	<i>Cohesion</i> [N/mm <sup>2</sup> ]	<i>Friction coefficient</i> [-]
Smooth surface	0.5	0.2
Toothed surface	1.0	0.5

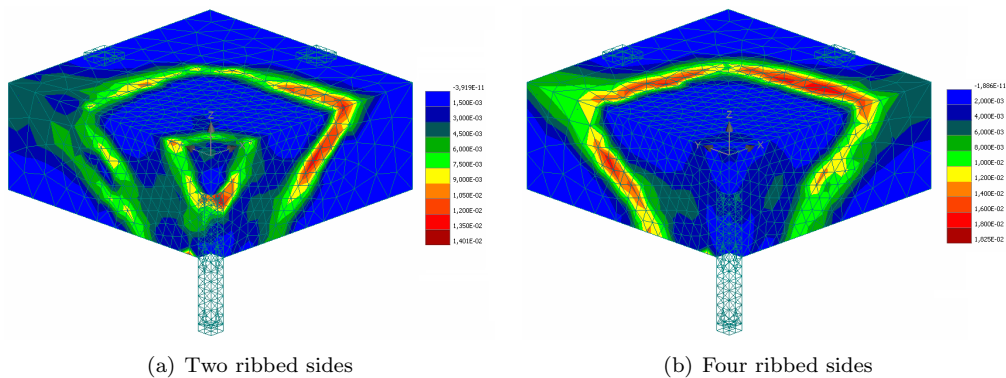
**Table 6.5: Surface conditions with associated cohesion and friction coefficient values**

Figure 6.27 shows the load-displacement graphs up to failure of both analyses. It is visible that the ultimate failure load is practically the same for both analyses. A difference in structural behaviour is noticed after the linear stage. The reduction of structural stiffness is explained by the crack formation at the region around the smooth side of the pile. The decrease in shear transfer capacity of the smooth contact area results in an increased crack development.



**Figure 6.27: Load - Displacement graph for different pile conditions**

The decrease of slab stiffness after the linear stage for the analysis with the smooth side is also visible by Figure 6.28. Initially, the reduced shear capacity of the smooth pile side results in a small punching cone. This is visible with the reduced slab stiffness after the linear stage. After the small punching cone has fully developed, a latter punching cone starts to develop. From this point, the slab behaviour with the smooth side is similar to the slab behaviour with four ribbed sides. This is visible by the same structural stiffness after a load of about 4000 kN.



**Figure 6.28: Principle fracture strain at failure for different pile conditions [-]**

It can be concluded that the influence of two smooth pile sides is not significant with respect to the failure load and the overall structural behaviour. A slight decrease in structural stiffness is observed after the linear stage which is caused by crack formation at the smooth pile side. After this crack formation, the stiffness is similar to the stiffness of the specimen with four ribbed sides.

## 6.6 Non symmetric load conditions

Up to this section, the punching shear behaviour is studied for symmetric load conditions. These conditions are ideal situations with respect to deflections and the corresponding distribution of stresses in a concrete slab. Load eccentricity introduces additional bending moments and affects the shear stress distribution. However, in practice, there are many instances where loading, geometry and reinforcement around foundation piles differ significantly from ideal axis-symmetrical conditions. During this section the influence of non symmetric conditions on the punching behaviour is analysed.

Eurocode 2 [10] provides a  $\beta$  factor ( $\geq 1.0$ ) to account for eccentricities. The external punching load should be multiplied by this  $\beta$  factor which depends on the rate of eccentricity, i.e. internal columns or edge columns. For internal columns a  $\beta$  factor of 1.15 can be used as approximation [11].

To add non symmetry to the model, one of the two steel supporting plates is removed from the slab surface. All other geometrical properties of the slab are left unchanged. Figure 6.29 presents the introduced non symmetric model.

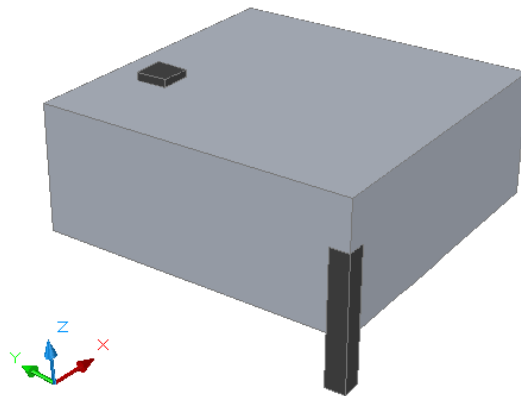


**Figure 6.29: Considered field element with non symmetric load condition**

In 2010, Sagaseta et al. [33] investigated the punching shear capacity of non axis symmetrical slabs without transverse reinforcement. Square specimens of 3000 x 3000 mm and a depth of 250 mm were tested. The specimens were vertically supported at four locations near the specimen edge. A centric located pile force generated a displacement controlled load.

The experimental set-up and the observed crack pattern are shown in Figure 6.30.

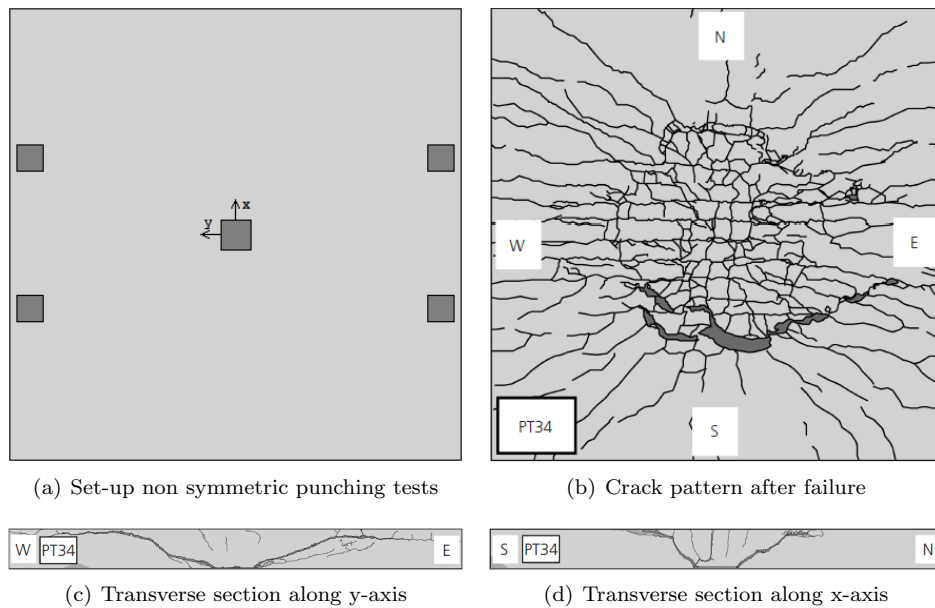


**Figure 6.30: Results experiment of Sagaseta et al. [33]**

Although this experiment has been carried out with a relative thin slab, the absence of research into non symmetric load conditions for thick slabs makes it still usable. The experimental results show an elliptical punching cone with a clear difference in shear angle between the y-axis and x-axis. The angle for the punching cone in y-direction is approximately  $25^\circ$  (angle between bottom of slab and shear crack) while the angle in the x-direction is approximately  $45^\circ$ . The non symmetric load conditions decreased the slab capacity from

1000 kN to 875 kN, indicating a reduction of 13%. This factor of 13% fits perfectly with the approximation  $\beta$  factor introduced in the Eurocode 2. The reason for the great difference in shear crack angle is due to the slender specimen geometry. Thin slabs (with respect to the span) are more sensitive for slab deflections due to the relative low bending stiffness. Non symmetrical load conditions for slender slabs introduce unequal slab deflections in y-axis and x-axis, resulting in a different shear crack angle and a reduced slab capacity.

Contrary to the experimental specimen with a slenderness ratio of 12, the FEM specimen is with a ratio of 5 much less slender. The slab height is three times as large compared to the experimental specimen. The relative large slab thickness results in a high bending stiffness. This results in a smaller difference for the slab deflection in x-axis and y-axis. Because the deflection are less different, the shear crack angle is only slightly influenced. This is shown with the principal fracture strain development shown in Figure 6.31.

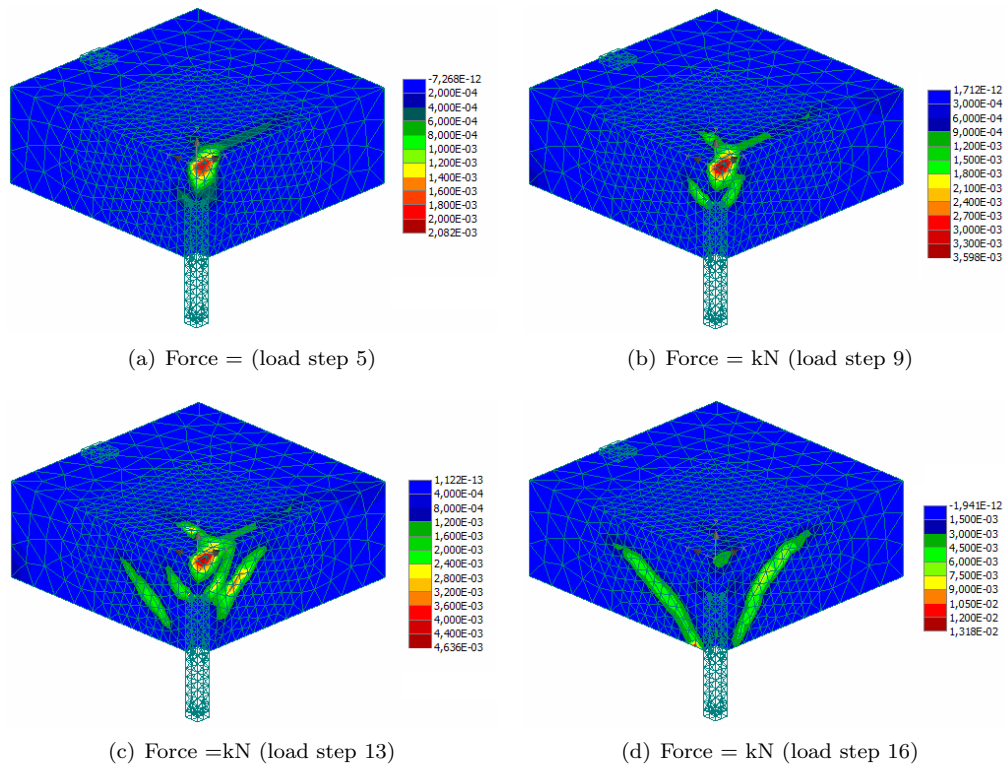


**Figure 6.31: Development of principal fracture strain with non symmetric load condition [-] ( $c = 0.7 \text{ N/mm}^2$ ,  $\mu = 1.4$ )**

During the analysis a non symmetric crack development is noticed at slab surface due to the absence of symmetrically located supporting plate, shown in Figure 6.31(b). The magnitude of the fracture strain is relatively low which indicates only micro crack development. The shear cracks shown in Figure 6.31(d) show a slight difference in crack angle. The angle in y-axis is approximately  $40^\circ$  while the angle in x-axis is approximately  $50^\circ$ . The increased shear angle in x-axis is in correspondence with the experiment. Only the magnitude of decrease is much less due to the difference in bending stiffness.

Figure 6.31 shows that a non symmetric load condition only slightly affects the punching cone perimeter with respect to symmetric conditions. This is also visible by comparing both failure loads for non symmetric and symmetric load conditions. Although the increase is less than 4%, the slab capacity increased from 5761 kN to 5984 kN corresponding to a friction coefficient of 1.6. This is against expectations, since both codes and experiments introduce a reduction factor for the slab resistance. This doesn't seem an exception since the same amount of failure load increase is noticed for the analysis with a friction coefficient of 0.2, which increased from 1235 kN to 1292 kN.

The positive influence of the non symmetric load condition on the slab capacity is caused by the extra bending moment. This introduces a slight increased compression stress distribution perpendicular to the bottom part of the pile surface. An increased compression force results in a greater shear resistance with respect to the Mohr-Coulomb law. The difference in normal stress distribution between both analyses is shown in Figure 6.32

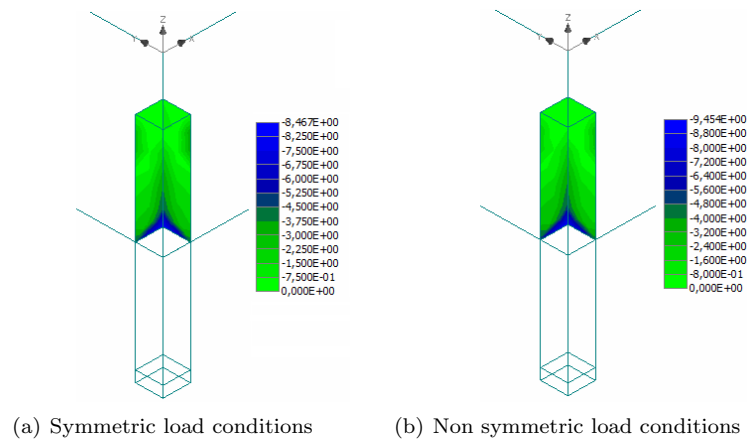


**Figure 6.32: Normal interface stress [N/mm<sup>2</sup>] ( $c = 0.7 \text{ N/mm}^2$ ,  $\mu = 0.2$ )**

The normal stress distribution increases by the addition of non symmetric load conditions. The result is a greater shear force resistance of the interface material. The slight increase of normal stress explains the relative small failure load increase of about 4%.

# Chapter 7

## Conclusion and recommendations

### 7.1 Introduction

The objective of this study was to investigate the structural behaviour with respect to punching shear of structural slabs on top of ribbed foundation piles loaded in compression. This objective includes the question which punching cone element will occur at slab failure, the small cone or the large cone.

Many three-dimensional non linear finite element analyses have been performed. The conclusions that can be drawn from the FEM analyses are summarised in the first part of this chapter. The second part consists of recommendations for future work.

### 7.2 Conclusions

The FEM analyses are able to simulate the punching shear failure mechanism with associated crack development in accordance with experimental observations. These numerical results justify the use of the interface material for modelling the contact area between the ribbed pile and structural slab for punching shear analyses. Different surface conditions of the pile can be simulated by a proper choice of friction parameters. The modelled friction parameters for the smooth and ribbed side of the pile showed good agreement with the experimental results with respect to shear crack propagation.

The FEM analyses showed after the linear stage a somewhat stiffer response than the experiments. It is believed to derive from the smeared crack formulation that is used in the concrete model. This cracking model responds with decreased stiffness to cracking first after the crack is fully developed. During the experiment, cracking affects the response of the specimen as cracks are initially formed. To overcome this difficulty, the fracture energy is reduced to decrease the stiffness of the specimen.

In the light of the validation chapter, FEM analyses are conducted for a case study. The goal of the chapter was to analyse the punching behaviour for different Mohr-Coulomb friction parameters. This friction law, which consist of a cohesion and a coefficient of friction parameter, determines the shear transfer capacity between slab and pile. From FEM analyses,

it can be concluded that the influence of the cohesion is neglectable for the punching failure mechanism. A study to the cohesion parameter is conducted for a range from 0.0 up to 1.5 N/mm<sup>2</sup> and no significantly increase of slab capacity is observed. The analyses show that the coefficient of friction parameter controls the occurring failure mechanism. Friction values from 0.0 to 1.0 show a shear crack propagation from pile head towards the slab surface. The mechanism corresponds to a relative small failure load due to the small punching cone perimeter. An active shear transfer from slab to pile is observed for friction coefficients of 1.4 or greater. This results in the most optimal shear crack propagation from slab bottom to slab surface. This latter punching cone ensures a slab capacity which is more than twice as high compared to relative small punching cone.

The FEM analyses show that the addition of bending reinforcement only slightly increases the slab capacity. This is caused by the absence of large deflection due to the high bending stiffness which is typical for slabs with a low slenderness. However, the addition of shear reinforcement is highly effective for the slab capacity. For friction coefficients of 0.0 to 1.0, an increase of roughly four times the initial failure load is observed. The failure load doubles for friction coefficients equal or greater than 1.4. A clear change in failure behaviour from brittle to ductile is noticed between a friction coefficient of 0.5 and 1.0. The brittle behaviour is characterised by a sudden failure while the ductile failure is characterised by large deflections before failure. The change in failure mode is caused by yielding of the shear reinforcement, which relates ductile material behaviour.

The analyses with non symmetric load conditions showed a slight increase of slab capacity. This increase is about 4% of the failure load for symmetric conditions. This increase is explained by the increased compression stress distribution at the contact area between pile and slab. This increase has a positive influence on the shear capacity of the interface material.

All analyses taken into account, it can be concluded that for structural slabs provided with shear reinforcement and a foundation pile with at least two ribbed sides, a fully punching cone develops.

### 7.3 Recommendations

The recommendations focus on the finite element analysis. This study has exclusively been conducted by means of non linear finite element analyses. FEM analyses are convenient and economically efficient to use compared to full scale laboratory testing that are seldom an alternative due to high costs. The performed analysis show that with a proper knowledge about finite element modelling, experiments can be simulated by numerical models.

Approximations for the Mohr-Coulomb friction parameters are based on experimental studies for indented, toothed and combed surfaces. In order to verify the friction parameters of ribbed surfaces a series of laboratory tests need to be conducted.

It is important to emphasise the need for further assessment of safety factors in order to account for proper design margins when employing results from FEM analyses in structural design. This applies especially for the investigated Mohr-Coulomb friction law parameters.

The modelled shear reinforcement bars were only used in this study to investigate the influence on the punching behaviour. Determining the number and position of the bars and the



diameter was beyond the scope of this work. The modelled reinforcement is based on practical assumptions without any variations in the amount and locations of the bars. However, a more economic design is possible when additional analyses are performed for the mentioned properties.

It is recommended to conduct more research on asymmetric load conditions. The performed FEM analyses are not extensively enough to draw clear conclusions and give recommendations for practical use.

Furthermore, long term effects such as shrinkage and creep were not included in these analyses. It is recommended to do further studies, including time dependent strength effects.



# Bibliography

- [1] ACI Committee 318. *Building code requirements for structural concrete and commentary*. ACI, London, UK, 2008.
- [2] BS Committee 318. *BS 8110 - Structural use of concrete*. BSI, Austin, USA, 1997.
- [3] P. Petersson A. Hillerborg, M. Mod er. *Analysis of crack formation and crack growth in concrete by means of fracture mechanics and finite elements*. Cement and Concrete Composite, Vol. 24, St. Louis, USA, 1976.
- [4] J. Schwartz A. Muttoni. *Behaviour of beams and punching in slabs without shear reinforcement*. IABSE Colloquium, Zurich, Switzerland, 1991.
- [5] A. Talbot. *Reinforced concrete wall footings and column footings*. University of Illinois, Illinois, USA, 1913.
- [6] J. Aziz. *Shear capacity of concrete prisms with interface joints*. Nahrain University, Baghdad, Iraq, 2010.
- [7] K. Bollinger. *Load-carrying behaviour and reinforcement of axisymmetrically loaded reinforced concrete plates*. Abteilung Bauwesen der Universitt Dortmund, Dortmund, Germany, 1956.
- [8] C. Broms. *Concrete flat slabs and footings: design method for punching and detailing for ductility*. Royal Institute of Technology, Stockholm, Sweden, 2006.
- [9] W.F. Chen. *Plasticity in reinforced concrete*. McGraw-Hill, New-York, USA, 1982.
- [10] CEN Committee. *Eurocode 2 - Design of concrete structures - Part 1-1: general rules and rules for buildings*. NEN, Brussels, Belgium, 2004.
- [11] CEN Committee. *Eurocode 2 - National annex*. NEN, Brussels, Belgium, 2004.
- [12] CUR Committee. *CUR Rapport 52: Splejsterkte van hoogwaardig beton*. CUR, Gouda, The Netherlands, 1971.
- [13] CUR Committee. *CUR Rapport 65: Pons*. CUR, Gouda, The Netherlands, 1974.
- [14] CUR Committee. *CUR Aanbeveling 77: Rekenregels voor ongewapende onderwaterbetonvloeren*. CUR, Gouda, The Netherlands, 2001.
- [15] Cervenka Consulting. *ATENA - Civil Engineering Software for Nonlinear Analysis of Reinforced Concrete*. Cervenka Consulting Ltd., Prague, Czech Republic.

- [16] A. van Rhijn C.R. Braam, A. Bosman. *Uittrekproeven op betonpalen met ribbels ingestort in een onderwaterbetonvloer*. University of Technology Delft, Delft, The Netherlands, 2004.
- [17] N. Carino D. Duthinh. *Shear design of high strength concrete beams: a review of state of the art*. National Institute of Standards and Technology, Gaithersburg, USA, 1996.
- [18] V. Lucio A. Ramos D. Faria, H. Biscaia. *Material and geometrical parameters affecting punching shear of reinforced concrete flat slabs with orthogonality reinforcement*. fib symposium, session 2B-7: Construction Technology, Prague, Czech Republic, 2011.
- [19] O. Blomkvist D. Öman. *Icke-linjär 3D finit elementanalys av genomstansade armerade betongplattor*. The Royal Institute of Technology, Stockholm, Sweden, 2006.
- [20] F. Daschner. *Deutscher Ausschuss Fur Stahlbeton: Versuche zur notwendigen Schubbe-  
wehrung zwischen Betonfertigteilen und Ortbeton*. Ernst Sohn, Berlin, Germany, 1986.
- [21] R. de Borst. *Non-linear analysis of frictional materials*. Ph.D. Thesis, Delft University of Technology, Delft, The Netherlands, 1986.
- [22] T. Engelder. *Structural Geology - Lecture 13, Coulomb Failure Criterion*. Penn State Department of Geosciences, Pennsylvania, USA, 1998.
- [23] M. Collins F. Vecchio. *Modified compression-field theory for teinforced concrete beams subjected to shear*. ACI Structural Journal, Vol. 83, Michigan, USA, 1986.
- [24] FIB. *Model Code 2010 - Final draft, Volume 1*. International Federation for Structural Concrete, Lausanne, Switzerland, 2012.
- [25] S. Guandalini. *Poinonnement symtrique des dalles en bton arm*. Ecole Polytechnique Fdrale, Lausanne, France, 2006.
- [26] M. Hallgren. *Punching shear capacity of reinforced high strength concrete slabs*. Royal Institute of Technology, Stockholm, Sweden, 1996.
- [27] D.A. Hordijk. *Local approach to fatigue of concrete*. Doctor dissertation, Delft University of Technology, Delft, The Netherlands, 1991.
- [28] A. El-Betar I. Metwally, M. Issa. *Punching shear resistance of normal and high strength reinforced concrete flat slabs*. Reinforced Concrete Research Institute, Giza, Egypt, 2008.
- [29] H. Kupfer I. Nissen, F. Daschner. *Verminderte Schubdeckung in Stahlbetonund Spann-  
betontrgern mit Fugen parallel zur Tragrichtung unter Bercksichtigung nicht vorwiegend  
ruhender Lasten*. Technische Universität München, München, Germnay, 1986.
- [30] Dywidag Systems International. *Prestressing Steel Threadbar System*. [www.dywidag-systems.com/uk](http://www.dywidag-systems.com/uk), Warwickshire, UK.
- [31] M. Meadows J. Carl, D. Müller-Hoeppe. *Comparison of tetrahedral and brick elements for linear elastic analysis*. University of Colorado Boulder, Boulder, USA, 2006.
- [32] R. Eligehausen J. Ozbolt, H. Vocke. *Three-dimensional numerical analysis of punching failure*. Royal Institute of Technology, Stockholm, Sweden, 2000.

- 
- [33] M. Ferdandez Ruiz L. Tassinari J. Sagaseta, A. Muttoni. *Non-axis-symmetrical punching shear around internal columns of RC slabs without transverse reinforcement*. Institution of Civil Engineering, 2011.
- [34] R. Faria J. Figueiras R. Gomes L. Trautwein, T. Bittencourt. *Axial symmetry analyses of punching shear in reinforced flat slabs*. University of Porto, Porto, Portugal, 2004.
- [35] K. Ka Lun Li. *Influence of size on punching shear strength of concrete slabs*. McGill University, Montreal, Canada, 2000.
- [36] B. Nylander M. Hallgren, S. Kinnunen. *Punching shear tests on column footings*. Royal Institute of Technology, Stockholm, Sweden, 1998.
- [37] P. Menetrey. *Numerical analysis of punching shear failure in reinforced concrete structures*. Ecole Polytechnique Federale de Lausanne, Lausanne, Switzerland, 1994.
- [38] J. Van Mier. *Multi-axial strain-softening of concrete part I: fracture*. RILEM, Vol. 19, Bagnex, France, 1986.
- [39] Fariborz Moeinaddini. *Concentric punching shear strength of reinforced concrete flat plates*. Swisburne University of Technology, Swisburne, Swiss, 2012.
- [40] A. Muttoni. *Shear and punching strength of slabs without shear reinforcement*. Beton- und Stahlbetonbau No.2, Berlin, Germany, 2003.
- [41] A. Muttoni. *Applications of critical shear crack theory to punching of reinforced concrete slabs without transverse reinforcement*. ACI Structural Journal, Vol. 105, Michigan, USA, 2008.
- [42] M. Nielsen. *Limit analysis and concrete plasticity*. CRC Press, Boca Raton, USA, 1998.
- [43] FIB Commission on prefabrication. *Shear at the interface of precast and in-situ concrete*. Federation Internationale de la Précontrainte, Slough, United Kingdom, 1982.
- [44] K. Willam P. Menétrey. *Triaxial failure criterion for concrete and its generalization*. ACI Structural Journal, Vol. 92, Michigan, USA, 1995.
- [45] A. de Boer R. Braam, C. van der Veen. *Trekelementen in onderwaterbetonvloeren*. Cement 2013/3 - Onderwaterbeton, Boxtel, The Netherlands, 2013.
- [46] E. Hognestad R. Elstner. *Shearing strength of reinforced concrete slabs*. ACI Structural Journal, Vol. 28, Michigan, USA, 1956.
- [47] K. Farahaninia S. Ericsson. *Punching shear in reinforced concrete slabs supported on edge steel columns*. Chalmers University of Technology, Göteborg, Sweden, 2010.
- [48] H. Nylander S. Kinnunen. *Punching shear of concrete slabs without shear reinforcement*. Royal Institute of Technology, Stockholm, Sweden, 1960.
- [49] Blijleven Sloopwerken. <http://www.blijleven.info>.
- [50] M. A. Staller. *Analytical studies and numerical analysis of punching shear failure in reinforced concrete slabs*. TRITA-BKN, Bulletin 57, 2000.
- [51] L. Jendele V. Cervenka, J. Cervenka. *ATENA Program Documentation - Theory*. Cervenka Consulting Ltd., Prague, Czech Republic, 2011.

## Bibliography

---

- [52] J. Walraven. *Fundamental analysis of aggregate interlock*. Delft University Press, Delft, The Netherlands, 1980.
- [53] J. Walraven. *CIE3150 - Gewapend Beton*. Delft University of Technology, Delft, The Netherlands, 2011.
- [54] Winvast. <http://www.winvast.nl>.
- [55] J. Wood. *Quantitative study of the causes of the partial collapse on 20th March 1997*. Structural Studies & Design Ltd, Chiddingfold, United Kingdom, 2006.
- [56] Z. Cao Z. Bažant. *Size effect in punching shear failure of slabs*. ACI Structural Journal, Vol. 84, Michigan, USA, 1987.

# Appendices





## Appendix A

# ATENA Input - Validation Chapter



Description:	<b>Simulation experiment Braam et al.</b>	Unit system:	Metric
Note:	Punching shear experiment Specimen 1-1		

side  
1

## ANALYSIS INFORMATION

Property	Value
Description	Simulation experiment Braam et al.
Note	Punching shear experiment Specimen 1-1
Unit system	Metric
Solver type	standard
Run	geometrically nonlinear

## MATERIALS

MATERIAL 1	
Property	Value
Title	Foundation Pile
Type	CC3DNonLinCementitious2
Elastic modulus E [MPa]	3,800E+04
Poisson's ratio $\mu$ [-]	0,200
Specific material weight $\rho$ [MN/m <sup>3</sup> ]	2,300E-02
Coefficient of thermal expansion $\alpha$ [1/K]	1,200E-05
Tensile strength $F_t$ [MPa]	4,200E+00
Compressive strength $F_c$ [MPa]	-6,300E+01
Specific fracture energy $G_f$ [MN/m]	1,386E-04
Critical compressive displacement $W_d$ [m]	-5,000E-04
Exc.,def. the shape of fail.surface e [-]	0,520
Multiplier for the direction of the pl.flow $\beta$ [-]	0,000
Fixed crack model coefficient [-]	1,000
Plastic strain at compressive strength $\varepsilon_{cp}$ [-]	-8,420E-04
Onset of non-linear behavior in compression $F_{c0}$ [MPa]	-8,820E+00
Reduction of compressive strength due to cracks $r_{c,lim}$ [-]	0,2
Crack Shear Stiff. Factor $S_F$ [-]	20,0
Aggregate Size [m]	0,02

MATERIAL 2	
Property	Value
Title	Slab
Type	CC3DNonLinCementitious2
Elastic modulus E [MPa]	3,285E+04
Poisson's ratio $\mu$ [-]	0,200
Specific material weight $\rho$ [MN/m <sup>3</sup> ]	2,300E-02
Coefficient of thermal expansion $\alpha$ [1/K]	1,200E-05
Tensile strength $F_t$ [MPa]	2,900E+00
Compressive strength $F_c$ [MPa]	-3,805E+01
Specific fracture energy $G_f$ [MN/m]	3,000E-05
Critical compressive displacement $W_d$ [m]	-5,000E-04
Exc.,def. the shape of fail.surface e [-]	0,520
Multiplier for the direction of the pl.flow $\beta$ [-]	0,000
Fixed crack model coefficient [-]	0,500
Plastic strain at compressive strength $\varepsilon_{cp}$ [-]	-1,158E-03



Description:	<b>Simulation experiment Braam et al.</b>	Unit system:	Metric
Note:	Punching shear experiment Specimen 1-1		

side  
2

MATERIAL 2	
Property	Value
Onset of non-linear behavior in compression $F_{c0}$ [MPa]	-6,090E+00
Reduction of compressive strength due to cracks $r_{c,lim}$ [-]	0,2
Crack Shear Stiff. Factor $S_F$ [-]	20,0
Aggregate Size [m]	0,02

MATERIAL 3	
Property	Value
Title	Prestressing Cable
Type	CCReinforcement
Elastic modulus E [MPa]	1,948E+05
Specific material weight $\rho$ [MN/m <sup>3</sup> ]	7,850E-02
Coefficient of thermal expansion $\alpha$ [1/K]	1,200E-05
Reinf. type	Bilinear
$\sigma_y$ [MPa]	950,000
In compression	active

MATERIAL 4	
Property	Value
Title	Ribbed Side
Type	CC3DInterface
Normal stiffness $K_{nn}$ [MN/m <sup>3</sup> ]	3,285E+08
Tangential stiffness $K_{tt}$ [MN/m <sup>3</sup> ]	3,285E+08
Tensile strength $F_t$ [MPa]	0,000E+00
Cohesion C [MPa]	6,600E-01
Friction coefficient [-]	9,000E-01
Min.normal stiffness for num.purposes $K_{nn,min}$ [MN/m <sup>3</sup> ]	3,285E+05
Min.tangential stiffness for num.purposes $K_{tt,min}$ [MN/m <sup>3</sup> ]	3,285E+05

MATERIAL 5	
Property	Value
Title	Smooth Side
Type	CC3DInterface
Normal stiffness $K_{nn}$ [MN/m <sup>3</sup> ]	3,285E+08
Tangential stiffness $K_{tt}$ [MN/m <sup>3</sup> ]	3,285E+08
Tensile strength $F_t$ [MPa]	0,000E+00
Cohesion C [MPa]	2,700E-01
Friction coefficient [-]	6,000E-01
Min.normal stiffness for num.purposes $K_{nn,min}$ [MN/m <sup>3</sup> ]	3,285E+05
Min.tangential stiffness for num.purposes $K_{tt,min}$ [MN/m <sup>3</sup> ]	3,285E+05

MATERIAL 6	
Property	Value
Title	Steel Plate
Type	CC3DElastIsotropic
Elastic modulus E [MPa]	2,100E+05



Description:	<b>Simulation experiment Braam et al.</b>	Unit system:	Metric
Note:	Punching shear experiment Specimen 1-1		

side  
3

MATERIAL 6	
Property	Value
Poisson's ratio $\mu$ [-]	0,300
Specific material weight $\rho$ [MN/m <sup>3</sup> ]	2,300E-02
Coefficient of thermal expansion $\alpha$ [1/K]	1,200E-05

## MACRO-ELEMENTS

### MACROELEMENT 1

MACROELEMENT 1 - JOINTS			
Number	X [m]	Y [m]	Z [m]
1	0,0000	0,1250	0,0000
2	0,0000	1,7250	0,0000
3	1,7250	1,7250	0,0000
4	1,7250	0,0000	0,0000
5	0,1250	0,0000	0,0000
6	0,1250	0,1250	0,0000
7	0,0000	1,7250	-0,8200
8	1,7250	1,7250	-0,8200
9	1,7250	0,0000	-0,8200
10	1,3000	1,3000	-0,8200
11	0,0000	1,3000	-0,8200
12	1,3000	0,0000	-0,8200
13	1,3000	0,0000	-0,5000
14	1,3000	1,3000	-0,5000
15	0,0000	1,3000	-0,5000
16	0,1250	0,1250	-0,5000
17	0,0000	0,1250	-0,5000
18	0,1250	0,0000	-0,5000
22	0,8500	0,0000	0,0000
23	0,8500	0,8500	0,0000
29	0,0000	0,8500	0,0000

MAKROELEMENT 1 - LINES					
Number	Joint at the beg.	Joint at the end	Number	Joint at the beg.	Joint at the end
1	29	2	18	10	12
2	2	3	19	11	15
3	3	4	20	15	17
4	4	22	21	17	16
5	6	5	22	16	18
6	4	9	23	17	1
7	1	6	24	6	16
8	9	8	25	13	14
9	8	3	26	29	17
10	8	7	27	14	15
11	7	2	28	22	18
12	9	12	29	14	10
13	12	13	32	22	5
14	13	18	33	1	29
15	18	5	36	29	23
16	7	11	46	23	22
17	11	10			



Description:	<b>Simulation experiment Braam et al.</b>	Unit system:	Metric
Note:	Punching shear experiment Specimen 1-1		

side  
4

### MAKROELEMENT 1 - SURFACES

Number	List of boundary lines
1	3,6,8-9
2	2,9-11
3	8,10,12,16-18
4	4,6,12-14,28
5	1,11,16,19-20,26
6	23,26,33
7	5,15,22,24
8	14,20-22,25,27
9	7,21,23-24
10	17,19,27,29
11	13,18,25,29
12	15,28,32
13	5,7,32-33,36,46
14	1-4,36,46

### MACROELEMENT 1 - PROPERTIES

Type of macroelement standard, azimuth = 0,00°, zenith = 0,00°

CS	Used	Material			
1	Yes	Ident	Material	Ratio [%]	Direction
		Basic	Slab		

### MACROELEMENT 2

#### MACROELEMENT 2 - JOINTS

Number	X [m]	Y [m]	Z [m]
1	0,0000	0,0000	0,0000
6	0,1250	0,0000	0,0000
7	0,1250	0,1250	0,0000
8	0,0000	0,1250	0,0000
9	0,1250	0,1250	-0,6000
10	0,0000	0,1250	-0,6000
11	0,1250	0,0000	-0,6000
12	0,0000	0,0000	-0,6000

#### MAKROELEMENT 2 - LINES

Number	Joint at the beg.	Joint at the end	Number	Joint at the beg.	Joint at the end
1	10	9	10	8	7
5	9	11	11	1	6
6	8	1	13	8	10
7	11	12	16	12	1
8	6	7	17	6	11
9	12	10	20	9	7

### MAKROELEMENT 2 - SURFACES

Number	List of boundary lines
1	1,5,7,9
2	1,10,13,20
3	5,8,17,20
5	6,9,13,16
9	7,11,16-17
10	6,8,10-11



Description:	<b>Simulation experiment Braam et al.</b>	Unit system:	Metric
Note:	Punching shear experiment Specimen 1-1		

side  
5

### MACROELEMENT 2 - PROPERTIES

Type of macroelement standard, azimuth = 0,00°, zenith = 0,00°

CS	Used	Material			
1	Yes	Ident	Material	Ratio [%]	Direction
		Basic	Foundation Pile		

### MACROELEMENT 3

#### MACROELEMENT 3 - JOINTS

Number	X [m]	Y [m]	Z [m]
1	0,0000	0,0000	-0,6000
2	0,1250	0,1250	-0,6000
3	0,0000	0,1250	-0,6000
4	0,1250	0,0000	-0,6000
5	0,0000	0,0000	-0,6500
6	0,1250	0,1250	-0,6500
7	0,0000	0,1250	-0,6500
8	0,1250	0,0000	-0,6500

#### MAKROELEMENT 3 - LINES

Number	Joint at the beg.	Joint at the end	Number	Joint at the beg.	Joint at the end
1	7	6	7	1	4
2	6	8	8	4	2
3	8	5	9	2	3
4	5	7	10	6	2
5	7	3	11	4	8
6	3	1	12	1	5

#### MAKROELEMENT 3 - SURFACES

Number	List of boundary lines
1	1,5,9-10
2	2,8,10-11
3	1-4
4	4-6,12
5	3,7,11-12
6	6-9

### MACROELEMENT 3 - PROPERTIES


Type of macroelement standard, azimuth = 0,00°, zenith = 0,00°

CS	Used	Material			
1	Yes	Ident	Material	Ratio [%]	Direction
		Basic	Steel Plate		

### MACROELEMENT 4

#### MACROELEMENT 4 - JOINTS

Number	X [m]	Y [m]	Z [m]
1	0,8500	0,8500	0,0000
2	1,1500	0,8500	0,0000
3	0,8500	1,1500	0,0000
4	1,1500	1,1500	0,0000
5	1,1500	1,1500	0,0500
6	0,8500	1,1500	0,0500
7	0,8500	0,8500	0,0500

	Description:	<b>Simulation experiment Braam et al.</b>	Unit system:	Metric	<b>side 6</b>
	Note:	Punching shear experiment Specimen 1-1			

MACROELEMENT 4 - JOINTS			
Number	X [m]	Y [m]	Z [m]
8	1,1500	0,8500	0,0500

MAKROELEMENT 4 - LINES					
Number	Joint at the beg.	Joint at the end	Number	Joint at the beg.	Joint at the end
1	1	2	7	8	5
2	2	4	8	5	6
3	4	3	9	6	3
4	3	1	10	5	4
5	1	7	11	8	2
6	7	8	12	7	6

MAKROELEMENT 4 - SURFACES	
Number	List of boundary lines
1	1-4
2	3,8-10
3	2,7,10-11
4	1,5-6,11
5	4-5,9,12
6	6-8,12

MACROELEMENT 4 - PROPERTIES				
Type of macroelement standard, azimuth = 0,00°, zenith = 0,00°				
CS	Used	Material	Ratio [%]	Direction
1	Yes	Ident Basic	Material Steel Plate	Ratio [%] Direction

## CONTACTS

CONTACTS - TOPOLOGY			
Number	Macroelement A - surface	Macroelement B - surface	Preferred master
1	1/9	2/2	automatic
2	2/3	1/7	automatic
3	3/6	2/1	automatic
4	4/1	1/14	automatic

CONTACT 1 - PROPERTIES			
CS	Used	Contact	Material
1	Yes	contact element - GAP	Smooth Side


CONTACT 2 - PROPERTIES			
CS	Used	Contact	Material
1	Yes	contact element - GAP	Ribbed Side

CONTACT 3 - PROPERTIES			
CS	Used	Contact	Material
1	Yes	perfect connection	

CONTACT 4 - PROPERTIES			
CS	Used	Contact	Material
1	Yes	perfect connection	

## BAR REINFORCEMENT

### BAR REINFORCEMENT 1

	Description:	<b>Simulation experiment Braam et al.</b>	Unit system:	Metric	<b>side 7</b>
	Note:	Punching shear experiment Specimen 1-1			

BAR REINFORCEMENT 1 - POINTS				
Number	X [m]	Y [m]	Z [m]	
1	0,9000	0,0000	-0,3500	
2	0,9000	1,7250	-0,3500	

BAR REINFORCEMENT 1 - SEGMENTS					
Number	Start point	End point	Number	Start point	End point
1	1	2			

BAR REINFORCEMENT 1 - PROPERTIES					
CS	Used	Material	Area [m <sup>2</sup> ]	Bond with surrounding material	
1	Yes	Prestressing Cable	8,042E-04	Connection type	perfect connection

### BAR REINFORCEMENT 2

BAR REINFORCEMENT 2 - POINTS				
Number	X [m]	Y [m]	Z [m]	
1	1,2000	0,0000	-0,3500	
2	1,2000	1,7250	-0,3500	

BAR REINFORCEMENT 2 - SEGMENTS					
Number	Start point	End point	Number	Start point	End point
1	1	2			

BAR REINFORCEMENT 2 - PROPERTIES					
CS	Used	Material	Area [m <sup>2</sup> ]	Bond with surrounding material	
1	Yes	Prestressing Cable	8,042E-04	Connection type	perfect connection

### BAR REINFORCEMENT 3

BAR REINFORCEMENT 3 - POINTS				
Number	X [m]	Y [m]	Z [m]	
1	1,5000	0,0000	-0,3500	
2	1,5000	1,7250	-0,3500	

BAR REINFORCEMENT 3 - SEGMENTS					
Number	Start point	End point	Number	Start point	End point
1	1	2			

BAR REINFORCEMENT 3 - PROPERTIES					
CS	Used	Material	Area [m <sup>2</sup> ]	Bond with surrounding material	
1	Yes	Prestressing Cable	8,042E-04	Connection type	perfect connection


### BAR REINFORCEMENT 4

BAR REINFORCEMENT 4 - POINTS				
Number	X [m]	Y [m]	Z [m]	
1	0,0000	1,2000	-0,2900	
2	1,7250	1,2000	-0,2900	

BAR REINFORCEMENT 4 - SEGMENTS					
Number	Start point	End point	Number	Start point	End point
1	1	2			

BAR REINFORCEMENT 4 - PROPERTIES					
CS	Used	Material	Area [m <sup>2</sup> ]	Bond with surrounding material	
1	Yes	Prestressing Cable	8,042E-04	Connection type	perfect connection



	Description:	<b>Simulation experiment Braam et al.</b>	Unit system:	Metric	<b>side 8</b>
	Note:	Punching shear experiment Specimen 1-1			

## BAR REINFORCEMENT 5

BAR REINFORCEMENT 5 - POINTS			
Number	X [m]	Y [m]	Z [m]
1	0,0000	0,9000	-0,2900
2	1,7250	0,9000	-0,2900

BAR REINFORCEMENT 5 - SEGMENTS					
Number	Start point	End point	Number	Start point	End point
1	1	2			

BAR REINFORCEMENT 5 - PROPERTIES					
CS	Used	Material	Area [m <sup>2</sup> ]	Bond with surrounding material	
1	Yes	Prestressing Cable	8,042E-04	Connection type	perfect connection

## BAR REINFORCEMENT 6

BAR REINFORCEMENT 6 - POINTS			
Number	X [m]	Y [m]	Z [m]
1	0,0000	1,5000	-0,2900
2	1,7250	1,5000	-0,2900

BAR REINFORCEMENT 6 - SEGMENTS					
Number	Start point	End point	Number	Start point	End point
1	1	2			

BAR REINFORCEMENT 6 - PROPERTIES					
CS	Used	Material	Area [m <sup>2</sup> ]	Bond with surrounding material	
1	Yes	Prestressing Cable	8,042E-04	Connection type	perfect connection

## LOAD CASES - OVERVIEW

LOAD CASE LIST			
Number	Title	Code	Coeff.[-]
1	Own Weight	Body force	1,000
2	Supports - LC 2	Supports	
3	Prescribed deformation - LC 3	Prescribed deformation	1,000
4	Pre-stressing - LC 4	Pre-stressing	1,000

## LC 1 - OWN WEIGHT

BODY FORCE
Dir: (0,0000; 0,0000; -1,0000)
Macroelements:
Reinforcement bars:
External cables:

## LC 2 - SUPPORTS - LC 2

SURFACE SUPPORTS				
Macro. / surface	Coordinate system	Support in dir. of the axis		
		X	Y	Z
1/4	Global	free	fixed	free
1/5	Global	fixed	free	free
1/6	Global	fixed	free	free
1/12	Global	free	fixed	free
2/5	Global	fixed	free	free



Description:	<b>Simulation experiment Braam et al.</b>	Unit system:	Metric
Note:	Punching shear experiment Specimen 1-1		

side  
9

### SURFACE SUPPORTS

Macro. / surface	Coordinate system	Support in dir. of the axis		
		X	Y	Z
2/9	Global	free	fixed	free
3/4	Global	fixed	free	free
3/5	Global	free	fixed	free
4/6	Global	free	free	fixed

## LC 3 - PRESCRIBED DEFORMATION - LC 3

### SUPPORTS AND PRESCRIBED DEFORMATIONS OF JOINTS

Macro. / joint	Coordinate system	Support and deformation in the direction of the axis		
		X [m]	Y [m]	Z [m]
3/5	Global	free	free	fixed: 5,000E-04

## LC 4 - PRE-STRESSING - LC 4

### PRE-STRESSING OF DISCRETE REINF.

Disc. reinf.	Value [MN]
1	4,530E-01
2	4,530E-01
3	4,530E-01
4	4,530E-01
5	4,530E-01
6	4,530E-01

## SOLUTION PARAMETERS

### SOLUTION PARAMETERS 1

Property	Value
Title	Standard Newton-Raphson
Method	Newton-Raphson (line search)
Iteration limit	40
Displacement Error	0,010000
Residual Error	0,010000
Absolute Residual Error	0,010000
Energy Error	0,000100
Optimize band-width	Sloan
Line Search	Yes
LS Type	With iterations
LS Unbalanced energy limit	0,800
LS Line search iteration limit	2
LS Minimum Eta	0,010
LS Maximum Eta	1,000
Update Stiffness	Each iteration
Stiffness Type	Tangent
Immediate Displacement Error Multiple	10000,0
After Step Displacement Error Multiple	1000,0
Immediate Residual Error Multiple	10000,0
After Step Residual Error Multiple	1000,0
Immediate Absolute Residual Error Multiple	10000,0
After Step Absolute Residual Error Multiple	1000,0
Immediate Energy Error Multiple	1000000,0



Description:	<b>Simulation experiment Braam et al.</b>	Unit system:	Metric
Note:	Punching shear experiment Specimen 1-1		

SOLUTION PARAMETERS 1	
Property	Value
After Step Energy Error Multiple	10000,0

SOLUTION PARAMETERS 2	
Property	Value
Title	Standard Arc Length
Method	Arc length (line search)
Arc Length Method	Consistently linearised
A-L Adjustment Method	Constant
A-L Load-Displacement Ratio	0,200
A-L Load-Displacement Method	Bergan constant
A-L Reference number of iterations	10
A-L Step-Length	Based on current load step
A-L Location	All nodes
Iteration limit	40
Displacement Error	0,010000
Residual Error	0,010000
Absolute Residual Error	0,010000
Energy Error	0,000100
Optimize band-width	Sloan
Line Search	Yes
LS Type	With iterations
LS Unbalanced energy limit	0,800
LS Line search iteration limit	2
LS Minimum Eta	0,010
LS Maximum Eta	1,000
Update Stiffness	Each iteration
Stiffness Type	Tangent
Immediate Displacement Error Multiple	10000,0
After Step Displacement Error Multiple	1000,0
Immediate Residual Error Multiple	10000,0
After Step Residual Error Multiple	1000,0
Immediate Absolute Residual Error Multiple	10000,0
After Step Absolute Residual Error Multiple	1000,0
Immediate Energy Error Multiple	1000000,0
After Step Energy Error Multiple	10000,0

SOLUTION PARAMETERS 3	
Property	Value
Title	Analysis parameter 3
Method	Newton-Raphson
Iteration limit	30
Displacement Error	0,010000
Residual Error	0,010000
Absolute Residual Error	0,010000
Energy Error	0,000100
Optimize band-width	Sloan
Line Search	No
Update Stiffness	Each iteration
Stiffness Type	Elastic
Immediate Displacement Error Multiple	200,0
After Step Displacement Error Multiple	50,0



Description:  
Note:

**Simulation experiment Braam et al.**

Unit system:

Metric

Punching shear experiment Specimen 1-1

side  
11

### SOLUTION PARAMETERS 3


Property	Value
Immediate Residual Error Multiple	200,0
After Step Residual Error Multiple	50,0
Immediate Absolute Residual Error Multiple	200,0
After Step Absolute Residual Error Multiple	50,0
Immediate Energy Error Multiple	200,0
After Step Energy Error Multiple	50,0

### ANALYSIS STEPS

Number	Load cases	Phase	Solution Parameters	Coefficient [-]
1	2,4	(1) Phase 1	Standard Newton-Raphson	1,000
2	1-3	(1) Phase 1	Standard Newton-Raphson	1,000
3	1-3	(1) Phase 1	Standard Newton-Raphson	1,000
4	1-3	(1) Phase 1	Standard Newton-Raphson	1,000
5	1-3	(1) Phase 1	Standard Newton-Raphson	1,000
6	1-3	(1) Phase 1	Standard Newton-Raphson	1,000
7	1-3	(1) Phase 1	Standard Newton-Raphson	1,000
8	1-3	(1) Phase 1	Standard Newton-Raphson	1,000
9	1-3	(1) Phase 1	Standard Newton-Raphson	1,000
10	1-3	(1) Phase 1	Standard Newton-Raphson	1,000
11	1-3	(1) Phase 1	Standard Newton-Raphson	1,000
12	1-3	(1) Phase 1	Standard Newton-Raphson	1,000
13	1-3	(1) Phase 1	Standard Newton-Raphson	1,000
14	1-3	(1) Phase 1	Standard Newton-Raphson	1,000
15	1-3	(1) Phase 1	Standard Newton-Raphson	1,000
16	1-3	(1) Phase 1	Standard Newton-Raphson	1,000
17	1-3	(1) Phase 1	Standard Newton-Raphson	1,000
18	1-3	(1) Phase 1	Standard Newton-Raphson	1,000
19	1-3	(1) Phase 1	Standard Newton-Raphson	1,000
20	1-3	(1) Phase 1	Standard Newton-Raphson	1,000
21	1-3	(1) Phase 1	Standard Newton-Raphson	1,000
22	1-3	(1) Phase 1	Standard Newton-Raphson	1,000
23	1-3	(1) Phase 1	Standard Newton-Raphson	1,000
24	1-3	(1) Phase 1	Standard Newton-Raphson	1,000
25	1-3	(1) Phase 1	Standard Newton-Raphson	1,000
26	1-3	(1) Phase 1	Standard Newton-Raphson	1,000
27	1-3	(1) Phase 1	Standard Newton-Raphson	1,000
28	1-3	(1) Phase 1	Standard Newton-Raphson	1,000
29	1-3	(1) Phase 1	Standard Newton-Raphson	1,000

### MONITORING POINTS

Number	Title	Type Location	Quantity - item
1	Force	Value at node Macroelement 3, point (0,0000; 0,0000; -0,6500) [m]	Reactions - Component 3
2	Meetpunt 2	Value at node Macroelement 2, point (0,0600; 0,0400; 0,0000) [m]	Displacements - Component 3

	Description:	<b>Simulation experiment Braam et al.</b>	Unit system:	Metric	<b>side 12</b>
	Note:	Punching shear experiment Specimen 1-1			

Number	Title	Type Location	Quantity - item
3	Meetpunt 3	Value at node Macroelement 1, point (0,1750; 0,0400; 0,0000) [m]	Displacements - Component 3
4	Meetpunt 4	Value at node Macroelement 1, point (0,3810; 0,0400; 0,0000) [m]	Displacements - Component 3
5	Meetpunt 5	Value at node Macroelement 1, point (0,5870; 0,0400; 0,0000) [m]	Displacements - Component 3
6	Meetpunt 6	Value at node Macroelement 1, point (0,1750; 0,1120; 0,0000) [m]	Displacements - Component 3
7	Meetpunt 7	Value at node Macroelement 1, point (0,3810; 0,3250; 0,0000) [m]	Displacements - Component 3
8	Meetpunt 8	Value at node Macroelement 1, point (0,5870; 0,5300; 0,0000) [m]	Displacements - Component 3



Description:	<b>Simulation experiment Braam et al.</b>	Unit system:	Metric
Note:	Punching shear experiment Specimen 3-1		

side  
1


## ANALYSIS INFORMATION

Property	Value
Description	Simulation experiment Braam et al.
Note	Punching shear experiment Specimen 3-1
Unit system	Metric
Solver type	standard
Run	geometrically nonlinear

## MATERIALS

MATERIAL 1	
Property	Value
Title	Foundation Pile
Type	CC3DNonLinCementitious2
Elastic modulus E [MPa]	3,800E+04
Poisson's ratio $\mu$ [-]	0,200
Specific material weight $\rho$ [MN/m <sup>3</sup> ]	2,300E-02
Coefficient of thermal expansion $\alpha$ [1/K]	1,200E-05
Tensile strength $F_t$ [MPa]	4,200E+00
Compressive strength $F_c$ [MPa]	-6,300E+01
Specific fracture energy $G_f$ [MN/m]	1,386E-04
Critical compressive displacement $W_d$ [m]	-5,000E-04
Exc.,def. the shape of fail.surface e [-]	0,520
Multiplier for the direction of the pl.flow $\beta$ [-]	0,000
Fixed crack model coefficient [-]	1,000
Plastic strain at compressive strength $\varepsilon_{cp}$ [-]	-8,420E-04
Onset of non-linear behavior in compression $F_{c0}$ [MPa]	-8,820E+00
Reduction of compressive strength due to cracks $r_{c,lim}$ [-]	0,2
Crack Shear Stiff. Factor $S_F$ [-]	20,0
Aggregate Size [m]	0,02

MATERIAL 2	
Property	Value
Title	Slab
Type	CC3DNonLinCementitious2
Elastic modulus E [MPa]	3,035E+04
Poisson's ratio $\mu$ [-]	0,200
Specific material weight $\rho$ [MN/m <sup>3</sup> ]	2,300E-02
Coefficient of thermal expansion $\alpha$ [1/K]	1,200E-05
Tensile strength $F_t$ [MPa]	2,300E+00
Compressive strength $F_c$ [MPa]	-2,922E+01
Specific fracture energy $G_f$ [MN/m]	2,875E-05
Critical compressive displacement $W_d$ [m]	-5,000E-04
Exc.,def. the shape of fail.surface e [-]	0,520
Multiplier for the direction of the pl.flow $\beta$ [-]	0,000
Fixed crack model coefficient [-]	0,700
Plastic strain at compressive strength $\varepsilon_{cp}$ [-]	-1,067E-03

	Description:	<b>Simulation experiment Braam et al.</b>	Unit system:	Metric	<b>side 2</b>
	Note:	Punching shear experiment Specimen 3-1			


MATERIAL 2	
Property	Value
Onset of non-linear behavior in compression $F_{c0}$ [MPa]	-4,830E+00
Reduction of compressive strength due to cracks $r_{c,lim}$ [-]	0,2
Crack Shear Stiff. Factor $S_F$ [-]	20,0
Aggregate Size [m]	0,02

MATERIAL 3	
Property	Value
Title	Prestressing Cable
Type	CCReinforcement
Elastic modulus E [MPa]	1,948E+05
Specific material weight $\rho$ [MN/m <sup>3</sup> ]	7,850E-02
Coefficient of thermal expansion $\alpha$ [1/K]	1,200E-05
Reinf. type	Bilinear
$\sigma_y$ [MPa]	950,000
In compression	active

MATERIAL 4	
Property	Value
Title	Ribbed Side
Type	CC3DInterface
Normal stiffness $K_{nn}$ [MN/m <sup>3</sup> ]	3,285E+08
Tangential stiffness $K_{tt}$ [MN/m <sup>3</sup> ]	3,285E+08
Tensile strength $F_t$ [MPa]	0,000E+00
Cohesion C [MPa]	6,600E-01
Friction coefficient [-]	9,000E-01
Min.normal stiffness for num.purposes $K_{nn,min}$ [MN/m <sup>3</sup> ]	3,285E+05
Min.tangential stiffness for num.purposes $K_{tt,min}$ [MN/m <sup>3</sup> ]	3,285E+05

MATERIAL 5	
Property	Value
Title	Smooth Side
Type	CC3DInterface
Normal stiffness $K_{nn}$ [MN/m <sup>3</sup> ]	3,285E+08
Tangential stiffness $K_{tt}$ [MN/m <sup>3</sup> ]	3,285E+08
Tensile strength $F_t$ [MPa]	0,000E+00
Cohesion C [MPa]	2,700E-01
Friction coefficient [-]	6,000E-01
Min.normal stiffness for num.purposes $K_{nn,min}$ [MN/m <sup>3</sup> ]	3,285E+05
Min.tangential stiffness for num.purposes $K_{tt,min}$ [MN/m <sup>3</sup> ]	3,285E+05

MATERIAL 6	
Property	Value
Title	Steel Plate
Type	CC3DElastIsotropic
Elastic modulus E [MPa]	2,100E+05

	Description:	<b>Simulation experiment Braam et al.</b>	Unit system:	Metric	side 3
	Note:	Punching shear experiment Specimen 3-1			

MATERIAL 6	
Property	Value
Poisson's ratio $\mu$ [-]	0,300
Specific material weight $\rho$ [MN/m <sup>3</sup> ]	2,300E-02
Coefficient of thermal expansion $\alpha$ [1/K]	1,200E-05



## Appendix B

# ATENA Input - Case Study



Description:	<b>Case Study, Unreinforced Slab</b>	Unit system:	Metric
Note:	Cohesion = 1.0, Friction coefficient = 1.0		

side  
1

## ANALYSIS INFORMATION


Property	Value
Description	Case Study, Unreinforced Slab
Note	Cohesion = 1.0, Friction coefficient = 1.0
Unit system	Metric
Solver type	standard
Run	geometrically nonlinear

## MATERIALS

MATERIAL 1	
Property	Value
Title	Elastic Pile
Type	CC3DElastIsotropic
Elastic modulus E [MPa]	3,800E+04
Poisson's ratio $\mu$ [-]	0,200
Specific material weight $\rho$ [MN/m <sup>3</sup> ]	2,300E-02
Coefficient of thermal expansion $\alpha$ [1/K]	1,200E-05

MATERIAL 2	
Property	Value
Title	Concrete Slab
Type	CC3DNonLinCementitious2
Elastic modulus E [MPa]	3,285E+04
Poisson's ratio $\mu$ [-]	0,200
Specific material weight $\rho$ [MN/m <sup>3</sup> ]	2,300E-02
Coefficient of thermal expansion $\alpha$ [1/K]	1,200E-05
Tensile strength $F_t$ [MPa]	2,900E+00
Compressive strength $F_c$ [MPa]	-3,810E+01
Specific fracture energy $G_f$ [MN/m]	2,875E-05
Critical compressive displacement $W_d$ [m]	-5,000E-04
Exc.,def. the shape of fail.surface e [-]	0,520
Multiplier for the direction of the pl.flow $\beta$ [-]	0,000
Fixed crack model coefficient [-]	0,700
Plastic strain at compressive strength $\epsilon_{cp}$ [-]	-1,158E-03
Onset of non-linear behavior in compression $F_{c0}$ [MPa]	-6,090E+00
Reduction of compressive strength due to cracks $r_{c,lim}$ [-]	0,2
Crack Shear Stiff. Factor $S_F$ [-]	20,0
Aggregate Size [m]	0,02

MATERIAL 3	
Property	Value
Title	Steel Plate
Type	CC3DElastIsotropic
Elastic modulus E [MPa]	2,100E+06
Poisson's ratio $\mu$ [-]	0,300
Specific material weight $\rho$ [MN/m <sup>3</sup> ]	7,600E-02
Coefficient of thermal expansion $\alpha$ [1/K]	1,200E-05

	Description:	<b>Case Study, Unreinforced Slab</b>	Unit system:	Metric	<b>side 2</b>
	Note:	Cohesion = 1.0, Friction coefficient = 1.0			

MATERIAL 4	
Property	Value
Title	Interface
Type	CC3DInterface
Normal stiffness $K_{nn}$ [MN/m <sup>3</sup> ]	3,800E+06
Tangential stiffness $K_{tt}$ [MN/m <sup>3</sup> ]	3,800E+06
Tensile strength $F_t$ [MPa]	0,000E+00
Cohesion C [MPa]	1,000E+00
Friction coefficient [-]	1,000E+00
Min.normal stiffness for num.purposes $K_{nn,min}$ [MN/m <sup>3</sup> ]	3,800E+04
Min.tangential stiffness for num.purposes $K_{tt,min}$ [MN/m <sup>3</sup> ]	3,800E+04

MATERIAL 6	
Property	Value
Title	Reinforcement
Type	CCReinforcement
Elastic modulus E [MPa]	2,000E+05
Specific material weight $\rho$ [MN/m <sup>3</sup> ]	7,850E-02
Coefficient of thermal expansion $\alpha$ [1/K]	1,200E-05
Reinf. type	Linear
In compression	active

## MACRO-ELEMENTS

### MACROELEMENT 1

MACROELEMENT 1 - JOINTS				
Number	X [m]	Y [m]	Z [m]	
1	0,0000	0,0000	0,0000	0,0000
2	0,0000	2,0000	0,0000	0,0000
3	2,0000	2,0000	0,0000	0,0000
4	2,0000	0,0000	0,0000	0,0000
5	2,0000	0,0000	0,0000	-0,8000
6	2,0000	2,0000	0,0000	-0,8000
7	0,0000	2,0000	0,0000	-0,8000
8	0,1250	0,0000	0,0000	-0,8000
9	0,1250	0,1250	0,0000	-0,8000
10	0,0000	0,1250	0,0000	-0,8000
11	0,0000	0,1250	0,0000	-0,3000
12	0,1250	0,1250	0,0000	-0,3000
13	0,1250	0,0000	0,0000	-0,3000
14	0,0000	0,0000	0,0000	-0,3000
15	0,4000	0,0000	0,0000	-0,8000
16	0,0000	0,4000	0,0000	-0,8000
22	1,2000	0,0000	0,0000	0,0000
23	1,2000	1,2000	0,0000	0,0000
29	0,0000	1,2000	0,0000	0,0000

MAKROELEMENT 1 - LINES					
Number	Joint at the beg.	Joint at the end	Number	Joint at the beg.	Joint at the end
1	29	2	16	13	8



Description:  
Note:

**Case Study, Unreinforced Slab**  
Cohesion = 1.0, Friction coefficient = 1.0

Unit system:

Metric

side  
3

### MAKROELEMENT 1 - LINES

Number	Joint at the beg.	Joint at the end	Number	Joint at the beg.	Joint at the end
2	2	3	17	15	5
3	3	4	18	13	14
4	4	22	19	14	11
5	6	5	20	14	1
6	5	4	21	8	9
7	6	3	22	9	10
8	6	7	23	9	12
9	7	2	24	15	22
10	29	1	25	10	16
11	1	22	26	16	7
12	8	15	27	16	29
13	10	11	36	29	23
14	11	12	46	23	22
15	12	13			

### MAKROELEMENT 1 - SURFACES

Number	List of boundary lines
1	5,8,12,17,21-22,25-26
2	2,7-9
3	3,5-7
4	1,9,26-27
5	10,13,19-20,25,27
6	14-15,18-19
7	15-16,21,23
8	13-14,22-23
9	10-11,36,46
10	1-4,36,46
11	4,6,17,24
12	11-12,16,18,20,24

### MACROELEMENT 1 - PROPERTIES

Type of macroelement standard, azimuth = 0,00°, zenith = 0,00°

CS	Used	Material			
1	Yes	Ident	Material	Ratio [%]	Direction
		Basic	Concrete Slab		

### MACROELEMENT 2

#### MACROELEMENT 2 - JOINTS

Number	X [m]	Y [m]	Z [m]
1	0,0000	0,0000	-0,3000
2	0,1250	0,1250	-1,3000
3	0,0000	0,1250	-1,3000
4	0,0000	0,0000	-1,3000
5	0,1250	0,0000	-1,3000
6	0,1250	0,0000	-0,3000
7	0,1250	0,1250	-0,3000
8	0,0000	0,1250	-0,3000
9	0,0000	0,0000	-0,8000
10	0,1250	0,0000	-0,8000
11	0,1250	0,1250	-0,8000



Description:  
Note:

**Case Study, Unreinforced Slab**  
Cohesion = 1.0, Friction coefficient = 1.0

Unit system: Metric

side  
4

### MACROELEMENT 2 - JOINTS

Number	X [m]	Y [m]	Z [m]
12	0,0000	0,1250	-0,8000

### MAKROELEMENT 2 - LINES

Number	Joint at the beg.	Joint at the end	Number	Joint at the beg.	Joint at the end
1	2	5	11	1	6
2	4	5	12	1	9
3	4	3	13	9	4
4	3	2	14	3	12
5	12	8	15	11	12
6	8	1	16	12	9
7	7	11	17	9	10
8	6	7	18	10	11
9	6	10	19	11	2
10	8	7	20	5	10

### MAKROELEMENT 2 - SURFACES

Number	List of boundary lines
1	1-4
2	7-9,18
3	5,7,10,15
4	1,18-20
5	4,14-15,19
6	3,13-14,16
7	5-6,12,16
8	2,13,17,20
9	9,11-12,17
10	6,8,10-11

### MACROELEMENT 2 - PROPERTIES

Type of macroelement standard, azimuth = 0,00°, zenith = 0,00°

CS	Used	Material	Ratio [%]	Direction
1	Yes	Ident Basic	Material Elastic Pile	

## MACROELEMENT 3

### MACROELEMENT 3 - JOINTS

Number	X [m]	Y [m]	Z [m]
1	0,0000	0,0000	-1,3000
2	0,1250	0,1250	-1,3000
3	0,0000	0,1250	-1,3000
4	0,1250	0,0000	-1,3000
5	0,0000	0,0000	-1,3500
6	0,1250	0,1250	-1,3500
7	0,0000	0,1250	-1,3500
8	0,1250	0,0000	-1,3500

### MAKROELEMENT 3 - LINES

Number	Joint at the beg.	Joint at the end	Number	Joint at the beg.	Joint at the end
1	7	6	7	1	4
2	6	8	8	4	2
3	8	5	9	2	3
4	5	7	10	6	2



Description:	<b>Case Study, Unreinforced Slab</b>	Unit system:	Metric
Note:	Cohesion = 1.0, Friction coefficient = 1.0		

side  
5

### MAKROELEMENT 3 - LINES

Number	Joint at the beg.	Joint at the end	Number	Joint at the beg.	Joint at the end
5	7	3	11	4	8
6	3	1	12	1	5

### MAKROELEMENT 3 - SURFACES

Number	List of boundary lines
1	1,5,9-10
2	2,8,10-11
3	1-4
4	4-6,12
5	3,7,11-12
6	6-9

### MACROELEMENT 3 - PROPERTIES

Type of macroelement standard, azimuth = 0,00°, zenith = 0,00°

CS	Used	Material			
1	Yes	Ident	Material	Ratio [%]	Direction
		Basic	Steel Plate		

### MACROELEMENT 4

#### MACROELEMENT 4 - JOINTS


Number	X [m]	Y [m]	Z [m]
1	0,7000	1,9500	0,0000
2	0,9000	1,9500	0,0000
3	0,9000	1,7500	0,0000
4	0,7000	1,7500	0,0000
5	0,7000	1,7500	0,0500
6	0,7000	1,9500	0,0500
7	0,9000	1,9500	0,0500
8	0,9000	1,7500	0,0500
10	0,8000	1,8500	0,0500

### MAKROELEMENT 4 - LINES

Number	Joint at the beg.	Joint at the end	Number	Joint at the beg.	Joint at the end
1	1	2	9	6	7
2	2	3	10	10	7
3	3	4	11	7	8
4	4	1	12	8	5
5	4	5	13	5	10
6	3	8	14	10	8
7	2	7	15	10	6
8	1	6	16	6	5

### MAKROELEMENT 4 - SURFACES

Number	List of boundary lines
1	1-4
2	1,7-9
3	2,6-7,11
4	3,5-6,12
5	4-5,8,16
6	13,15-16
7	9-10,15
8	10-11,14

	Description:	<b>Case Study, Unreinforced Slab</b>	Unit system:	Metric	<b>side 6</b>
	Note:	Cohesion = 1.0, Friction coefficient = 1.0			

MAKROELEMENT 4 - SURFACES	
Number	List of boundary lines
9	12-14

MACROELEMENT 4 - PROPERTIES					
Type of macroelement standard, azimuth = 0,00°, zenith = 0,00°					
CS	Used	Material			
1	Yes	Ident	Material	Ratio [%]	Direction
		Basic	Steel Plate		

## MACROELEMENT 5


MACROELEMENT 5 - JOINTS				
Number	X [m]	Y [m]	Z [m]	Z [m]
1	1,9500	0,7000	0,0000	0,0000
2	1,9500	0,9000	0,0000	0,0000
3	1,9500	0,9000	0,0500	0,0500
4	1,9500	0,7000	0,0500	0,0500
5	1,7500	0,7000	0,0500	0,0500
6	1,7500	0,7000	0,0000	0,0000
7	1,7500	0,9000	0,0000	0,0000
8	1,7500	0,9000	0,0500	0,0500
9	1,8500	0,8000	0,0500	0,0500

MAKROELEMENT 5 - LINES					
Number	Joint at the beg.	Joint at the end	Number	Joint at the beg.	Joint at the end
1	2	7	9	6	5
2	6	7	10	5	4
3	6	1	11	4	1
4	1	2	12	3	4
5	2	3	13	9	3
6	3	8	14	9	5
7	8	7	15	9	8
8	8	5	16	9	4

MAKROELEMENT 5 - SURFACES	
Number	List of boundary lines
1	4-5,11-12
2	1-4
3	3,9-11
4	2,7-9
5	1,5-7
6	6,13,15
7	12-13,16
8	10,14,16
9	8,14-15

MACROELEMENT 5 - PROPERTIES					
Type of macroelement standard, azimuth = 0,00°, zenith = 0,00°					
CS	Used	Material			
1	Yes	Ident	Material	Ratio [%]	Direction
		Basic	Steel Plate		

## CONTACTS

	Description:	<b>Case Study, Unreinforced Slab</b>	Unit system:	Metric	<b>side 7</b>
	Note:	Cohesion = 1.0, Friction coefficient = 1.0			

CONTACTS - TOPOLOGY			
Number	Macroelement A - surface	Macroelement B - surface	Preferred master
1	2/2	1/7	automatic
2	2/3	1/8	automatic
3	2/10	1/6	automatic
4	3/6	2/1	automatic
5	4/1	1/10	automatic
6	5/2	1/10	automatic

CONTACT 1 - PROPERTIES			
CS	Used	Contact	Material
1	Yes	contact element - GAP	Interface

CONTACT 2 - PROPERTIES			
CS	Used	Contact	Material
1	Yes	contact element - GAP	Interface

CONTACT 3 - PROPERTIES			
CS	Used	Contact	Material
1	Yes	perfect connection	

CONTACT 4 - PROPERTIES			
CS	Used	Contact	Material
1	Yes	perfect connection	

CONTACT 5 - PROPERTIES			
CS	Used	Contact	Material
1	Yes	perfect connection	

CONTACT 6 - PROPERTIES			
CS	Used	Contact	Material
1	Yes	perfect connection	

## LOAD CASES - OVERVIEW

LOAD CASE LIST			
Number	Title	Code	Coeff.[-]
1	Own Weight	Body force	1,000
2	Boundary Conditions	Supports	
3	Prescribed Deformation	Prescribed deformation	1,000

## LC 1 - OWN WEIGHT

BODY FORCE	
Dir: (0,0000; 0,0000; -1,0000)	
Macroelements:	
Reinforcement bars:	
External cables:	

## LC 2 - BOUNDARY CONDITIONS

SURFACE SUPPORTS				
Macro. / surface	Coordinate system	Support in dir. of the axis		
		X	Y	Z
1/2	Global	free	fixed	free
1/3	Global	fixed	free	free





Description:  
Note:

**Case Study, Unreinforced Slab**  
Cohesion = 1.0, Friction coefficient = 1.0

Unit system:

Metric

side  
8

### SURFACE SUPPORTS

Macro. / surface	Coordinate system	Support in dir. of the axis		
		X	Y	Z
1/4	Global	fixed	free	free
1/5	Global	fixed	free	free
1/11	Global	free	fixed	free
1/12	Global	free	fixed	free
2/6	Global	fixed	free	free
2/7	Global	fixed	free	free
2/8	Global	free	fixed	free
2/9	Global	free	fixed	free
3/3	Global	free	free	fixed
3/4	Global	fixed	free	free
3/5	Global	free	fixed	free

## LC 3 - PRESCRIBED DEFORMATION

### SUPPORTS AND PRESCRIBED DEFORMATIONS OF JOINTS

Macro. / joint	Coordinate system	Support and deformation in the direction of the axis		
		X [m]	Y [m]	Z [m]
4/10	Global	free	free	fixed: -5,000E-04
5/9	Global	free	free	fixed: -5,000E-04

## SOLUTION PARAMETERS

### SOLUTION PARAMETERS 1

Property	Value
Title	Standard Newton-Raphson
Method	Newton-Raphson (line search)
Iteration limit	40
Displacement Error	0,010000
Residual Error	0,010000
Absolute Residual Error	0,010000
Energy Error	0,000100
Optimize band-width	Sloan
Line Search	Yes
LS Type	With iterations
LS Unbalanced energy limit	0,800
LS Line search iteration limit	2
LS Minimum Eta	0,010
LS Maximum Eta	1,000
Update Stiffness	Each iteration
Stiffness Type	Tangent
Immediate Displacement Error Multiple	10000,0
After Step Displacement Error Multiple	1000,0
Immediate Residual Error Multiple	10000,0
After Step Residual Error Multiple	1000,0
Immediate Absolute Residual Error Multiple	10000,0
After Step Absolute Residual Error Multiple	1000,0
Immediate Energy Error Multiple	1000000,0
After Step Energy Error Multiple	10000,0



Description:  
Note:

**Case Study, Unreinforced Slab**  
Cohesion = 1.0, Friction coefficient = 1.0

Unit system:

Metric


side  
9

### SOLUTION PARAMETERS 2

Property	Value
Title	Standard Arc Length
Method	Arc length (line search)
Arc Length Method	Consistently linearised
A-L Adjustment Method	Constant
A-L Load-Displacement Ratio	0,200
A-L Load-Displacement Method	Bergan constant
A-L Reference number of iterations	10
A-L Step-Length	Based on current load step
A-L Location	All nodes
Iteration limit	40
Displacement Error	0,010000
Residual Error	0,010000
Absolute Residual Error	0,010000
Energy Error	0,000100
Optimize band-width	Sloan
Line Search	Yes
LS Type	With iterations
LS Unbalanced energy limit	0,800
LS Line search iteration limit	2
LS Minimum Eta	0,010
LS Maximum Eta	1,000
Update Stiffness	Each iteration
Stiffness Type	Tangent
Immediate Displacement Error Multiple	10000,0
After Step Displacement Error Multiple	1000,0
Immediate Residual Error Multiple	10000,0
After Step Residual Error Multiple	1000,0
Immediate Absolute Residual Error Multiple	10000,0
After Step Absolute Residual Error Multiple	1000,0
Immediate Energy Error Multiple	1000000,0
After Step Energy Error Multiple	10000,0

### SOLUTION PARAMETERS 3

Property	Value
Title	Analysis parameter 3
Method	Newton-Raphson
Iteration limit	30
Displacement Error	0,010000
Residual Error	0,010000
Absolute Residual Error	0,010000
Energy Error	0,000100
Optimize band-width	Sloan
Line Search	No
Update Stiffness	Each iteration
Stiffness Type	Elastic
Immediate Displacement Error Multiple	200,0
After Step Displacement Error Multiple	50,0
Immediate Residual Error Multiple	200,0
After Step Residual Error Multiple	50,0
Immediate Absolute Residual Error Multiple	200,0
After Step Absolute Residual Error Multiple	50,0

	Description:	<b>Case Study, Unreinforced Slab</b>	Unit system:	Metric	<b>side 10</b>
	Note:	Cohesion = 1.0, Friction coefficient = 1.0			

### SOLUTION PARAMETERS 3


Property	Value
Immediate Energy Error Multiple	200,0
After Step Energy Error Multiple	50,0

### ANALYSIS STEPS

Number	Load cases	Phase	Solution Parameters	Coefficient [-]
1	1-3	(1) Construction Case 1	Standard Newton-Raphson	0,500
2	1-3	(1) Construction Case 1	Standard Newton-Raphson	0,500
3	1-3	(1) Construction Case 1	Standard Newton-Raphson	0,500
4	1-3	(1) Construction Case 1	Standard Newton-Raphson	0,500
5	1-3	(1) Construction Case 1	Standard Newton-Raphson	0,500
6	1-3	(1) Construction Case 1	Standard Newton-Raphson	0,500
7	1-3	(1) Construction Case 1	Standard Newton-Raphson	0,500
8	1-3	(1) Construction Case 1	Standard Newton-Raphson	0,500
9	1-3	(1) Construction Case 1	Standard Newton-Raphson	0,500
10	1-3	(1) Construction Case 1	Standard Newton-Raphson	0,500
11	1-3	(1) Construction Case 1	Standard Newton-Raphson	0,500
12	1-3	(1) Construction Case 1	Standard Newton-Raphson	0,500
13	1-3	(1) Construction Case 1	Standard Newton-Raphson	0,500
14	1-3	(1) Construction Case 1	Standard Newton-Raphson	0,500
15	1-3	(1) Construction Case 1	Standard Newton-Raphson	0,500
16	1-3	(1) Construction Case 1	Standard Newton-Raphson	0,500
17	1-3	(1) Construction Case 1	Standard Newton-Raphson	0,500
18	1-3	(1) Construction Case 1	Standard Newton-Raphson	0,500
19	1-3	(1) Construction Case 1	Standard Newton-Raphson	0,500
20	1-3	(1) Construction Case 1	Standard Newton-Raphson	0,500

### MONITORING POINTS

Number	Title	Type Location	Quantity - item
1	Displacement 1	Value at node Macroelement 1, point (0,2500; 0,2500; 0,0000) [m]	Displacements - Component 3
2	Displacement 2	Value at node Macroelement 1, point (1,5000; 1,5000; 0,0000) [m]	Displacements - Component 3
3	Displacement 3	Value at node Macroelement 2, point (0,0000; 0,0000; -0,8000) [m]	Displacements - Component 3
4	Force 1	Value at node Macroelement 4, point (0,8000; 1,8500; 0,0500) [m]	Reactions - Component 3
5	Force 2	Value at node Macroelement 5, point (1,8500; 0,8000; 0,0500) [m]	Reactions - Component 3

	Description:	<b>Case Study, Reinforced Slab</b>	Unit system:	Metric	<b>side 1</b>
	Note:	Cohesion =1.0, Friction coefficient =1.0			

## ANALYSIS INFORMATION

Property	Value
Description	Case Study, Reinforced Slab
Note	Cohesion =1.0, Friction coefficient =1.0
Unit system	Metric
Solver type	standard
Run	geometrically nonlinear

## BAR REINFORCEMENT

### BAR REINFORCEMENT 1

BAR REINFORCEMENT 1 - POINTS			
Number	X [m]	Y [m]	Z [m]
1	0,1000	0,0000	-0,0400
2	0,1000	2,0000	-0,0400

BAR REINFORCEMENT 1 - SEGMENTS					
Number	Start point	End point	Number	Start point	End point
1	2	1			

BAR REINFORCEMENT 1 - PROPERTIES					
CS	Used	Material	Area [m <sup>2</sup> ]	Bond with surrounding material	
1	Yes	Reinforcement	4,909E-04	Connection type	perfect connection

### BAR REINFORCEMENT 2

BAR REINFORCEMENT 2 - POINTS			
Number	X [m]	Y [m]	Z [m]
1	0,3000	0,0000	-0,0400
2	0,3000	2,0000	-0,0400

BAR REINFORCEMENT 2 - SEGMENTS					
Number	Start point	End point	Number	Start point	End point
1	2	1			

BAR REINFORCEMENT 2 - PROPERTIES					
CS	Used	Material	Area [m <sup>2</sup> ]	Bond with surrounding material	
1	Yes	Reinforcement	4,909E-04	Connection type	perfect connection


### BAR REINFORCEMENT 3

BAR REINFORCEMENT 3 - POINTS			
Number	X [m]	Y [m]	Z [m]
1	0,5000	0,0000	-0,0400
2	0,5000	2,0000	-0,0400

BAR REINFORCEMENT 3 - SEGMENTS					
Number	Start point	End point	Number	Start point	End point
1	2	1			

BAR REINFORCEMENT 3 - PROPERTIES					
CS	Used	Material	Area [m <sup>2</sup> ]	Bond with surrounding material	
1	Yes	Reinforcement	4,909E-04	Connection type	perfect connection

### BAR REINFORCEMENT 4

	Description:	<b>Case Study, Reinforced Slab</b>	Unit system:	Metric	<b>side 2</b>
	Note:	Cohesion =1.0, Friction coefficient =1.0			

BAR REINFORCEMENT 4 - POINTS				
Number	X [m]	Y [m]	Z [m]	
1	0,7000	0,0000	-0,0400	
2	0,7000	2,0000	-0,0400	

BAR REINFORCEMENT 4 - SEGMENTS					
Number	Start point	End point	Number	Start point	End point
1	2	1			

BAR REINFORCEMENT 4 - PROPERTIES					
CS	Used	Material	Area [m <sup>2</sup> ]	Bond with surrounding material	
1	Yes	Reinforcement	4,909E-04	Connection type	perfect connection

### BAR REINFORCEMENT 5

BAR REINFORCEMENT 5 - POINTS				
Number	X [m]	Y [m]	Z [m]	
1	0,9000	0,0000	-0,0400	
2	0,9000	2,0000	-0,0400	

BAR REINFORCEMENT 5 - SEGMENTS					
Number	Start point	End point	Number	Start point	End point
1	2	1			

BAR REINFORCEMENT 5 - PROPERTIES					
CS	Used	Material	Area [m <sup>2</sup> ]	Bond with surrounding material	
1	Yes	Reinforcement	4,909E-04	Connection type	perfect connection

### BAR REINFORCEMENT 6

BAR REINFORCEMENT 6 - POINTS				
Number	X [m]	Y [m]	Z [m]	
1	1,1000	0,0000	-0,0400	
2	1,1000	2,0000	-0,0400	

BAR REINFORCEMENT 6 - SEGMENTS					
Number	Start point	End point	Number	Start point	End point
1	2	1			

BAR REINFORCEMENT 6 - PROPERTIES					
CS	Used	Material	Area [m <sup>2</sup> ]	Bond with surrounding material	
1	Yes	Reinforcement	4,909E-04	Connection type	perfect connection

### BAR REINFORCEMENT 7

BAR REINFORCEMENT 7 - POINTS				
Number	X [m]	Y [m]	Z [m]	
1	1,3000	0,0000	-0,0400	
2	1,3000	2,0000	-0,0400	

BAR REINFORCEMENT 7 - SEGMENTS					
Number	Start point	End point	Number	Start point	End point
1	2	1			

BAR REINFORCEMENT 7 - PROPERTIES					
CS	Used	Material	Area [m <sup>2</sup> ]	Bond with surrounding material	
1	Yes	Reinforcement	4,909E-04	Connection type	perfect connection



Description:	<b>Case Study, Reinforced Slab</b>	Unit system:	Metric
Note:	Cohesion =1.0, Friction coefficient =1.0		

side  
3

### BAR REINFORCEMENT 8

#### BAR REINFORCEMENT 8 - POINTS

Number	X [m]	Y [m]	Z [m]
1	1,5000	0,0000	-0,0400
2	1,5000	2,0000	-0,0400

#### BAR REINFORCEMENT 8 - SEGMENTS

Number	Start point	End point	Number	Start point	End point
1	2	1			

#### BAR REINFORCEMENT 8 - PROPERTIES

CS	Used	Material	Area [m <sup>2</sup> ]	Bond with surrounding material	
1	Yes	Reinforcement	4,909E-04	Connection type	perfect connection

### BAR REINFORCEMENT 9

#### BAR REINFORCEMENT 9 - POINTS

Number	X [m]	Y [m]	Z [m]
1	1,7000	0,0000	-0,0400
2	1,7000	2,0000	-0,0400

#### BAR REINFORCEMENT 9 - SEGMENTS

Number	Start point	End point	Number	Start point	End point
1	2	1			

#### BAR REINFORCEMENT 9 - PROPERTIES

CS	Used	Material	Area [m <sup>2</sup> ]	Bond with surrounding material	
1	Yes	Reinforcement	4,909E-04	Connection type	perfect connection

### BAR REINFORCEMENT 10

#### BAR REINFORCEMENT 10 - POINTS

Number	X [m]	Y [m]	Z [m]
1	1,9000	0,0000	-0,0400
2	1,9000	2,0000	-0,0400

#### BAR REINFORCEMENT 10 - SEGMENTS

Number	Start point	End point	Number	Start point	End point
1	2	1			

#### BAR REINFORCEMENT 10 - PROPERTIES

CS	Used	Material	Area [m <sup>2</sup> ]	Bond with surrounding material	
1	Yes	Reinforcement	4,909E-04	Connection type	perfect connection

### BAR REINFORCEMENT 11

#### BAR REINFORCEMENT 11 - POINTS

Number	X [m]	Y [m]	Z [m]
1	0,0000	0,1000	-0,0650
2	2,0000	0,1000	-0,0650

#### BAR REINFORCEMENT 11 - SEGMENTS

Number	Start point	End point	Number	Start point	End point
1	1	2			



Description:	<b>Case Study, Reinforced Slab</b>	Unit system:	Metric
Note:	Cohesion =1.0, Friction coefficient =1.0		

side  
4

**BAR REINFORCEMENT 11 - PROPERTIES**

CS	Used	Material	Area [m <sup>2</sup> ]	Bond with surrounding material	
1	Yes	Reinforcement	4,909E-04	Connection type	perfect connection

**BAR REINFORCEMENT 12**

**BAR REINFORCEMENT 12 - POINTS**

Number	X [m]	Y [m]	Z [m]
1	0,0000	0,3000	-0,0650
2	2,0000	0,3000	-0,0650

**BAR REINFORCEMENT 12 - SEGMENTS**

Number	Start point	End point	Number	Start point	End point
1	1	2			

**BAR REINFORCEMENT 12 - PROPERTIES**

CS	Used	Material	Area [m <sup>2</sup> ]	Bond with surrounding material	
1	Yes	Reinforcement	4,909E-04	Connection type	perfect connection

**BAR REINFORCEMENT 13**

**BAR REINFORCEMENT 13 - POINTS**

Number	X [m]	Y [m]	Z [m]
1	0,0000	0,5000	-0,0650
2	2,0000	0,5000	-0,0650

**BAR REINFORCEMENT 13 - SEGMENTS**

Number	Start point	End point	Number	Start point	End point
1	1	2			

**BAR REINFORCEMENT 13 - PROPERTIES**

CS	Used	Material	Area [m <sup>2</sup> ]	Bond with surrounding material	
1	Yes	Reinforcement	4,909E-04	Connection type	perfect connection

**BAR REINFORCEMENT 14**

**BAR REINFORCEMENT 14 - POINTS**

Number	X [m]	Y [m]	Z [m]
1	0,0000	0,7000	-0,0650
2	2,0000	0,7000	-0,0650

**BAR REINFORCEMENT 14 - SEGMENTS**

Number	Start point	End point	Number	Start point	End point
1	1	2			

**BAR REINFORCEMENT 14 - PROPERTIES**

CS	Used	Material	Area [m <sup>2</sup> ]	Bond with surrounding material	
1	Yes	Reinforcement	4,909E-04	Connection type	perfect connection

**BAR REINFORCEMENT 15**

**BAR REINFORCEMENT 15 - POINTS**

Number	X [m]	Y [m]	Z [m]
1	0,0000	0,9000	-0,0650
2	2,0000	0,9000	-0,0650



Description:	<b>Case Study, Reinforced Slab</b>	Unit system:	Metric
Note:	Cohesion =1.0, Friction coefficient =1.0		

side  
5

### BAR REINFORCEMENT 15 - SEGMENTS

Number	Start point	End point	Number	Start point	End point
1	1	2			

### BAR REINFORCEMENT 15 - PROPERTIES

CS	Used	Material	Area [m <sup>2</sup> ]	Bond with surrounding material	
1	Yes	Reinforcement	4,909E-04	Connection type	perfect connection

### BAR REINFORCEMENT 16

#### BAR REINFORCEMENT 16 - POINTS

Number	X [m]	Y [m]	Z [m]
1	0,0000	1,1000	-0,0650
2	2,0000	1,1000	-0,0650

### BAR REINFORCEMENT 16 - SEGMENTS

Number	Start point	End point	Number	Start point	End point
1	1	2			

### BAR REINFORCEMENT 16 - PROPERTIES

CS	Used	Material	Area [m <sup>2</sup> ]	Bond with surrounding material	
1	Yes	Reinforcement	4,909E-04	Connection type	perfect connection

### BAR REINFORCEMENT 17

#### BAR REINFORCEMENT 17 - POINTS

Number	X [m]	Y [m]	Z [m]
1	0,0000	1,3000	-0,0650
2	2,0000	1,3000	-0,0650

### BAR REINFORCEMENT 17 - SEGMENTS

Number	Start point	End point	Number	Start point	End point
1	1	2			

### BAR REINFORCEMENT 17 - PROPERTIES

CS	Used	Material	Area [m <sup>2</sup> ]	Bond with surrounding material	
1	Yes	Reinforcement	4,909E-04	Connection type	perfect connection

### BAR REINFORCEMENT 18

#### BAR REINFORCEMENT 18 - POINTS

Number	X [m]	Y [m]	Z [m]
1	0,0000	1,5000	-0,0650
2	2,0000	1,5000	-0,0650

### BAR REINFORCEMENT 18 - SEGMENTS

Number	Start point	End point	Number	Start point	End point
1	1	2			

### BAR REINFORCEMENT 18 - PROPERTIES


CS	Used	Material	Area [m <sup>2</sup> ]	Bond with surrounding material	
1	Yes	Reinforcement	4,909E-04	Connection type	perfect connection

### BAR REINFORCEMENT 19

#### BAR REINFORCEMENT 19 - POINTS

Number	X [m]	Y [m]	Z [m]
1	0,0000	1,7000	-0,0650



	Description:	<b>Case Study, Reinforced Slab</b>	Unit system:	Metric	<b>side 6</b>
	Note:	Cohesion =1.0, Friction coefficient =1.0			

**BAR REINFORCEMENT 19 - POINTS**

Number	X [m]	Y [m]	Z [m]
2	2,0000	1,7000	-0,0650

**BAR REINFORCEMENT 19 - SEGMENTS**

Number	Start point	End point	Number	Start point	End point
1	1	2			

**BAR REINFORCEMENT 19 - PROPERTIES**

CS	Used	Material	Area [m <sup>2</sup> ]	Bond with surrounding material	
1	Yes	Reinforcement	4,909E-04	Connection type	perfect connection

**BAR REINFORCEMENT 20**

**BAR REINFORCEMENT 20 - POINTS**

Number	X [m]	Y [m]	Z [m]
1	0,0000	1,9000	-0,0650
2	2,0000	1,9000	-0,0650

**BAR REINFORCEMENT 20 - SEGMENTS**

Number	Start point	End point	Number	Start point	End point
1	1	2			

**BAR REINFORCEMENT 20 - PROPERTIES**

CS	Used	Material	Area [m <sup>2</sup> ]	Bond with surrounding material	
1	Yes	Reinforcement	4,909E-04	Connection type	perfect connection

**BAR REINFORCEMENT 21**

**BAR REINFORCEMENT 21 - POINTS**

Number	X [m]	Y [m]	Z [m]
1	0,1500	0,1000	-0,7600
2	2,0000	0,1000	-0,7600

**BAR REINFORCEMENT 21 - SEGMENTS**

Number	Start point	End point	Number	Start point	End point
1	1	2			

**BAR REINFORCEMENT 21 - PROPERTIES**

CS	Used	Material	Area [m <sup>2</sup> ]	Bond with surrounding material	
1	Yes	Reinforcement	4,909E-04	Connection type	perfect connection

**BAR REINFORCEMENT 22**

**BAR REINFORCEMENT 22 - POINTS**

Number	X [m]	Y [m]	Z [m]
1	0,0000	0,3000	-0,7600
2	2,0000	0,3000	-0,7600

**BAR REINFORCEMENT 22 - SEGMENTS**

Number	Start point	End point	Number	Start point	End point
1	1	2			

**BAR REINFORCEMENT 22 - PROPERTIES**

CS	Used	Material	Area [m <sup>2</sup> ]	Bond with surrounding material	
1	Yes	Reinforcement	4,909E-04	Connection type	perfect connection

**BAR REINFORCEMENT 23**



Description:	<b>Case Study, Reinforced Slab</b>	Unit system:	Metric
Note:	Cohesion =1.0, Friction coefficient =1.0		

side  
7

**BAR REINFORCEMENT 23 - POINTS**

Number	X [m]	Y [m]	Z [m]
1	0,0000	0,5000	-0,7600
2	2,0000	0,5000	-0,7600

**BAR REINFORCEMENT 23 - SEGMENTS**

Number	Start point	End point	Number	Start point	End point
1	1	2			

**BAR REINFORCEMENT 23 - PROPERTIES**

CS	Used	Material	Area [m <sup>2</sup> ]	Bond with surrounding material	
1	Yes	Reinforcement	4,909E-04	Connection type	perfect connection

**BAR REINFORCEMENT 24**

**BAR REINFORCEMENT 24 - POINTS**

Number	X [m]	Y [m]	Z [m]
1	0,0000	0,7000	-0,7600
2	2,0000	0,7000	-0,7600

**BAR REINFORCEMENT 24 - SEGMENTS**

Number	Start point	End point	Number	Start point	End point
1	1	2			

**BAR REINFORCEMENT 24 - PROPERTIES**

CS	Used	Material	Area [m <sup>2</sup> ]	Bond with surrounding material	
1	Yes	Reinforcement	4,909E-04	Connection type	perfect connection

**BAR REINFORCEMENT 25**

**BAR REINFORCEMENT 25 - POINTS**

Number	X [m]	Y [m]	Z [m]
1	0,0000	0,9000	-0,7600
2	2,0000	0,9000	-0,7600

**BAR REINFORCEMENT 25 - SEGMENTS**

Number	Start point	End point	Number	Start point	End point
1	1	2			

**BAR REINFORCEMENT 25 - PROPERTIES**

CS	Used	Material	Area [m <sup>2</sup> ]	Bond with surrounding material	
1	Yes	Reinforcement	4,909E-04	Connection type	perfect connection

**BAR REINFORCEMENT 26**

**BAR REINFORCEMENT 26 - POINTS**

Number	X [m]	Y [m]	Z [m]
1	0,0000	1,1000	-0,7600
2	2,0000	1,1000	-0,7600

**BAR REINFORCEMENT 26 - SEGMENTS**

Number	Start point	End point	Number	Start point	End point
1	1	2			

**BAR REINFORCEMENT 26 - PROPERTIES**

CS	Used	Material	Area [m <sup>2</sup> ]	Bond with surrounding material	
1	Yes	Reinforcement	4,909E-04	Connection type	perfect connection



Description:	<b>Case Study, Reinforced Slab</b>	Unit system:	Metric
Note:	Cohesion =1.0, Friction coefficient =1.0		

side  
8

### BAR REINFORCEMENT 27

#### BAR REINFORCEMENT 27 - POINTS

Number	X [m]	Y [m]	Z [m]
1	0,0000	1,3000	-0,7600
2	2,0000	1,3000	-0,7600

#### BAR REINFORCEMENT 27 - SEGMENTS

Number	Start point	End point	Number	Start point	End point
1	1	2			

#### BAR REINFORCEMENT 27 - PROPERTIES

CS	Used	Material	Area [m <sup>2</sup> ]	Bond with surrounding material	
1	Yes	Reinforcement	4,909E-04	Connection type	perfect connection

### BAR REINFORCEMENT 28

#### BAR REINFORCEMENT 28 - POINTS

Number	X [m]	Y [m]	Z [m]
1	0,0000	1,5000	-0,7600
2	2,0000	1,5000	-0,7600

#### BAR REINFORCEMENT 28 - SEGMENTS

Number	Start point	End point	Number	Start point	End point
1	1	2			

#### BAR REINFORCEMENT 28 - PROPERTIES

CS	Used	Material	Area [m <sup>2</sup> ]	Bond with surrounding material	
1	Yes	Reinforcement	4,909E-04	Connection type	perfect connection

### BAR REINFORCEMENT 29

#### BAR REINFORCEMENT 29 - POINTS

Number	X [m]	Y [m]	Z [m]
1	0,0000	1,7000	-0,7600
2	2,0000	1,7000	-0,7600

#### BAR REINFORCEMENT 29 - SEGMENTS

Number	Start point	End point	Number	Start point	End point
1	1	2			

#### BAR REINFORCEMENT 29 - PROPERTIES

CS	Used	Material	Area [m <sup>2</sup> ]	Bond with surrounding material	
1	Yes	Reinforcement	4,909E-04	Connection type	perfect connection

### BAR REINFORCEMENT 30

#### BAR REINFORCEMENT 30 - POINTS

Number	X [m]	Y [m]	Z [m]
1	0,0000	1,9000	-0,7600
2	2,0000	1,9000	-0,7600

#### BAR REINFORCEMENT 30 - SEGMENTS

Number	Start point	End point	Number	Start point	End point
1	1	2			



Description:	<b>Case Study, Reinforced Slab</b>	Unit system:	Metric
Note:	Cohesion =1.0, Friction coefficient =1.0		

**BAR REINFORCEMENT 30 - PROPERTIES**

CS	Used	Material	Area [m <sup>2</sup> ]	Bond with surrounding material	
1	Yes	Reinforcement	4,909E-04	Connection type	perfect connection

**BAR REINFORCEMENT 31**

**BAR REINFORCEMENT 31 - POINTS**

Number	X [m]	Y [m]	Z [m]
1	0,1000	0,1500	-0,7350
2	0,1000	2,0000	-0,7350

**BAR REINFORCEMENT 31 - SEGMENTS**

Number	Start point	End point	Number	Start point	End point
1	2	1			

**BAR REINFORCEMENT 31 - PROPERTIES**

CS	Used	Material	Area [m <sup>2</sup> ]	Bond with surrounding material	
1	Yes	Reinforcement	4,909E-04	Connection type	perfect connection

**BAR REINFORCEMENT 32**

**BAR REINFORCEMENT 32 - POINTS**

Number	X [m]	Y [m]	Z [m]
1	0,3000	0,0000	-0,7350
2	0,3000	2,0000	-0,7350

**BAR REINFORCEMENT 32 - SEGMENTS**

Number	Start point	End point	Number	Start point	End point
1	1	2			

**BAR REINFORCEMENT 32 - PROPERTIES**

CS	Used	Material	Area [m <sup>2</sup> ]	Bond with surrounding material	
1	Yes	Reinforcement	4,909E-04	Connection type	perfect connection

**BAR REINFORCEMENT 33**

**BAR REINFORCEMENT 33 - POINTS**

Number	X [m]	Y [m]	Z [m]
1	0,5000	0,0000	-0,7350
2	0,5000	2,0000	-0,7350

**BAR REINFORCEMENT 33 - SEGMENTS**

Number	Start point	End point	Number	Start point	End point
1	1	2			

**BAR REINFORCEMENT 33 - PROPERTIES**

CS	Used	Material	Area [m <sup>2</sup> ]	Bond with surrounding material	
1	Yes	Reinforcement	4,909E-04	Connection type	perfect connection

**BAR REINFORCEMENT 34**

**BAR REINFORCEMENT 34 - POINTS**

Number	X [m]	Y [m]	Z [m]
1	0,7000	0,0000	-0,7350
2	0,7000	2,0000	-0,7350



Description:	<b>Case Study, Reinforced Slab</b>	Unit system:	Metric
Note:	Cohesion =1.0, Friction coefficient =1.0		

side  
**10**

**BAR REINFORCEMENT 34 - SEGMENTS**

Number	Start point	End point	Number	Start point	End point
1	1	2			

**BAR REINFORCEMENT 34 - PROPERTIES**

CS	Used	Material	Area [m <sup>2</sup> ]	Bond with surrounding material	
1	Yes	Reinforcement	4,909E-04	Connection type	perfect connection

**BAR REINFORCEMENT 35**

**BAR REINFORCEMENT 35 - POINTS**

Number	X [m]	Y [m]	Z [m]
1	0,9000	0,0000	-0,7350
2	0,9000	2,0000	-0,7350

**BAR REINFORCEMENT 35 - SEGMENTS**

Number	Start point	End point	Number	Start point	End point
1	1	2			

**BAR REINFORCEMENT 35 - PROPERTIES**

CS	Used	Material	Area [m <sup>2</sup> ]	Bond with surrounding material	
1	Yes	Reinforcement	4,909E-04	Connection type	perfect connection

**BAR REINFORCEMENT 36**

**BAR REINFORCEMENT 36 - POINTS**

Number	X [m]	Y [m]	Z [m]
1	1,1000	0,0000	-0,7350
2	1,1000	2,0000	-0,7350

**BAR REINFORCEMENT 36 - SEGMENTS**

Number	Start point	End point	Number	Start point	End point
1	1	2			

**BAR REINFORCEMENT 36 - PROPERTIES**

CS	Used	Material	Area [m <sup>2</sup> ]	Bond with surrounding material	
1	Yes	Reinforcement	4,909E-04	Connection type	perfect connection

**BAR REINFORCEMENT 37**

**BAR REINFORCEMENT 37 - POINTS**

Number	X [m]	Y [m]	Z [m]
1	1,3000	0,0000	-0,7350
2	1,3000	2,0000	-0,7350

**BAR REINFORCEMENT 37 - SEGMENTS**

Number	Start point	End point	Number	Start point	End point
1	1	2			

**BAR REINFORCEMENT 37 - PROPERTIES**

CS	Used	Material	Area [m <sup>2</sup> ]	Bond with surrounding material	
1	Yes	Reinforcement	4,909E-04	Connection type	perfect connection

**BAR REINFORCEMENT 38**

**BAR REINFORCEMENT 38 - POINTS**

Number	X [m]	Y [m]	Z [m]
1	1,5000	0,0000	-0,7350



Description:	<b>Case Study, Reinforced Slab</b>	Unit system:	Metric
Note:	Cohesion =1.0, Friction coefficient =1.0		

side  
**11**

**BAR REINFORCEMENT 38 - POINTS**

Number	X [m]	Y [m]	Z [m]
2	1,5000	2,0000	-0,7350

**BAR REINFORCEMENT 38 - SEGMENTS**

Number	Start point	End point	Number	Start point	End point
1	1	2			

**BAR REINFORCEMENT 38 - PROPERTIES**

CS	Used	Material	Area [m <sup>2</sup> ]	Bond with surrounding material	
1	Yes	Reinforcement	4,909E-04	Connection type	perfect connection

**BAR REINFORCEMENT 39**

**BAR REINFORCEMENT 39 - POINTS**

Number	X [m]	Y [m]	Z [m]
1	1,7000	0,0000	-0,7350
2	1,7000	2,0000	-0,7350

**BAR REINFORCEMENT 39 - SEGMENTS**

Number	Start point	End point	Number	Start point	End point
1	1	2			

**BAR REINFORCEMENT 39 - PROPERTIES**

CS	Used	Material	Area [m <sup>2</sup> ]	Bond with surrounding material	
1	Yes	Reinforcement	4,909E-04	Connection type	perfect connection

**BAR REINFORCEMENT 40**

**BAR REINFORCEMENT 40 - POINTS**

Number	X [m]	Y [m]	Z [m]
1	1,9000	0,0000	-0,7350
2	1,9000	2,0000	-0,7350

**BAR REINFORCEMENT 40 - SEGMENTS**

Number	Start point	End point	Number	Start point	End point
1	1	2			

**BAR REINFORCEMENT 40 - PROPERTIES**

CS	Used	Material	Area [m <sup>2</sup> ]	Bond with surrounding material	
1	Yes	Reinforcement	4,909E-04	Connection type	perfect connection

**BAR REINFORCEMENT 41**

**BAR REINFORCEMENT 41 - POINTS**

Number	X [m]	Y [m]	Z [m]
1	0,2000	0,0000	-0,0300
2	0,2000	0,1080	-0,0300
3	0,2000	0,1080	-0,7700
4	0,2000	0,0000	-0,7700

**BAR REINFORCEMENT 41 - SEGMENTS**

Number	Start point	End point	Number	Start point	End point
1	4	3	3	2	1
2	2	3			



Description:	<b>Case Study, Reinforced Slab</b>	Unit system:	Metric
Note:	Cohesion =1.0, Friction coefficient =1.0		

side  
12

**BAR REINFORCEMENT 41 - PROPERTIES**

CS	Used	Material	Area [m <sup>2</sup> ]	Bond with surrounding material	
1	Yes	Reinforcement	2,011E-04	Connection type	perfect connection

**BAR REINFORCEMENT 42**

**BAR REINFORCEMENT 42 - POINTS**

Number	X [m]	Y [m]	Z [m]
1	0,0000	0,2000	-0,0300
2	0,1080	0,2000	-0,0300
3	0,1080	0,2000	-0,7700
4	0,0000	0,2000	-0,7700

**BAR REINFORCEMENT 42 - SEGMENTS**

Number	Start point	End point	Number	Start point	End point
1	1	2	3	3	4
2	2	3			

**BAR REINFORCEMENT 42 - PROPERTIES**

CS	Used	Material	Area [m <sup>2</sup> ]	Bond with surrounding material	
1	Yes	Reinforcement	2,011E-04	Connection type	perfect connection

**BAR REINFORCEMENT 43**

**BAR REINFORCEMENT 43 - POINTS**

Number	X [m]	Y [m]	Z [m]
1	0,0000	0,3500	-0,0300
2	0,1080	0,3500	-0,0300
3	0,1080	0,3500	-0,7700
4	0,0000	0,3500	-0,7700

**BAR REINFORCEMENT 43 - SEGMENTS**

Number	Start point	End point	Number	Start point	End point
1	1	2	3	3	4
2	2	3			

**BAR REINFORCEMENT 43 - PROPERTIES**

CS	Used	Material	Area [m <sup>2</sup> ]	Bond with surrounding material	
1	Yes	Reinforcement	2,011E-04	Connection type	perfect connection

**BAR REINFORCEMENT 44**

**BAR REINFORCEMENT 44 - POINTS**

Number	X [m]	Y [m]	Z [m]
1	0,0920	0,3200	-0,0300
2	0,3080	0,3200	-0,0300
3	0,3080	0,3200	-0,7700
4	0,0920	0,3200	-0,7700

**BAR REINFORCEMENT 44 - SEGMENTS**

Number	Start point	End point	Number	Start point	End point
1	1	2	3	3	4
2	2	3	4	1	4

**BAR REINFORCEMENT 44 - PROPERTIES**

CS	Used	Material	Area [m <sup>2</sup> ]	Bond with surrounding material	
1	Yes	Reinforcement	2,011E-04	Connection type	perfect connection



Description:	<b>Case Study, Reinforced Slab</b>	Unit system:	Metric
Note:	Cohesion =1.0, Friction coefficient =1.0		

side  
**13**

### BAR REINFORCEMENT 45

#### BAR REINFORCEMENT 45 - POINTS

Number	X [m]	Y [m]	Z [m]
1	0,0920	0,4500	-0,0300
2	0,3080	0,4500	-0,0300
3	0,3080	0,4500	-0,7700
4	0,0920	0,4500	-0,7700

#### BAR REINFORCEMENT 45 - SEGMENTS

Number	Start point	End point	Number	Start point	End point
1	1	2	3	3	4
2	2	3	4	1	4

#### BAR REINFORCEMENT 45 - PROPERTIES

CS	Used	Material	Area [m <sup>2</sup> ]	Bond with surrounding material	
1	Yes	Reinforcement	2,011E-04	Connection type	perfect connection

### BAR REINFORCEMENT 46

#### BAR REINFORCEMENT 46 - POINTS

Number	X [m]	Y [m]	Z [m]
1	0,3200	0,0920	-0,0300
2	0,3200	0,3080	-0,0300
3	0,3200	0,0920	-0,7700
4	0,3200	0,3080	-0,7700

#### BAR REINFORCEMENT 46 - SEGMENTS

Number	Start point	End point	Number	Start point	End point
1	4	3	3	2	1
2	2	4	4	1	3

#### BAR REINFORCEMENT 46 - PROPERTIES

CS	Used	Material	Area [m <sup>2</sup> ]	Bond with surrounding material	
1	Yes	Reinforcement	2,011E-04	Connection type	perfect connection

### BAR REINFORCEMENT 47

#### BAR REINFORCEMENT 47 - POINTS

Number	X [m]	Y [m]	Z [m]
1	0,3500	0,0000	-0,0300
2	0,3500	0,1080	-0,0300
3	0,3500	0,1080	-0,7700
4	0,3500	0,0000	-0,7700

#### BAR REINFORCEMENT 47 - SEGMENTS

Number	Start point	End point	Number	Start point	End point
1	4	3	3	2	1
2	2	3			

#### BAR REINFORCEMENT 47 - PROPERTIES

CS	Used	Material	Area [m <sup>2</sup> ]	Bond with surrounding material	
1	Yes	Reinforcement	2,011E-04	Connection type	perfect connection

### BAR REINFORCEMENT 48





Description:	<b>Case Study, Reinforced Slab</b>	Unit system:	Metric
Note:	Cohesion =1.0, Friction coefficient =1.0		

side  
**14**

**BAR REINFORCEMENT 48 - POINTS**

Number	X [m]	Y [m]	Z [m]
1	0,4700	0,0920	-0,0300
2	0,4700	0,3080	-0,0300
3	0,4700	0,0920	-0,7700
4	0,4700	0,3080	-0,7700

**BAR REINFORCEMENT 48 - SEGMENTS**

Number	Start point	End point	Number	Start point	End point
1	4	3	3	2	1
2	2	4	4	1	3

**BAR REINFORCEMENT 48 - PROPERTIES**

CS	Used	Material	Area [m <sup>2</sup> ]	Bond with surrounding material	
1	Yes	Reinforcement	2,011E-04	Connection type	perfect connection

**BAR REINFORCEMENT 49**

**BAR REINFORCEMENT 49 - POINTS**

Number	X [m]	Y [m]	Z [m]
1	0,0920	0,6000	-0,0300
2	0,3080	0,6000	-0,0300
3	0,3080	0,6000	-0,7700
4	0,0920	0,6000	-0,7700

**BAR REINFORCEMENT 49 - SEGMENTS**

Number	Start point	End point	Number	Start point	End point
1	1	2	3	3	4
2	2	3	4	1	4

**BAR REINFORCEMENT 49 - PROPERTIES**

CS	Used	Material	Area [m <sup>2</sup> ]	Bond with surrounding material	
1	Yes	Reinforcement	2,011E-04	Connection type	perfect connection

**BAR REINFORCEMENT 50**

**BAR REINFORCEMENT 50 - POINTS**

Number	X [m]	Y [m]	Z [m]
1	0,0000	0,5100	-0,0300
2	0,1080	0,5100	-0,0300
3	0,1080	0,5100	-0,7700
4	0,0000	0,5100	-0,7700

**BAR REINFORCEMENT 50 - SEGMENTS**

Number	Start point	End point	Number	Start point	End point
1	1	2	3	3	4
2	2	3			

**BAR REINFORCEMENT 50 - PROPERTIES**

CS	Used	Material	Area [m <sup>2</sup> ]	Bond with surrounding material	
1	Yes	Reinforcement	2,011E-04	Connection type	perfect connection

**BAR REINFORCEMENT 51**

**BAR REINFORCEMENT 51 - POINTS**

Number	X [m]	Y [m]	Z [m]
1	0,5200	0,0000	-0,0300



Description:	<b>Case Study, Reinforced Slab</b>	Unit system:	Metric
Note:	Cohesion =1.0, Friction coefficient =1.0		

side  
**15**

**BAR REINFORCEMENT 51 - POINTS**

Number	X [m]	Y [m]	Z [m]
2	0,5200	0,1080	-0,0300
3	0,5200	0,1080	-0,7700
4	0,5200	0,0000	-0,7700

**BAR REINFORCEMENT 51 - SEGMENTS**

Number	Start point	End point	Number	Start point	End point
1	4	3	3	2	1
2	2	3			

**BAR REINFORCEMENT 51 - PROPERTIES**

CS	Used	Material	Area [m <sup>2</sup> ]	Bond with surrounding material	
1	Yes	Reinforcement	2,011E-04	Connection type	perfect connection

**BAR REINFORCEMENT 52**

**BAR REINFORCEMENT 52 - POINTS**

Number	X [m]	Y [m]	Z [m]
1	0,6200	0,0920	-0,0300
2	0,6200	0,3080	-0,0300
3	0,6200	0,0920	-0,7700
4	0,6200	0,3080	-0,7700

**BAR REINFORCEMENT 52 - SEGMENTS**

Number	Start point	End point	Number	Start point	End point
1	4	3	3	2	1
2	2	4	4	1	3

**BAR REINFORCEMENT 52 - PROPERTIES**

CS	Used	Material	Area [m <sup>2</sup> ]	Bond with surrounding material	
1	Yes	Reinforcement	2,011E-04	Connection type	perfect connection

## Appendix C

# Encountered modelling problems

### **Convergence criteria (within line search) not satisfied due to eta limit, continuing superordinate iteration**

It is a warning about the line search iterations. This method only helps to stabilize the convergence process. Normally, the solution parameters are defined such that only 1-2 line search iterations are performed in each step. Thus, it is quite normal that it is not enough for this method to fully converge, but it is not a problem and the main important thing is that at the end each analysis step converges.

### **Problems using the interface material on contacts**

The interface material settings with tensile strength, cohesion, and friction coefficient all zero are very likely to cause numerical problems. The friction coefficient is hardly ever lower than 0.1 (maybe except an oiled surface), if you have no better measurement/estimate, 0.3-0.5 are usually not far from reality. Cohesion always has to be greater than (or at least equal to) tensile strength times the friction coefficient, i.e.,  $c \geq f_t \cdot \mu$ .

A good starting value for both initial stiffnesses is about 10 times the stiffness of the adjacent elements:

$$\frac{E_{concrete}}{element\ size} \cdot 10$$

The residual stiffness values for numerical purposes are recommended about 1/100 - 1/1000 of the initial values.

### **Varying element size**

Vary the element size to reach an optimal running time - accuracy ratio. An analysis with about 9000 elements runs for more than three hours. The use of shell elements for slender plates is recommendable because it significantly reduces the amount of elements.

### **Load conditions**

It is recommendable to model the loading conditions with prescribed displacements instead of applied forces. The behaviour of a structure around the failure load is with a displacement

controlled analysis more clearly visible. Model a stiff steel plate and assign the prescribed displacement to the one node. By modelling a monitoring point at this location, the reaction force can be saved in the output file.

### **Modelling of prestressing**

To model a prestressed specimen, make sure the first analysis step consists of the correct load cases. The first load step should consist of the boundary conditions and the prestressing load. From the second load step the load conditions should be included and the prestressing load should be excluded. See Appendix A for an example of the modelled analysis steps.